

Optical and Photodynamic Properties of the Higher-lying
States of Rose Bengal

by

John Michael Larkin

Submitted in Partial Fulfillment

of the

Requirements for the Degree

Doctor of Philosophy

Supervised by

Professor Thomas H. Foster

Department of Physics and Astronomy

The College

Arts and Sciences

University of Rochester

Rochester, New York

2000

To my parents

Curriculum Vitae

The author was born in Richland, Washington on November 28, 1970. He entered Pacific Lutheran University in 1989 with a National Merit Scholarship and graduated with a Bachelor of Science in Physics and a Bachelor of Arts in History in May 1993. In September 1993 Larkin began his graduate career in the Department of Physics and Astronomy at the University of Rochester as a G.A.A.N.N. Fellow of the United States Department of Education. He received the Master of Arts degree in 1995. He pursued his research under the supervision of Professor Thomas H. Foster. In 1996 he became a Frank J. Horton Fellow at the University of Rochester's Laboratory for Laser Energetics, where he received additional guidance from Dr. William R. Donaldson.

Acknowledgments

This work would not have been possible without the support of many people and organizations. Particular thanks is given for financial support from the Department of Physics and Astronomy and the Laboratory for Laser Energetics, both at the University of Rochester. Thanks is also due to the United States Departments of Education and Energy for their financial support.

I would like to thank Dr. Thomas H. Foster for his encouragement and support of this work. He provided crucial guidance, especially with regard to the fundamental issues of photochemistry and photobiology in this thesis.

I would like to thank Dr. William R. Donaldson for providing access to the laboratory in which most of this work was conducted. His daily assistance and advice made the experimental aspects of this work possible.

I would like to thank Dr. Robert S. Knox for many helpful discussions and his thorough comments on this work.

Many other people involved in research at the University of Rochester have also facilitated this work. Thanks for many helpful discussions is owed to the students in Foster's PDT group, particularly Ed Hull and Irene Georgakoudi. Special thanks is given to Irene for her assistance in working with multicell tumor spheroids and in using an oxygen microelectrode. Dr. Hilf, Scott Gibson and

the rest of the Hilf lab kindly assisted me on many occasions. Students at the Laboratory for Laser Energetics also provided helpful discussions as well as loans of equipment and their support is greatly appreciated.

I would also like to acknowledge the love and encouragement shown me by my parents, Dave and Carol Larkin, and my sisters, Kim Suko and Sheila Larkin.

Abstract

We have studied the photophysics and photochemistry of the higher-lying triplet states of rose bengal (tetraiodo-tetrachlorofluorescein) in water.

Triplet-triplet absorption spectroscopy is used to identify a previously undescribed triplet state of rose bengal with an absorption cross section of $(1.1 \pm 0.1) \times 10^{-16} \text{ cm}^2$ at 1064 nm. This state is the least energetic triplet state, excluding T_1 , to be identified, so it will be denoted as T_2 .

Two-step excitation techniques for measuring reverse intersystem crossing, an intersystem crossing from a higher-lying triplet state to a singlet state, are described. The method of two-step laser-induced fluorescence is used to determine the quantum yield of reverse intersystem crossing for three higher-lying triplet states of rose bengal. Reverse intersystem crossing yields of 0.0076 ± 0.0002 , < 0.06 , and 0.12 ± 0.02 are found for the triplet states excited by 1064-, 632-, 532-nm light, denoted respectively as T_2 , T_3 and T_4 . Bond cleavage may also follow excitation of a higher-lying state. Other workers have found evidence for this photochemical process from T_3 but not T_4 . The method of two-step laser-induced bleaching was used to determine whether bond cleavage occurs from T_2 . No evidence was found for a such a process. It had been hypothesized that reverse intersystem crossing was responsible for the lack of bond cleavage from T_4 . A

theoretical investigation based on kinetic models including reverse intersystem crossing shows that variations in the yield of this process would produce only small changes in the yield of photoproducts formed by bond cleavage.

A two-photon absorption cross section of 0.028 ± 0.001 GM for rose bengal excited by 1064-nm light is determined using a fluorescence technique. The impact of higher-lying states on multiphoton excitation is discussed, and it is shown that the neglect of reverse intersystem crossing can lead to an apparent enhancement of the two-photon absorption cross section in the analysis of fluorescence data.

Table of Contents

Curriculum Vitae	iii
Acknowledgments	iv
Abstract	vi
Table of Contents	viii
List of Tables	xii
List of Figures	xiv
1 Introduction	1
1.1 Introductory photophysics	2
1.2 Selection rules for radiative transitions	5
1.3 Phosphorescence, excited state absorption, and identification of the triplet state	8
1.4 Intersystem crossing yields	9
1.4.1 The heavy atom effect	9
1.4.2 The energy gap law	11
1.4.3 Oxygen-enhanced intersystem crossing	12
1.5 Photodynamic therapy	16

1.6	Rose bengal	17
1.7	Outline of the thesis	19
2	Detection and excitation of higher-lying triplet states	23
2.1	Experimental methods	24
2.1.1	In-line geometry	26
2.1.2	Right-angle geometry	30
2.1.3	Materials	33
2.2	Analytical methods	33
2.2.1	Total depletion method	34
2.2.2	Partial saturation method	35
2.2.3	Pulsed fluence variation	36
2.3	Results and discussion	38
2.4	Discussion	44
3	Intersystem crossing from higher-lying triplet states	45
3.1	Background	45
3.2	Measurement techniques for determining reverse intersystem crossing yields	47
3.2.1	Two-step laser-induced bleaching	48
3.2.2	Two-step laser-induced fluorescence	50
3.2.3	Discussion of the Φ_{risc} measurement techniques	51
3.3	Prior work	54
3.3.1	Low-yield results	55
3.3.2	High-yield results	57
3.3.3	Previous rose bengal results	59
3.4	One-color experiment	62

3.4.1	Experimental methods	62
3.4.2	Analytical methods	66
3.4.3	Results	73
3.5	Two-color experiments	79
3.5.1	Experimental methods	79
3.5.2	Analytical methods	82
3.5.3	Results	90
3.6	Discussion	94
4	Photochemistry of higher-lying states	99
4.1	Overview	99
4.2	Limitations of conventional photodynamic therapy and proposed remedies	100
4.3	Objections to the Leupold-Freyer two-step activation proposal	104
4.4	Photochemistry of the higher-lying states of rose bengal	106
4.5	Bond cleavage	110
4.6	Measurements of T_2 photochemistry	113
4.6.1	Theoretical basis of two-step laser-induced bleaching	113
4.6.2	Experimental methods and results	118
4.6.3	Analysis and discussion	124
4.7	Explanation of photochemical differences based on reverse intersystem crossing	128
4.8	Discussion of two-step activation feasibility	134
4.9	Conclusion	139
5	Simultaneous multiphoton absorption and the effects of higher-lying states	140

5.1	Background	141
5.2	Fluorescence technique for determining the two-photon absorption cross section	144
5.3	Intensity-squared dependence of two-photon excited fluorescence	145
5.4	Two-photon excited fluorescence and reverse intersystem crossing in rose bengal	149
5.4.1	Experimental methods and results	149
5.4.2	Analysis	153
5.5	Conclusion	160
6	Summary and suggestions for future work	165
6.1	Summary	165
6.2	Suggestions for future work	169
	Bibliography	172
A	Absorption and the effects of molecular rotation	185
A.1	Molecular orientation and Beer's law	185
A.2	Effect of rotational diffusion on ground state depletion	186
A.2.1	Analytical solutions	186
A.2.2	Numerical solutions	189

List of Tables

2.1	Equipment used in the pump-probe experiment	28
2.2	Equipment used in the laser flash photolysis experiments	32
3.1	Summary of reverse intersystem crossing yields appearing in the literature.	63
3.2	Equipment used in the one-color laser-induced fluorescence experiments	65
3.3	Photophysical parameters of rose bengal in water that are relevant to 532-nm excitation. Parameters to be determined in the fitting process are indicated by t. b. d.	69
3.4	Equipment used in the two-step laser-induced fluorescence experiments	81
3.5	Photophysical parameters for two-color excitation of rose bengal	85
3.6	Energies of rose bengal excited states	98
4.1	Photophysical parameters for 1064-nm excitation of the T_1 state of rose bengal	116
4.2	Equipment used in the two-color laser-induced bleaching experiments	120
4.3	Energies and radical yields of rose bengal excited states	129

5.1	Photophysical parameters of rose bengal in water that are relevant to 1064-nm excitation. Parameters to be determined in the fitting process are indicated by t. b. d.	156
5.2	Photophysical parameters of Rhodamine 6G in ethanol that are relevant to 1064-nm excitation.	157

List of Figures

1.1	Energy level diagram showing the basic photophysical processes.	4
1.2	Schematic of potential energy surfaces for a non-radiative transition between two electronic states	13
1.3	Non-radiative transition rate as a function of energy gap	14
1.4	Rose bengal-related articles in the research literature (1991-1999)	20
2.1	Schematic of transient absorption geometries	25
2.2	Experimental setup for pump-probe measurements	27
2.3	Experimental setup for laser flash photolysis measurements	31
2.4	Ground state absorption spectrum of rose bengal	40
2.5	Pump-probe measurements of 1064-nm absorption by T_1	41
2.6	Dependence of triplet extinction fit on choice of data subset	42
2.7	Rose bengal near-infrared triplet-triplet absorption spectrum	43
3.1	Idealized two-step laser-induced bleaching signal	49
3.2	Idealized two-step laser-induced fluorescence signal	52
3.3	Experimental setup for one-color laser-induced fluorescence measurements	64
3.4	Energy-level scheme for 532-nm excitation dynamics	68

3.5	Experimental results of one-color laser-induced fluorescence measurement ($\lambda = 532$ nm)	74
3.6	Population dynamics during one-color excitation	75
3.7	Effect of triplet-triplet absorption and reverse intersystem crossing on S_1 dynamics during one-color excitation	77
3.8	Effect of rotational diffusion and thermalization on one-color laser-induced fluorescence	78
3.9	Experimental setup for two-step laser-induced fluorescence measurements ($\lambda_2 = 1064$ nm)	80
3.10	Energy-level scheme for two-color excitation dynamics, complete model	84
3.11	Energy-level scheme for two-color excitation dynamics, \mathcal{P}_2 subset of model	88
3.12	Emission spectra resulting from 532- + 1064-nm excitation	91
3.13	Two-step laser-induced fluorescence ratio versus \mathcal{P}_2 fluence for 532- + 1064-nm excitation	93
4.1	Energy level diagrams for two-step activated photodynamic therapy	105
4.2	Potential energy curves for states in the predissociation pathway	111
4.3	Energy-level scheme for 1064-nm excitation of the T_1 state of rose bengal	117
4.4	Experimental setup for two-step laser-induced bleaching measurements	119
4.5	Transient transmission at 920 nm induced by 532-nm excitation reveals long-term photobleaching effects	123
4.6	Transient transmission at 920 nm induced by one- and two-step excitation	125

4.7	Comparison of transient transmission at 920 nm induced by one- and two-step excitation	126
4.8	Relative change in absorbance at 920 nm induced by two-step excitation	127
4.9	Theoretical dependence of radical production on the forward and reverse intersystem crossing yields	132
4.10	Theoretical dependence of radical production on the reverse intersystem crossing yield and upper triplet state lifetime	133
5.1	Models of two-photon excitation	142
5.2	Models of two-photon excited fluorescence quenching	147
5.3	Experimental setup for two-photon excited fluorescence measurements	151
5.4	Two-photon excited fluorescence of rose bengal and Rhodamine 6G	152
5.5	Energy-level scheme for 1064-nm multiphoton excitation dynamics	155
5.6	The best value of the two-photon absorption cross section δ is determined by a locating a minimum in χ^2 of the fit of δ to the 1064-nm excited fluorescence of rose bengal	158
5.7	Best fit to 1064-nm-excited fluorescence of rose bengal	159
5.8	Population dynamics of S_1 during multiphoton excitation	161
5.9	Population dynamics of T_1 during multiphoton excitation	162
5.10	Population dynamics of T_2 during multiphoton excitation	163
A.1	Analytical solutions of ground state depletion including effects of rotational motion.	188
A.2	Numerical solutions of ground state depletion including effects of rotational motion	192
A.3	Evolution of the ground state population when $k_{rot} = 3.2 \text{ ns}^{-1}$	193

A.4	Evolution of the ground state population when $k_{rot} = 0$	194
A.5	Dependence of rotational diffusion model on number of angular divisions	195

Chapter 1

Introduction

Rose bengal is a potent photosensitizing agent first synthesized in the 1880s. Possessing a near unity intersystem crossing yield, it has been a standard reference used in experiments determining the intersystem crossing and singlet oxygen yields of other photosensitizers. It has also been used as source of singlet oxygen in many studies of the biological effects of singlet oxygen. Careful and complete characterization of molecules such as rose bengal is essential if they are to be useful references.

Much of the previous interest in photosensitive molecules has been focused on the properties of the lowest excited singlet and triplet states. Reports in the past two decades have suggested that higher-lying states could produce novel effects that might enhance conventional photodynamic therapy. The logical place to begin a study of the previously ignored higher-lying states is with rose bengal, one of the standard conventional photosensitizers.

This thesis describes studies of the important properties of the upper-excited states of the molecule rose bengal. We will present evidence for a new triplet state of rose bengal that we predicted would result in strong triplet-triplet absorption in the near-infrared. The question of whether reverse intersystem crossing yields

are state-dependent will be answered using a two-step laser-induced fluorescence technique. An explanation of differences in oxygen-independent damage based on reverse intersystem crossing will be proposed, and the validity of that explanation will be evaluated using kinetic models. Our experimental measurements of photobleaching will be used to set a lower limit on the energy required for cleavage of a carbon-iodine bond in rose bengal. We will also show that neglect of reverse intersystem crossing can lead to an apparent enhancement of the two-photon absorption cross section in the analysis of fluorescence data.

This chapter lays a foundation for the remainder of the thesis by reviewing key concepts of molecular physics, particularly those related to the absorption and emission of light. Following that review is a brief history of photodynamic therapy and rose bengal. Finally, the chapter concludes with an overview of the remainder of the thesis.

1.1 Introductory photophysics

According to the Pauli exclusion principle, no more than two electrons may occupy any particular molecular orbital. Most molecules have an even number of electrons as well as non-degenerate orbitals, resulting in a minimum energy configuration in which electrons only occur in pairs with anti-parallel spins. Such a ground state molecule will have no net electronic spin. States with zero spin are called singlet states because the M_S quantum number describing the total spin can have only one value, zero. If one pair of electron spins is parallel rather than anti-parallel then the spin quantum number will be 1. This configuration is called a triplet state because M_S can take on three values: +1, 0, and -1. The number of possible spin quantum numbers is also called the state's multiplicity. Throughout the rest of this work singlet states will be denoted by S_i and triplet states by T_i . In this

notation S_0 is the ground state, S_1 is the first excited singlet state, T_1 is the first excited state that is a triplet, and so forth. In the infrequent case where the ground state is a triplet it will be denoted by T_0 . According to Hund's rule a high multiplicity orbital configuration will be less energetic than an otherwise identical orbital configuration with a smaller multiplicity. In practice this means that each excited singlet state has an associated less energetic triplet state.

Dioxygen (O_2), which will simply be called oxygen or molecular oxygen elsewhere in this work, is one of the important exceptions to the general rule that the ground state of a molecule is a singlet. The triplet nature of the oxygen ground state results from the degeneracy of its highest occupied molecular orbitals. Because reactions between oxygen and dye molecules provide much of the context for the present work, it is convenient to reserve the S_i and T_i notation for the dye molecule and adopt an alternative notation for oxygen. Therefore the ground state of oxygen will be called 3O_2 and the corresponding excited singlet state $O_2(^1\Delta_g)$ will be abbreviated as 1O_2 .

The three main types of non-radiative transitions that will be considered are vibrational relaxation, internal conversion, and intersystem crossing. Vibrational relaxation is a fast transition occurring within the vibrational levels of a single electronic state. Internal conversion is an isoenergetic transition between states of the same multiplicity (*e.g.*, S_2 to S_1). Typically it occurs from a lower-lying vibrational level of one electronic state to an upper-lying vibrational level of another state. This is predominantly a unidirectional transition because vibrational relaxation will quickly depopulate the upper-lying vibrational levels. Intersystem crossing is essentially equivalent to internal conversion except that it occurs between states of different multiplicity (*e.g.*, S_1 to T_1). The processes of internal conversion and intersystem crossing are shown in Fig. 1.1. Transitions between

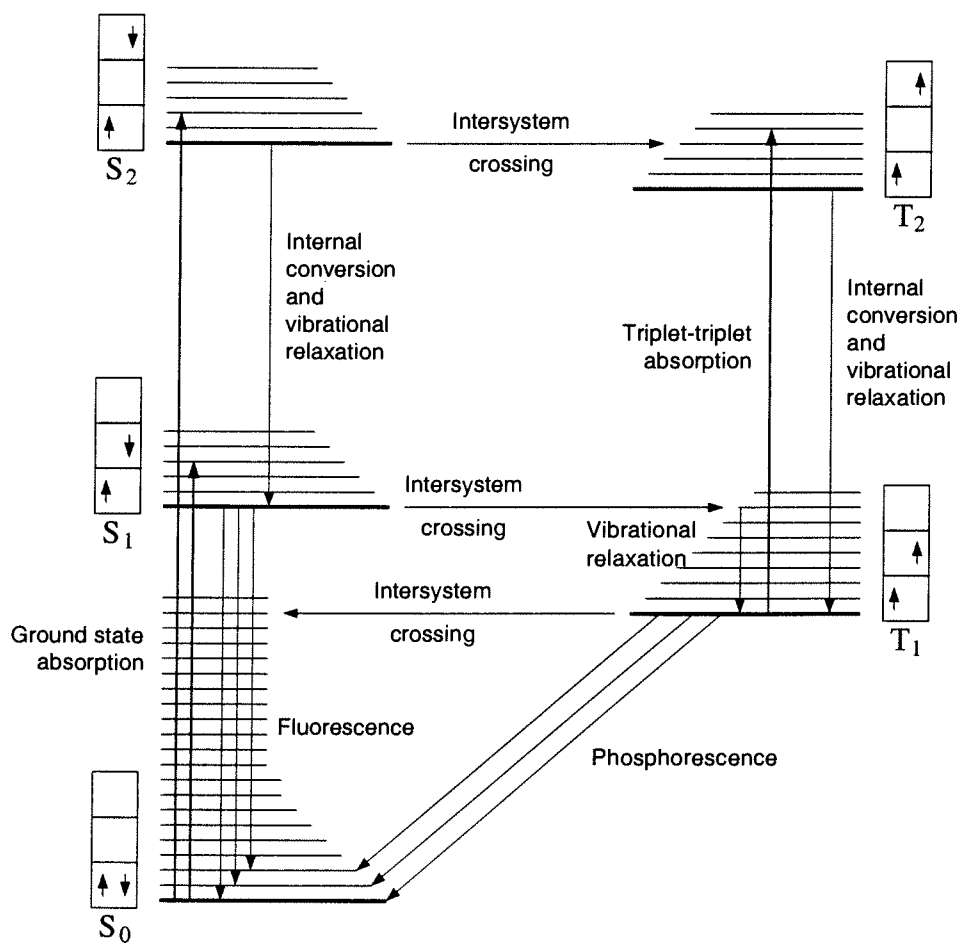


Figure 1.1: Energy level diagram showing the basic photophysical processes. The spin orientations of the outermost pair of electrons are illustrated for the case of no orbital degeneracy. Electronic states are shown along with their associated vibrational levels.

states of different multiplicity are “forbidden” in a simple treatment of the molecular system because spin angular momentum is not conserved. The forbiddenness of intermultiplicity transitions can be reduced if relativistic effects result in some coupling between spin and orbital angular momentum, allowing a change in spin if there is a corresponding change in orbital angular momentum. In many cases this coupling is weak so as a general rule internal conversion is a much more probable transition than intersystem crossing. Conditions leading to enhanced intersystem crossing will be described in §1.4.

Radiative transitions, like the non-radiative transitions described above, are divided into two main types based on multiplicity. Radiative transitions between states of the same multiplicity will be called fluorescence and intermultiplicity transitions are phosphorescence. The spin conservation considerations described above also apply to radiative transitions, so fluorescence tends to be more probable than phosphorescence. Fluorescence occurs at an approximately 10^6 faster rate than phosphorescence for molecules containing atoms no heavier than oxygen [1]. As a consequence, fluorescence tends to be shorter-lived than phosphorescence. Alternatively, in some parts of the scientific community a radiative transition is termed fluorescence or phosphorescence based on its lifetime. In many cases the lifetime-based and multiplicity-based definitions will overlap, but there are also several well-known processes leading to long-lived singlet-singlet emission. The multiplicity-based definition is used throughout this work so emissions such as these will be termed fluorescence rather than phosphorescence.

1.2 Selection rules for radiative transitions

Radiative transitions cannot occur between any given pair of states. Allowed transitions occur when various selection rules, based on fundamental laws such as

the conservation of angular momentum, are satisfied. Transitions which violate one or more selection rules are termed “forbidden” because in an idealized model they would never occur. Deviations of the actual molecule from the idealized model are such that “forbidden” transitions are not absolutely prohibited. In general, “forbidden” transitions are often less probable than “allowed” transitions, but still possible.

The set of rules used most commonly in photophysics are those for electric dipole transitions in molecules where the spin-orbit interaction is weak. An additional rule, the Laporte selection rule, applies to the subset of molecules which are centrosymmetric. Transitions involving dipole or electric quadrupole moments require different sets of selection rules. Only electric dipole selection rules will be described here, but information on other types of transitions can be found in a quantum mechanics text such as Ref. [2].

The Laporte selection rule applies only to electric dipole transitions in centrosymmetric molecules. The rate of such a transition is proportional to

$$\langle \psi_f | e\mathbf{r} | \psi_i \rangle, \quad (1.1)$$

where $e\mathbf{r}$ is the electric dipole operator and ψ_i and ψ_f are the initial and final states. If the molecule is centrosymmetric, the states ψ_i and ψ_f have a well defined parity. This parity has traditionally been denoted by g and u where g comes from the German word for even, *gerade*, and u stands for *ungerade* or odd. Symmetry arguments show that Eq. (1.1) will vanish if the overall parity is odd. Because the electric dipole operator is odd, the combination of ψ_i and ψ_f must also be odd. Therefore, the Laporte selection rule states that the only allowed transitions will be g→u or u→g [3].

Spatial symmetry resulted in the Laporte selection rule, but conservation of angular momentum for the total electron spin of the molecule, S , leads to the

next selection rule. This rule states that transitions must satisfy $\Delta S = 0$. It is this rule that forbids transitions between singlet states where $S = 0$ and triplet states where $S = 1$. As noted above, this selection rule only holds for the case of negligible spin-orbit coupling.

Conservation of orbital angular momentum, L , requires that $\Delta L = \pm 1, 0$. Each electron involved in the transition must satisfy $\Delta l = \pm 1$ because the photon carries a unit spin. The case $\Delta L = 0$ can occur only if two electrons are involved in the transition [4]. This selection rule applies only to the case of negligible spin-orbit coupling.

The conservation of total angular momentum J is independent of the strength of the spin-orbit interaction. This requires that $\Delta J = \pm 1, 0$ with the special case that $J = 0$ to $J = 0$ transitions are forbidden. When the spin-orbit interaction is negligible, the total angular momentum is found by Russell-Saunders coupling. The assumption in this case is that only the total spin S interacts with the total orbital angular momentum L . In this limit the allowed values are $J = L + S, L + S - 1, L + S - 2, \dots, |L - S|$. At the opposite extreme is jj -coupling. In this case the strong spin-orbit interaction couples each electron's spin s to its orbital angular momentum l to produce the combined angular momentum j for that electron. The total angular momentum of the molecule is then found from the sum of all of the individual j . Molecules may also fall somewhere between the Russell-Saunders and jj -coupling limits [4].

1.3 Phosphorescence, excited state absorption, and identification of the triplet state

Early evidence for the generation of triplet states of molecules following excitation of their singlet ground state was the observation of a long-lived luminescence lasting for microseconds or longer. The origins of this luminescence were not immediately associated with a triplet state, partly due to the observation that the luminescence consisted of two distinct spectral bands, α and β , but exhibited only a single lifetime. The α band exactly corresponded to the much shorter-lived fluorescence spectrum, and the β band was red-shifted compared to this [5].

Jabłoński proposed that a metastable state existed below the fluorescent state [6]. The α emission was attributed to repopulation of the fluorescent state from the metastable state through thermal activation, and the β emission resulted from a direct transition between the metastable state and the ground state. Experimental observations confirmed that the strength of the α band was temperature-dependent [7]. In the current literature the term α luminescence has been replaced by delayed thermal fluorescence.

Using intense illumination it was possible to deplete the ground state of the molecule and generate a significant concentration of molecules in the metastable state. The absorption spectrum of the metastable state could then be measured. Lewis *et al.* observed that exciting the metastable state to these higher-lying states did not repopulate the fluorescent or ground states, but the higher-lying states were found to relax exclusively to the metastable state [7]. In 1944 Lewis and Kasha presented substantial evidence for the triplet nature of the metastable state [5]. The experiments in which these absorption properties of the metastable state were studied provided key evidence for the triplet nature of this state. These

observations were consistent with an explanation in which the states directly excited from the ground state had one multiplicity and the metastable state and its higher-lying states had another, with intermultiplicity transitions being “forbidden” because of conservation of spin angular momentum. Measurements of triplet-triplet absorption continue to play an important role in understanding the photophysics and photochemistry of the triplet state of molecules.

1.4 Intersystem crossing yields

Intersystem crossing would be strictly forbidden if there were no spin-orbit coupling. Even with this coupling intersystem crossing often remains an improbable process, but under certain conditions this transition rate can become comparable to other decay rates associated with an excited state. Specifically, intersystem crossing can become significant in a molecule which contains heavy atoms and which has a small energy gap between the two states associated with the transition. In addition, bimolecular effects (to be considered below) can also increase the yield of intersystem crossing in certain cases.

1.4.1 The heavy atom effect

The motion of the electron in the electrostatic field \mathbf{E} of the nucleus produces a coupling between the spin and orbital angular momenta. This is a consequence of the fact that the electrostatic field of the nucleus appears as a magnetic field in the rest frame of the electron. This magnetic field, according to special relativity, is given by

$$\mathbf{B}' = -\frac{\gamma}{c^2} \mathbf{v} \times \mathbf{E} \quad (1.2)$$

where \mathbf{v} is the velocity of the electron as measured in the center-of-mass rest frame and $\gamma = 1/\sqrt{1 - (v/c)^2}$. Expanded in powers of v/c ,

$$\mathbf{B}' = -\frac{1}{c} \left(1 + \frac{1}{2} \frac{v^2}{c^2} + \frac{3}{8} \frac{v^4}{c^4} + \dots \right) \left(\frac{\mathbf{v}}{c} \times \mathbf{E} \right), \quad (1.3)$$

which to first order in v/c gives

$$\mathbf{B}' \approx -\frac{1}{c^2} \mathbf{v} \times \mathbf{E}. \quad (1.4)$$

The intrinsic magnetic moment of the electron interacts with this field, providing an additional term to the Hamiltonian equal to

$$H_{SO} = -\frac{e\mathbf{S}}{m} \cdot \mathbf{B}' \quad (1.5)$$

where \mathbf{S} is the spin angular momentum, m is the mass of the electron, and e the charge of the electron. For a hydrogenic atom, the electric field produced by the nucleus is given by

$$\mathbf{E} = -\frac{Ze}{r^3} \mathbf{r} \quad (1.6)$$

where Z is the nuclear charge. According to Eq. (1.4), this electric field is experienced as a magnetic field in the electron rest frame such that

$$\mathbf{B}' = \frac{Ze}{mc^2 r^3} \mathbf{p} \times \mathbf{r} \quad (1.7)$$

where \mathbf{p} is the linear momentum of the electron in the center-of-mass frame. Recalling that \mathbf{L} , the orbital angular momentum, is defined as $\mathbf{L} \equiv \mathbf{r} \times \mathbf{p}$ allows Eq. (1.7) to be written as

$$\mathbf{B}' = -\frac{Ze}{mc^2 r^3} \mathbf{L}. \quad (1.8)$$

It follows that the Hamiltonian for the interaction between the electron spin and the electrostatic field of the nucleus is found by using this expression for the magnetic field in Eq. (1.5). This differs from experiment by a factor of two. The

origin of this disagreement can be found in the treatment of the electron rest frame as inertial when in fact it is not. The non-inertial nature of the electron frame gives rise to Thomas precession which introduces the required factor of 1/2 [8]. Therefore, the correct spin-orbit interaction for a hydrogenic atom is

$$H_{\text{SO}} = \frac{Ze^2}{2m^2c^2r^3} \mathbf{L} \cdot \mathbf{S} . \quad (1.9)$$

In hydrogenic atoms $\langle r^{-n} \rangle \propto Z^n$ so the spin-orbit interaction will be proportional to Z^4 . This strong dependence on nuclear charge also applies to non-hydrogenic atoms and produces significant spin-orbit coupling in all heavy atoms. This topic is covered in most quantum mechanics texts but for a more detailed treatment see Ref. [9]. The incorporation of heavy atoms into molecules has a similar effect, but the coupling is reduced because the optically-active electrons are not strongly localized near the heavy nucleus. This is known as the internal heavy atom effect. Alternatively, the external heavy atom effect relies on the close proximity of heavy atoms in nearby molecules to increase the spin-orbit coupling.

1.4.2 The energy gap law

In addition to the heavy atom effect described above, the likelihood of intersystem crossing is also affected by the energy gap between the two states. Englman and Jortner have described an energy gap law for non-radiative transitions which is generally applicable to molecular systems [10]. The weak coupling limit of this theory, relevant to transitions which do not involve a photochemical rearrangement process, states that the rate, k_{nr} , of a non-radiative transition is given by

$$k_{nr} = \frac{C^2 \sqrt{2\pi}}{\hbar \sqrt{\hbar \omega_M \Delta E}} \exp(-\gamma \Delta E / \hbar \omega_M) \quad (1.10)$$

with

$$\gamma \equiv \log \left(\frac{2 \Delta E}{d \hbar \omega_M \Delta_M^2} \right) - 1 \quad (1.11)$$

where ΔE is the energy gap between the origins of the two electronic states as shown in Fig. 1.2, ω_M is the frequency of the vibrational mode with maximum frequency, d is the degeneracy of the mode with maximum frequency and Δ_M is the displacement of the normalized nuclear coordinate for this mode. The mode with the highest vibrational frequency is commonly a C–H stretch mode such that $\hbar\omega_M \approx 3000 \text{ cm}^{-1}$. The coupling parameter C depends on the initial and final electronic states and is given by

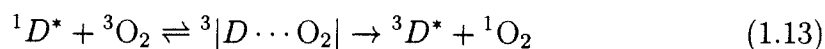
$$C = \frac{\langle \psi_f | H_n | \psi_i \rangle}{\langle \psi_f | \psi_i \rangle} \quad (1.12)$$

where H_n is the nuclear part of the Hamiltonian and includes contributions due to spin-orbit coupling and nuclear motion. The contribution of heavy atoms to an increased rate of intersystem crossing enters into Eq. (1.10) through this parameter.

The rate of a non-radiative transition decreases at an approximately exponential rate as the energy gap between the two states increases, as illustrated for a sample set of parameters in Fig. 1.3. The yield of a particular non-radiative transition depends on the rates of competing transitions. A particularly elegant example of an application of the energy gap law is the work of Chynwat and Frank on internal conversion in carotenoids [11].

1.4.3 Oxygen-enhanced intersystem crossing

The discussion above has been restricted to monomolecular singlet-triplet transitions, but bimolecular reactions can also result in the generation of triplet states from excited singlet states [12]. In particular, molecular oxygen has been found to enhance the intersystem crossing yield through two processes:



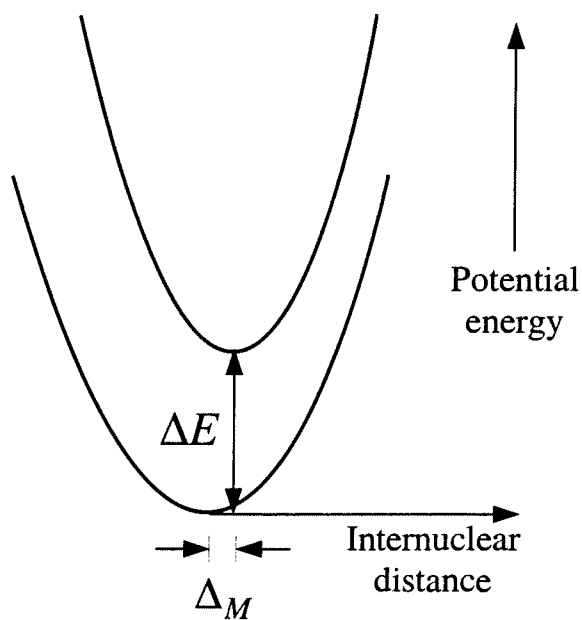


Figure 1.2: Schematic of potential energy surfaces for a non-radiative transition between two electronic states. ΔE is the energy gap between the origins of the two electronic states, and Δ_M is the displacement of the normalized nuclear coordinate for the vibrational mode with the maximum frequency.

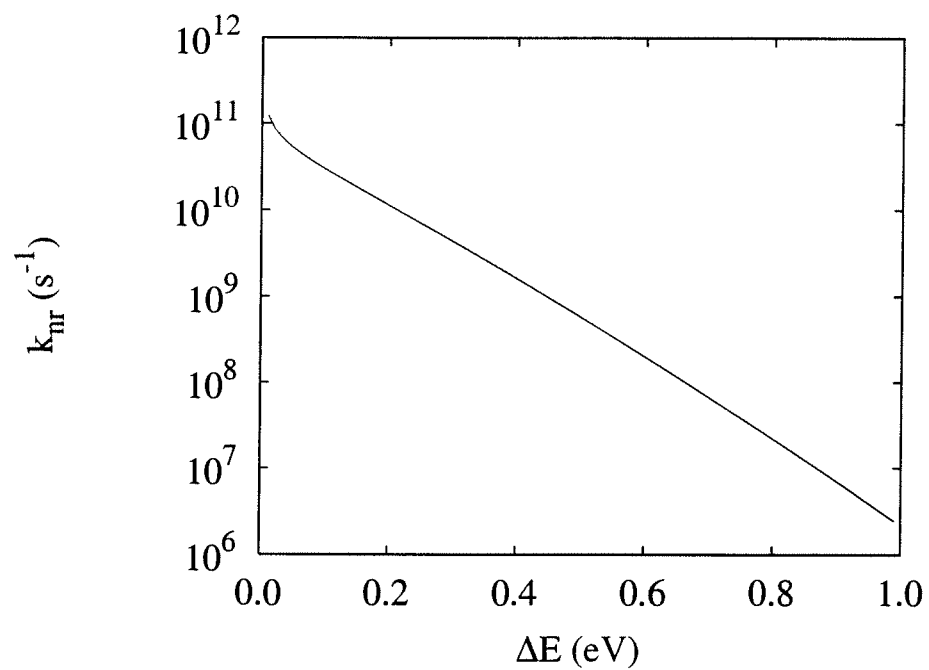
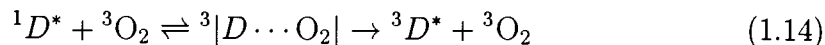


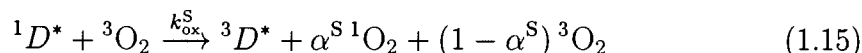
Figure 1.3: Non-radiative transition rate as a function of energy gap. Calculated from Eq. (1.10) using $d = 2$, $\hbar\omega_M = 0.37$ eV, $\Delta_M = 0.2$, and $C = 3.5 \times 10^{-3}$ eV.

and



where ${}^3|D \cdots O_2|$ is a short-lived complex between the dye, D , and molecular oxygen. The notation ${}^1D^*$ and ${}^3D^*$ refers in nearly all cases to the states labeled S_1 and T_1 , respectively. Process (1.13) can only occur when $\Delta E_{S_1, T_1} \geq 0.97$ eV, the energy required to excite 1O_2 , and both processes can become significant only for dyes in which τ_{S_1} is sufficiently large (≥ 1 ns).

It is assumed that processes (1.13) and (1.14) are the only mechanisms by which the complex ${}^3|D \cdots O_2|$ deactivates. If α^S is the yield of process (1.13) then



where k_{ox}^S is the bimolecular rate constant for oxygen-mediated $S_1 \rightarrow T_1$ quenching. This process results in an oxygen-dependent intersystem crossing yield

$$\Phi'_{isc} = \frac{\Phi_{isc} + k_{ox}^S \tau_{S_1}^0 [O_2]}{1 + k_{ox}^S \tau_{S_1}^0 [O_2]} \quad (1.16)$$

where $\tau_{S_1}^0$ is the S_1 lifetime in the absence of oxygen. The enhanced intersystem crossing plus the direct production of singlet oxygen from S_1 via process (1.13) can result in an oxygen-dependent efficiency for singlet oxygen production. For example, McLean *et al.* find that the singlet oxygen quantum yield for protoporphyrin-IX-dimethylester (PPDME) ranges from 0.63 in oxygen-saturated benzene to 0.45 when the oxygen concentration is reduced to approximately 100 μM [12]. Using Eq. (1.16) it is calculated that an oxygen concentration of 150 μM produces an additional 5% intersystem crossing for PPDME based on its lifetime ($\tau_{S_1}^0 = 23$ ns [13]) and rate constant for oxygen quenching ($k_{ox}^S = 1.5 \times 10^{10} \text{ M}^{-1} \text{ s}^{-1}$ [12]).

In this work the $S_1 \rightarrow T_1$ intersystem crossing yield for rose bengal will be treated as a constant. Rose bengal's short S_1 lifetime (~ 90 ps) makes the process of oxygen-mediated quenching less probable [14–16]. Using the same quenching

rate constant as for PPDME in benzene suggests that an oxygen concentration of ~ 7 mM is required to add 1% to rose bengal's intersystem crossing yield. Oxygen concentrations of this magnitude were not used in any of the experiments to be described in later chapters.

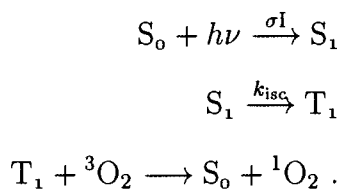
1.5 Photodynamic therapy

Photodynamic therapy (PDT) is a treatment in which a dye, light, and oxygen cause photochemically-induced cell death. This three-component requirement for producing the desired photochemistry provides the ability to design a treatment which has good selectivity for destroying diseased regions while sparing the surrounding healthy tissue. Potential and current applications of PDT include the treatment of cancer, macular degeneration, and arteriosclerosis as well as viral inactivation of blood products.

Observations of the photodynamic effect occurred at least as early as the end of the nineteenth century. While studying differences between the *in vivo* and *in vitro* efficacy of potential anti-malarial drugs in 1900 Oskar Raab observed that the dye acridine rapidly killed paramecia when exposed to light, but had no effect in the dark [17]. These observations quickly inspired attempts to use this effect to treat disease. Light and the dye eosin were combined to treat skin cancer in 1903 [18]; however, significant progress in applying photodynamic therapy to the treatment of cancer did not occur until the 1940s and 1950s, when it was discovered by Figge [19] and Lipson [20] that porphyrin-based photosensitive dyes preferentially accumulated in malignant tissues. A sustained series of studies into the mechanisms and applications of photodynamic therapy for the treatment of a broad range of cancers was initiated by Dougherty in the 1970s [21]. This work was joined by many researchers worldwide and led the U.S. Food and Drug Adminis-

tration in December 1995 to approve the treatment of advanced esophageal cancer using photodynamic therapy with Photofrin[®], a porphyrin-based photosensitizer. In 1998 this approval was extended to cover the treatment of early-stage lung cancer. Other countries have also approved photodynamic therapy for the treatment of bladder, gastric, and cervical cancers. Several review articles have been published that provide an overview of the clinical results and history of photodynamic therapy [22–24].

The photodynamic effect is a result of three primary optical processes. First, the ground state of the dye, S_0 , is optically excited to produce S_1 . Population from this state is transferred by intersystem crossing to the dye's lowest triplet state, T_1 . Finally, collisional energy transfer from the triplet dye to ground-state molecular oxygen, 3O_2 , produces highly reactive singlet oxygen, 1O_2 , and returns the dye to its ground state:



The singlet oxygen produced as a result of this three-step process reacts readily with many biological targets and, in sufficient quantity, can destroy a wide variety of cells.

1.6 Rose bengal

According to the historical records of the chemical manufacturer CIBA-Geigy, rose bengal was first synthesized for use in dyeing wool by Rudolf Gnehm in 1880–1881 at one of their predecessor companies in Basel, Switzerland [25] and its first mention in print was the 1881 edition of Schultz's *Tables of Dyes*. Rose bengal

was so named because it reminded Gnehm of the red dot worn on the foreheads of Bengali women to symbolize marriage. Rose bengal is one of many xanthene dyes introduced at the end of the nineteenth century based on the pioneering work of Baeyer at the university in Strasbourg. Chief among Baeyer's contributions were fluorescein and with Emil Fischer, its brominated derivative, eosin. Gnehm provided the two other halogenated derivatives that have had a lasting impact, rose bengal (tetraiodo-tetrachlorofluorescein) and erythrosin (tetraiodofluorescein).

The applications of dyes derived from fluorescein have gone far beyond dyeing wool. The intense red color of erythrosin (also known as FD&C Red #3) is highly valued by the food industry and continues to be used in foods (maraschino cherries, candies, etc.) and oral medications (Tylenol capsules, for example) despite ongoing concerns raised by studies showing that it could lead to thyroid cancer when ingested in large quantities by rats [26]. These concerns did result in it being banned from use in cosmetics in the United States. Rose bengal has also been valued for its brilliant red color. In Japan both erythrosin and rose bengal are used in foods at up to 100 μM concentrations, providing a dietary source of iodine. In addition, Japanese cosmetics such as lipstick can consist of as much as 8% (0.8 M) of these two dyes [27].

The intense fluorescence of fluorescein has long been one of its most important properties, ranging from its use by Baeyer in 1877 to prove the connection of the Danube to the Rhine to its more recent use in the many specially designed molecular probes that are increasingly important in the biological sciences [28]. The fluorescence of the fluorescein derivatives is inversely related to the extent of their halogenation, with rose bengal exhibiting only a weak fluorescence.

The discovery of photodynamic action by Oskar Raab in 1900 [17] was followed by the more extensive 1904 work by von Tappeiner and Jodlbauer, in which

the effectiveness of photodynamic action against paramecia was studied for various combinations of dyes, light, and oxygenation [29]. Rose bengal and the rest of the known fluorescein derivatives were among the dyes studied. One of the relationships discovered was that the photodynamic effect was inversely proportional to the fluorescence yield of the dye. This is now understood in terms of the heavy-atom effect.

Rose bengal has a substantial yield of singlet oxygen and has been used as a standard for determining the singlet oxygen yields of other photosensitizers. In addition to being used for fundamental studies of singlet oxygen chemistry, the photodynamic properties of rose bengal have also been applied to problems such as killing the human immunodeficiency virus (HIV) [30], *Salmonella* bacteria [31], and the *Trypanosoma* protozoa responsible for the human diseases transmitted by the tsetse fly [32]. Many other applications, too numerous to list, have been found for rose bengal in chemistry, biology, and medicine. After 120 years rose bengal continues to be an important research subject and tool, as shown by the significant number of research articles that feature it prominently each year (Fig. 1.4).

1.7 Outline of the thesis

The second chapter of this thesis describes techniques for measuring triplet-triplet absorption spectra. Knowledge of the energies of the various higher-lying triplet states can be approximately determined from such spectra. Chapter Two concludes with an application of these techniques to the identification of a previously undescribed higher-lying triplet state of rose bengal. This state is the least energetic triplet state to be identified, excluding T_1 , so it will be called T_2 throughout this work. The T_2 state has an absorption cross section, $1.1 \times 10^{-16} \text{ cm}^2$ at 1064 nm, substantially greater than that found for the other triplet states

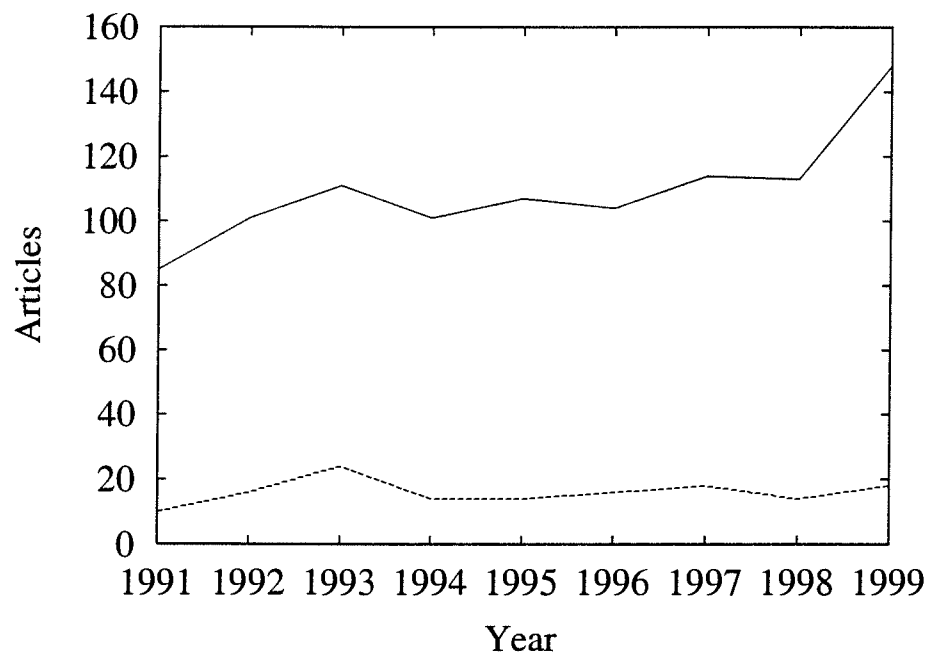


Figure 1.4: Rose bengal-related articles in the research literature (1991-1999). Publications containing “rose bengal” in their title, abstract, or list of keywords (—); publications containing “rose bengal” in their title (- - -). The numbers for 1999 are extrapolated from the first six months of that year. All information was obtained from *Science Citation Index* (Institute for Scientific Information).

and approaches that of the maximum ground state absorption, approximately $3.8 \times 10^{-16} \text{ cm}^2$ at 548 nm. Portions of this chapter appeared in a 1999 *Chemical Physics* article by Larkin *et al.* [33].

In Chapter Three the photophysical processes which follow excitation of higher-lying states are described in more detail. The focus of this chapter is reverse intersystem crossing, the transition from a higher-lying triplet state back to the singlet manifold. Two experimental techniques for measuring the quantum yield of this transition are introduced: two-step laser-induced bleaching and two-step laser-induced fluorescence. Experiments using the latter technique to determine reverse intersystem crossing yields for three higher-lying triplet states of rose bengal are then described. Those yields, as high as 12%, depend on the particular higher-lying state initially excited, contrary to the hypothesis of several previous workers in this field. Portions of this chapter appeared in a 1999 *Chemical Physics* article by Larkin *et al.* [33]. The analysis presented in that article has been revised in this chapter to include molecular orientation effects.

The possibility of photochemistry from the higher-lying triplet states is the topic of the fourth chapter. Oxygen-independent biological damage has been attributed to radicals formed following bond cleavage from such states. In this chapter, two-step laser-induced bleaching is used as an indicator of bond cleavage following excitation of the T_2 state of rose bengal. An upper limit of 0.0008 is found for the yield of photoproducts from this state. Work by other groups has found oxygen-independent damage following excitation of the T_3 state of rose bengal but not for the more energetic T_4 . A proposed explanation of this difference had been dissimilar yields of reverse intersystem crossing for these various states. This proposal was introduced in a talk by Larkin *et al.* at the 1998 meeting of the American Society for Photobiology [34]. In Chapter Four we quantitatively

investigate the effect of reverse intersystem crossing on radical formation yields using a kinetic model. This modeling suggests that reverse intersystem crossing can only account for a small fraction of the observed difference in biological effects. Finally, this chapter concludes with an analysis of the feasibility of two-step activated photodynamic therapy capable of producing oxygen-independent damage.

Chapter Five addresses simultaneous two-photon excitation of rose bengal. A commonly used fluorescence technique for determining the two-photon absorption cross section is described and then applied to determine this photophysical parameter for 1064-nm excitation of the ground state of rose bengal. A two-photon absorption cross section of 0.028 GM is found for 1064-nm excitation. Complicating effects due to reverse intersystem crossing are discussed, and its impact on the two-photon absorption cross section is demonstrated.

Chapter Six summarizes the results of the preceding chapters. Areas of future research are also suggested.

Appendix A discusses the importance of considering the orientation of molecules during photoexcitation. Analytical expressions for ground state depletion are presented for the cases of fast and slow rotation of the molecules. A computational approach appropriate for intermediate rotation rates is also described.

Chapter 2

Detection and excitation of higher-lying triplet states

The technique of flash photolysis was introduced in 1949 by Norrish and Porter [35,36] for studies of light-induced chemical reactions in which intermediate species were produced in concentrations comparable to the reactants. The study of short-lived transient species requires a means of providing an intense burst of exciting energy. Norrish and Porter found that flash lamps could provide pulses of light that were sufficiently bright to generate a significant concentration of transients, allowing the study of time scales on the order of microseconds. Phenomena lasting as short as femtoseconds can be studied if pulsed lasers are used instead of flash lamps. Reference [37] presents a recent overview of the contributions that flash photolysis has provided to our understanding of biologically-relevant excited states and free radicals.

2.1 Experimental methods

The two geometries available in a transient absorption experiment are illustrated in Fig. 2.1. These experiments require a pump beam to produce the excited state species to be studied and a probe beam to detect the change in absorption due to transfer of population from the ground state to one or more excited states. The probe beam may either be parallel or perpendicular to the pump beam. This chapter describes experiments conducted with both the in-line (probe parallel to pump) and right-angle (probe perpendicular to pump) geometries. In this work measurements performed using the in-line geometry will be called pump-probe experiments, and laser flash photolysis will primarily be understood to refer to measurements based on the right-angle geometry.

The primary advantage of the in-line geometry is that a relatively greater fraction of the absorbed pump photons create excited states in the probed volume. However, the small cross-sectional area makes achieving good overlap of the pump and probe beams throughout the sample more difficult. Another disadvantage is the problem of separating the pump and probe beams following the sample so that the absorption of the probe can be detected. For thin samples it is possible to have a larger deviation from perfect collinearity without compromising overlap within the sample. This allows for the beams to be separated spatially. For extended samples the overlap requirement greatly reduces the deviations from collinearity that can be tolerated. In this case it becomes more practical to separate the beams spectrally, rather than spatially. For broadband probes this separation becomes more problematic.

The right-angle geometry allows the pump and probe beams to be easily distinguished, making this technique particularly appealing for probes from broadband light sources. In this geometry the pump pulse is typically expanded so that

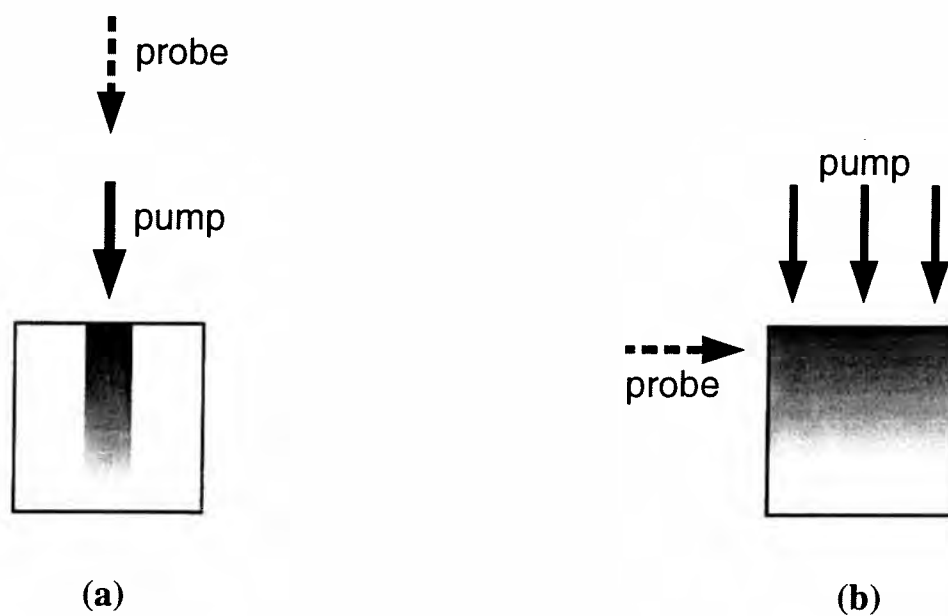


Figure 2.1: Schematic of transient absorption geometries, (a) in-line and (b) right-angle. Shading is suggestive of the spatial dependence of $[T_1]$ that could result if significant attenuation of the pump pulse occurs.

it excites a rectangular cross section of the sample, with the long axis of the rectangle along the direction of the probe's propagation. If the pump beam overfills a rectangular aperture an approximately homogeneous beam profile can be created. If this is true, the probe pulse sees a constant concentration of excited species, because the probe pulse traverses the sample perpendicular to the pump pulse. This eliminates the difficulties that can result from attenuation of the pump pulse as it propagates through the sample.

Although a long path length for the probe pulse can increase the sensitivity of the technique, it prevents its application to detection of ultrafast transients. For example, a 1-cm path length results in a transit time of approximately 40 ps through the sample. The triplet states which are the focus of the present chapter have lifetimes exceeding a microsecond, and therefore the measurements will not be significantly effected by this picosecond-scale temporal averaging.

2.1.1 In-line geometry

The experimental setup for the pump-probe measurements is shown in Fig. 2.2 and uses the symbols defined in Table 2.1. The 1064-nm light is the final output of a pulsed Nd:YAG laser system. The foundation of the laser system is a mode-locked Nd:YAG laser that generates a train of pulses at 76 MHz. Every 400 ms a single pulse is selected using an electro-optic switch and amplified using a regenerative amplifier followed by a flashlamp-pumped two-pass amplifier (both Nd:YAG). The final output of the system is a pulse containing up to 2 mJ with a pulse length of ~ 190 ps. This pulse is split at a beam splitter (BS1), which reflects 90% of the light. The transmitted light will become the probe pulse. The reflected fraction passes through a half-wave plate (WP) which is mounted in a computer-controlled rotary mount. The beam diameter is reduced by approximately a factor of 8 by

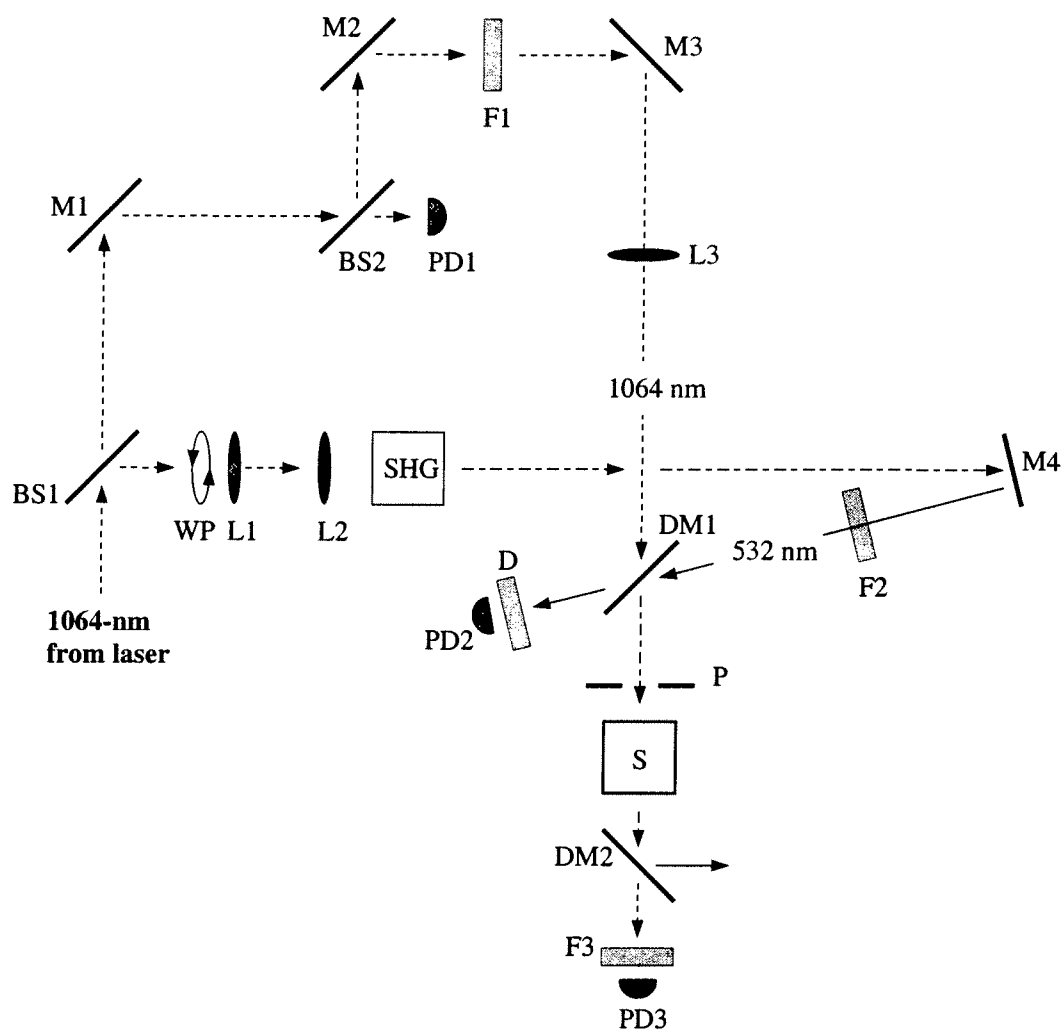


Figure 2.2: Experimental setup for pump-probe measurements. See Table 2.1 for symbol definitions.

Table 2.1: Equipment used in the pump-probe experiment

	Description	Details
BS1	beam splitter	90% reflection
BS2	beam splitter	35% reflection
D	diffuser	ground glass
DM1-2	dichroic mirror	R@532 nm, T@1064 nm
F1	neutral density filters	OD > 4
F2	short-pass filters	two KG3, one KG2 (Schott)
F3	interference filter	$\lambda_0 = 1064$ nm, $\Delta\lambda = 10$ nm
L1	lens	f = 100 mm
L2	lens	f = -12 mm
L3	lens	f = 400 mm
M1-3	mirror	1064 nm, 45°
M4	mirror	532 nm, 0°
P	pinhole	1 mm radius
PD1-3	photodiodes	EG&G, FND-100
S	sample cuvette	1-cm path length
SHG	second harmonic generation	KDP crystal
WP	half-wave plate	rotation computer controlled

lenses L1 and L2. This 1064-nm pulse then passes through a nonlinear crystal (SHG), producing the pump pulse, \mathcal{P}_1 , at the second harmonic ($\lambda = 532$ nm). The fraction of the 1064-nm pulse that is converted is dependent on the orientation of its polarization with respect to the optical axis of the nonlinear crystal. This angle is controlled by the half-wave plate, allowing computer-control of the energy in the pump pulse. This mixture of 532- and 1064-nm light is incident on a green-reflecting mirror (M4), removing light at the fundamental frequency from the reflected light. The spectral purity of the 532-nm pump pulse is enhanced by attenuating any residual light at the fundamental by passing the pulse through short-pass filters (F2). The \mathcal{P}_1 pulse is then reflected by a dichroic mirror (DM1) through a pinhole (P) before exciting the sample (S). After passing through the sample the pump pulse is reflected by a dichroic mirror (DM2) into a beam stop (not shown). A small fraction of the \mathcal{P}_1 light is transmitted through DM1 and then detected by a silicon photodiode (PD2), providing a monitor of the energy in the pump pulse. This monitor signal is calibrated by placing an energy meter (Molelectron, J50-LP) at the cuvette location.

The probe light is delayed by ~ 4 ns relative to the pump pulse by traversal of a greater optical path using mirrors M1-M3. This delay line contains a beam splitter (BS2) which reflects 35% of the probe light. The transmitted fraction is detected by a silicon photodiode (PD1), providing a monitor of fluctuations in the probe pulse energy. The probe light is further attenuated by neutral density filters (F1), reducing its energy by more than 10^4 . The probe light is transmitted through dichroic mirror DM1, passes through the sample, and is separated from \mathcal{P}_1 by dichroic mirror DM2. The probe light passes through an interference filter so that any residual pump light is eliminated. Finally, the probe pulse is detected by silicon photodiode PD3. The two probe monitor signals produced by PD1 and

PD3 are calibrated with the pump pulse blocked prior to the sample.

Signals from the photodiodes are captured using three gated integrators (Stanford Research Systems, 250), digitized (Stanford Research Systems, 240), and transferred to a computer via GPIB (general purpose interface bus). The transmission of each probe pulse is determined from PD1 and PD3 and recorded along with the corresponding pump energy obtained from PD2.

2.1.2 Right-angle geometry

The experimental setup for the laser flash photolysis measurements is shown in Fig. 2.3 using the symbols defined in Table 2.2. In this configuration the second-harmonic pulse ($\lambda = 532$ nm) is separated from the fundamental by a dichroic mirror (DM) with any residual light at the fundamental wavelength ($\lambda = 1064$ nm) further attenuated by a short-pass filter (F). The majority of this frequency-doubled pump pulse is focused by a cylindrical lens (CL) onto the masked sample cuvette, exciting a 2-mm by 10-mm cross sectional area. A small fraction of the pump pulse is reflected by a glass plate (BS) prior to the cylindrical lens, attenuated by neutral density filters, and then detected by a fast silicon photodiode (PD1). This signal is captured by a gated integrator (GI) and transferred to a computer. By removing the sample cuvette and placing an energy meter behind the beam mask, the pump pulse monitor signal measured by PD1 can be calibrated with respect to the energy reaching the sample. Transient absorption changes are probed by a broadband light beam traveling along the length of the irradiated zone (perpendicular to the pump pulse). The probe pulse has a 20-ms duration and is produced by a mercury lamp followed by a long-pass filter and fast mechanical shutter. This collection of elements is represented by PL in Fig. 2.3. The probe pulse passes through a monochromator (SP) before being detected by

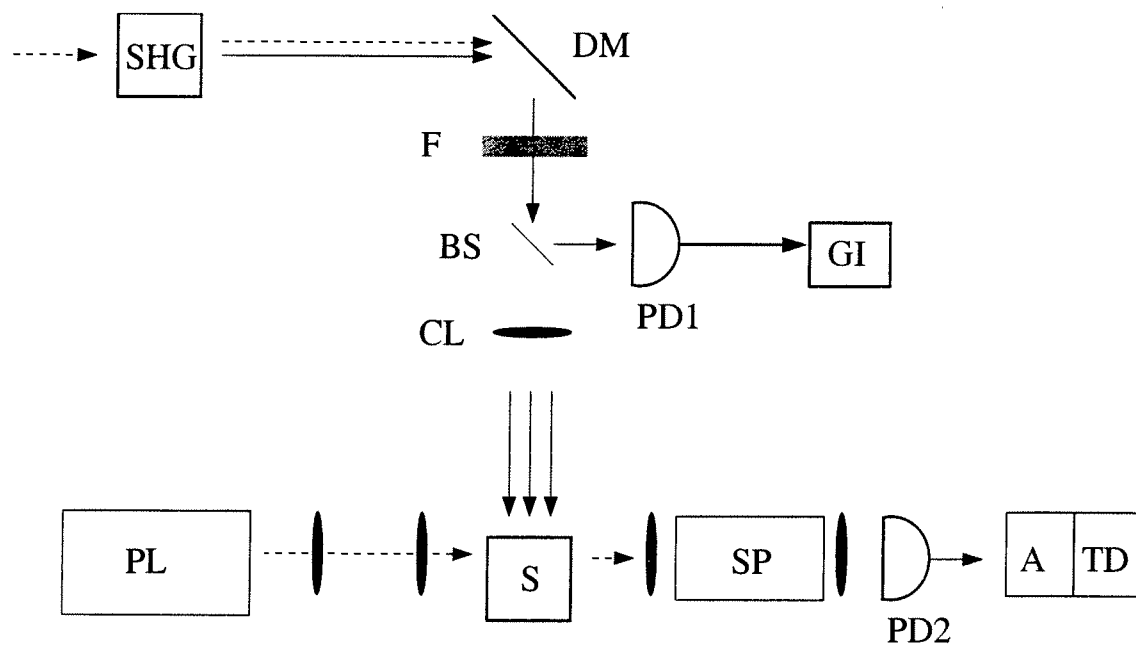


Figure 2.3: Experimental setup for laser flash photolysis measurements. See Table 2.2 for symbol definitions.

Table 2.2: Equipment used in the laser flash photolysis experiments

	Description	Details
A	fast amplifier	EG&G, 574
BS	glass plate (microscope slide)	
CL	cylindrical lens	
DM	dichroic mirror	R@532 nm, T@1064 nm
F	short-pass filter	Schott, KG3
GI	gated integrator	Stanford Research Systems, 250
PD1-2	silicon photodiodes	EG&G, FND-100
PL	mercury arc lamp fast shutter long-pass filter	Olympus, 100 W Vincent Assoc., Uniblitz VS25 Schott, RG695
S	sample cuvette and beam mask	1-cm path length
SHG	second harmonic generator	KDP crystal
SP	monochromator, 13 nm BW	Instruments SA, H20
TD	digitizing oscilloscope	Hewlett-Packard, HP54201A

a silicon photodiode (PD2). The photodiode signal is increased by a multistage amplifier (A) and then recorded by a digital oscilloscope (TD). The average signal from 64 shots is then transferred at 9-bit resolution to a computer for analysis.

2.1.3 Materials

Rose bengal was purchased from Sigma (St. Louis, MO) and used without further purification. All experiments were carried out in phosphate-buffered saline with a pH of 7. Effects of photobleaching were minimized by continuously stirring all samples with a micro-stirbar during irradiation. Samples were stored in the dark prior to use, and the laboratory was only dimly illuminated during the experiment. Dye concentrations were determined from ground state absorption spectra obtained using a Perkin-Elmer Lambda 9 UV/VIS/NIR spectrophotometer and $\epsilon_{s_0} = 47200 \text{ M}^{-1} \text{ cm}^{-1}$ at 532 nm [14]. In the pump-probe experiments the sample had a concentration of $\sim 65 \mu\text{M}$.

2.2 Analytical methods

It is necessary to determine the concentration of molecules in the triplet state in order to extract a triplet-triplet absorption cross section from transient absorption measurements obtained using flash photolysis or pulse radiolysis. Additional complications enter into the calculation of the triplet-triplet absorption cross section, $\sigma_{T_1T_n}$, if there is overlap with the ground state absorption spectrum. Many methods of analyzing transient absorption data have been used throughout the history of triplet state studies. In their exhaustive review, Carmichael and Hug describe in detail seven of these methods, with an additional five covered in less depth [38]. See this review for additional discussion of these methods, historic

analysis of their use, and a more than 200 page compilation of triplet extinction coefficients for organic molecules reported in the literature between 1950 and 1984.

2.2.1 Total depletion method

The method of total depletion is based on the premise that complete conversion of the molecules from the ground state, S_0 , to the lowest triplet state, T_1 , can be achieved given a sufficiently large excitation fluence. If complete conversion is achieved then the concentration of triplets is equal to the total concentration of the molecules, a quantity that can be more easily determined. If the intermediate S_1 state is ignored, a simple two population model of the system is described by

$$\frac{dp_{T_1}}{dt} = \Phi_{isc} \sigma_{S_0 S_1} I p_{S_0} \quad (2.1)$$

where $\sigma_{S_0 S_1}$ is the ground state absorption cross section, I is the photon flux, Φ_{isc} is the quantum yield of $S_1 \rightarrow T_1$ intersystem crossing, and p_{S_0} and p_{T_1} are the population densities of the states S_0 and T_1 . Solving this simple model gives

$$[T_1] = (1 - e^{-\sigma_{S_0 S_1} \Phi_{isc} F}) C \quad (2.2)$$

where F is the photon fluence, $[T_1]$ is the concentration of triplet molecules immediately following the excitation pulse, and C is the total concentration of the species being studied.

Many details of the true kinetics are ignored by this model, including relaxation of the triplet state. Therefore it is necessary to remember that the fluence required for saturation must be delivered in a time much less than that of the triplet lifetime, τ_{T_1} . However, as the pulse length is reduced the existence of the intermediate state S_1 can no longer be ignored. The complications introduced by this state have been examined, and it was found that complete conversion can only be achieved if the singlet lifetime, τ_{S_1} , is sufficiently short [39]. More specifically,

for the case of a square pulse the conversion of 95% of the ground state can only be achieved when

$$\frac{2\tau_{S_1}}{\Phi_{isc}} \leq \Gamma \leq \frac{\tau_{T_1}}{20}, \quad (2.3)$$

where Γ is the length of the pulse. These requirements suggest that the method of total depletion can only be successfully applied when a sufficient fluence, $3/(\Phi_{isc}\sigma_{S_0S_1})$ for 95% conversion, can be delivered in this restricted pulse length range. In the case of air-saturated aqueous solutions of rose bengal, the pulse lengths for which the total depletion approximation is applicable are between approximately 180 ps and 150 ns.

It might be believed that confidence in achieving complete conversion could be assured if the transient absorption does not continue to grow with increasing fluence. However, effects other than ground state depletion can lead to the same appearance of saturation. For example, photoselection effects become important if the pulse length is not much greater than the rotational diffusion time of the molecules. Appendix A discusses this particular effect on ground state depletion in more detail. In addition, multiphoton effects, either simultaneous or sequential, become increasingly likely at the high fluences required to achieve total depletion.

2.2.2 Partial saturation method

The partial saturation method addresses some of the problems associated with the method of total depletion [40]. Using the same simple two-level model as before, the change in absorption, ΔA , at a particular wavelength is given by

$$\Delta A = a(1 - e^{-bF}) \quad (2.4)$$

with

$$a = (\epsilon_{T_1} - \epsilon_{S_0})\ell C \quad (2.5)$$

$$b = \Phi_{\text{isc}} \sigma_{\text{S}_0\text{S}_1} \quad (2.6)$$

where ℓ is the path length of the transient absorption probe and the ϵ_i are the extinction coefficients of the corresponding states. The absorption cross section is related to the extinction coefficient by

$$\sigma(\text{cm}^2) = 3.82 \times 10^{-21} \epsilon(\text{M}^{-1} \text{cm}^{-1}). \quad (2.7)$$

If both the intersystem crossing yield and the triplet absorption cross section are unknown then the partial saturation method may allow both to be determined from the variation of ΔA with F . The upper end of the range of fluences used must be sufficient to achieve at least partial saturation, hence the name of the technique. If only low fluences are used, Eq. (2.4) can be approximated by $\Delta A \approx abF$ making Φ_{isc} and ϵ_{T_1} indistinguishable.

Although the partial saturation method does address some of the limitations of the method of total depletion, it is still plagued by the fact that ground state depletion is not the only cause of saturation. As mentioned earlier, the effects of photoselection and rotational motion discussed in Appendix A are an example of such complicating factors.

2.2.3 Pulsed fluence variation

The pulsed fluence variation method¹ requires an accurate knowledge of several photophysical parameters, but when those are known it has the advantage of allowing the triplet extinction to be determined from the dependence of absorbance on fluence in the low fluence regime. In particular, it is possible to avoid the complications associated with partial or total depletion of the ground state. In the low fluence limit the difference in absorbance shortly after the excitation pulse

¹Called pulsed intensity variation by Carmichael and Hug [38].

is given by

$$\Delta A(\lambda) = [\epsilon_{T_1}(\lambda) - \epsilon_{S_0}(\lambda)]\ell C\Phi_{isc}\sigma_{S_0S_1}F \quad (2.8)$$

where the low fluence condition is satisfied when $\sigma_{S_0S_1}F \ll 0.1$. Violation of this condition will result in a deviation from the linear dependence of ΔA on F . The triplet extinction can be determined from the slope of this line if accurate values of Φ_{isc} and ϵ_{S_0} are available. Additional constraints are that the pulse length must be much less than the T_1 lifetime and ΔA should be measured after S_1 has relaxed.

This equation can be extended so that it can be used to analyze pump-probe measurements on samples of greater absorbance where pump attenuation becomes significant. The number of triplets in the excitation volume is given by

$$N_T = \Phi_{isc}(1 - 10^{-A_g})E \quad (2.9)$$

where A_g is the absorbance of the unexcited sample at the pump wavelength and E is the number of photons in the pump pulse. This can be simply converted to a molar concentration such that

$$[T_1] = \frac{1000N_T}{a\ell N_A} \quad (2.10)$$

where a is the cross sectional area (in cm^2) of the pump pulse as it travels through the sample and N_A is Avogadro's number. If the transient absorbance is due solely to the triplet state we find

$$\begin{aligned} \Delta A &= \epsilon_{T_1}[T_1]\ell \\ &= \frac{1000}{N_A}\Phi_{isc}(1 - 10^{-A_g})\epsilon_{T_1}F \end{aligned} \quad (2.11)$$

where F is the photon fluence (units of photons cm^{-2}) and ϵ_{T_1} is in units of $\text{M}^{-1} \text{cm}^{-1}$.

Pulsed fluence variation is difficult to apply with conventional flash photolysis which uses broadband flash lamps to create the triplets. In this case the $\sigma_{S_0S_1}F$ term in Eq. (2.8) is more appropriately written as

$$\sigma_{S_0S_1}F = \int \sigma_{S_0S_1}(\lambda_{ex})F(\lambda_{ex})d\lambda_{ex} \quad (2.12)$$

where the integral is taken over the wavelength range of the excitation pulse. Any variation in the spectral distribution of the lamp with time must be carefully monitored. Light sources which have a bandwidth narrow compared to the rate of variation in $\sigma_{S_0S_1}(\lambda_{ex})$ will not suffer from this complication. Many lasers can satisfy this condition for the relatively broad absorption bands of dyes in solution.

As noted above, application of this method requires accurate knowledge of Φ_{isc} and ϵ_{S_0} . Particular care must be taken because these photophysical parameters are well known to exhibit significant solvent-dependent variations. As an example of the variations observable in absorption and emission spectra and the rates of radiative and non-radiative transitions, see the work of Fleming *et al.* [15]. In the case of rose bengal they observed a shift in the absorption maximum from 548 nm to 561 nm in changing the solvent from water to isopropanol.

2.3 Results and discussion

The methods of total depletion and partial saturation are difficult to implement with rose bengal in water for the pulse lengths available from the Nd:YAG laser used in these experiments. As is discussed in more detail in Appendix A, rose bengal has a rotational diffusion time comparable to the laser pulse length, causing significant deviations from the simple exponential depletion model assumed by the total depletion and partial saturation methods. Therefore, the pulsed fluence variation method was used to analyze the data obtained in both the pump-probe

and flash photolysis measurements. Rose bengal has been extensively studied, and the photophysical parameters required to use this method are known. Both studies examined the transient absorption of light at wavelengths greater than 650 nm. Ground state rose bengal does not absorb in this region, as shown in Fig. 2.4.

The change in absorbance at 1064 nm observed in the pump-probe experiment is shown in Fig. 2.5. There is a clear deviation from linearity at higher energies. In order to extract ϵ_{T_1} from this data using Eq. (2.11) it is necessary to select only the linear region. However, it is difficult to clearly delineate the extent of this region. The variation in the value of ϵ_{T_1} obtained from fits to the first ν points in the data is shown in Fig. 2.6. There is a plateau from approximately $\nu = 11$ to 16, corresponding to the region of linear response ending at approximately 33 μJ . In this region $\epsilon_{T_1}(1064 \text{ nm}) \approx 32670 \text{ M}^{-1} \text{ cm}^{-1}$, corresponding to a triplet-triplet absorption cross section of $1.25 \times 10^{-16} \text{ cm}^2$. The fit with the least χ^2 in its data subset occurs at $\nu = 6$ and gives an extinction of $30830 \text{ M}^{-1} \text{ cm}^{-1}$ ($\sigma_{TT} = 1.18 \times 10^{-16} \text{ cm}^2$). A fit based on this value systematically underestimates the change in absorbance between $\nu = 7$ and 22 (dashed curve in Fig. 2.5). Depletion effects will result in deviations from a linear increase in the observed ΔA at high fluences. Therefore it is expected that the fit should be good at low fluences but overestimate ΔA at higher fluences. The larger value of ϵ_{T_1} (solid curve in Fig. 2.5) produces this expected behavior.

The near-infrared triplet-triplet absorption spectrum of rose bengal obtained using laser flash photolysis is shown in Fig. 2.7. The triplet absorption was calculated using the known ground state absorption, concentration of the sample, and energy of the excitation pulse. Detector limitations (silicon photodiode) prevented the extension of this spectrum beyond 1100 nm. Interpolating between the values

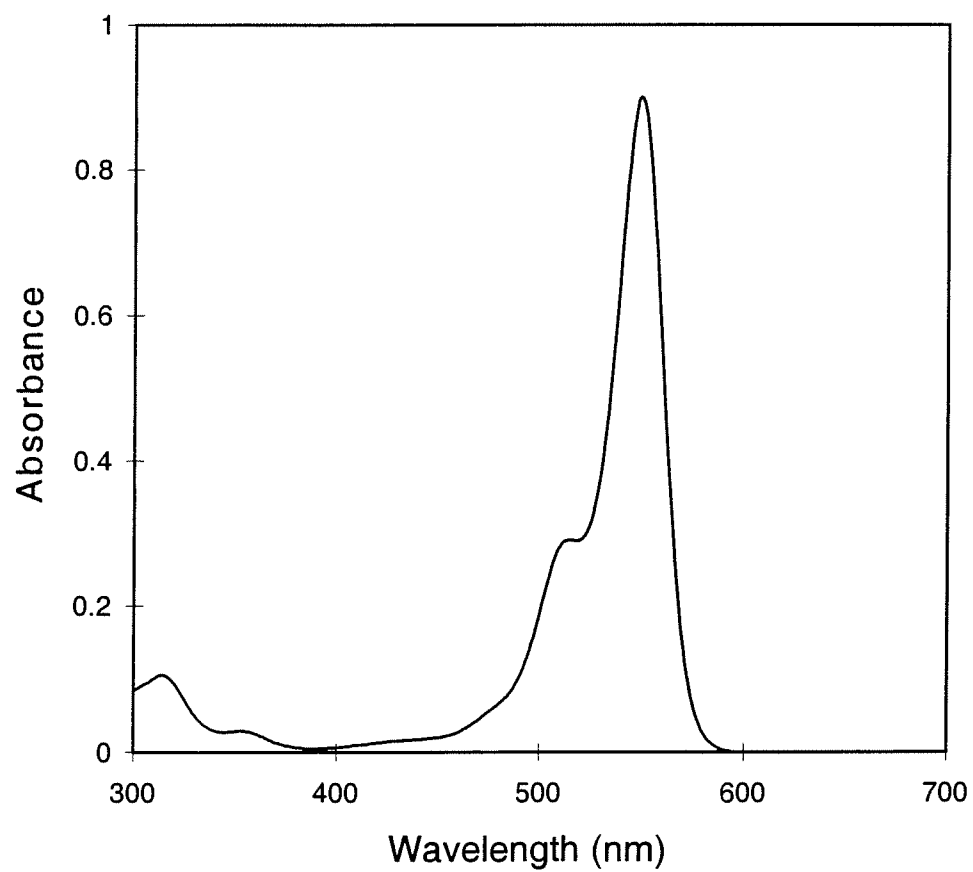


Figure 2.4: Ground state absorption spectrum of 1 μM rose bengal in phosphate-buffered saline (pH 7).

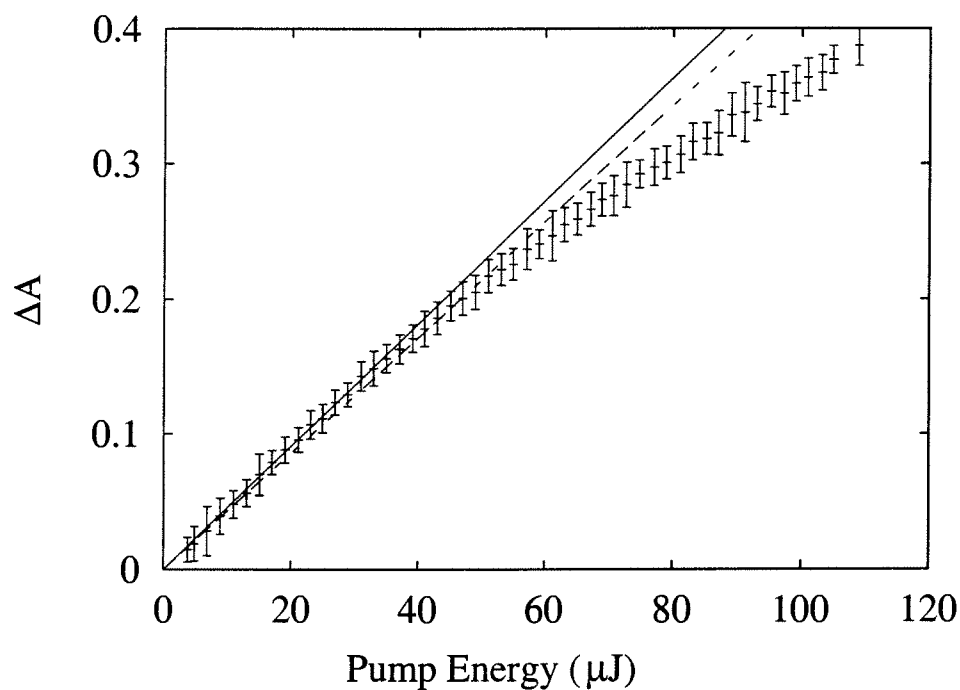


Figure 2.5: Pump-probe measurements of 1064-nm absorption by T_1 state of rose bengal. Pump wavelength: 532 nm. Probe wavelength: 1064 nm. Pump-probe delay: ~ 4 ns. Experimental data (+); Eq. (2.11) with $\epsilon_{T_1} = 32670 \text{ M}^{-1} \text{ cm}^{-1}$ (—); Eq. (2.11) with $\epsilon_{T_1} = 30830 \text{ M}^{-1} \text{ cm}^{-1}$ (- - -). Error bars indicate the standard deviation of 64 measurements.

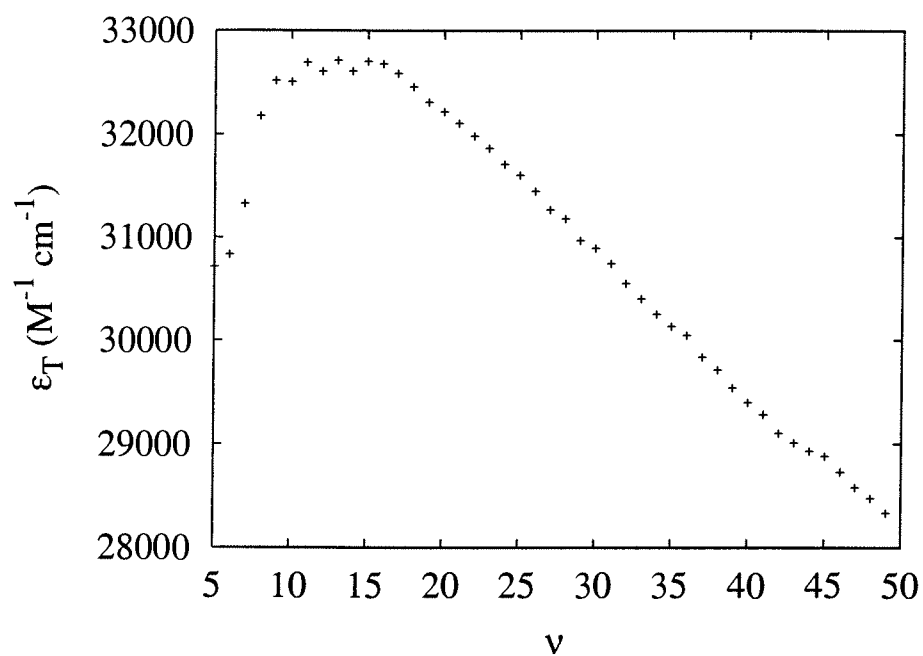


Figure 2.6: Dependence of triplet extinction fit on choice of data subset. Crosses (+) represent best fits of Eq. (2.11) to the first ν data points in the pump-probe transient absorption data shown in Fig. 2.5.

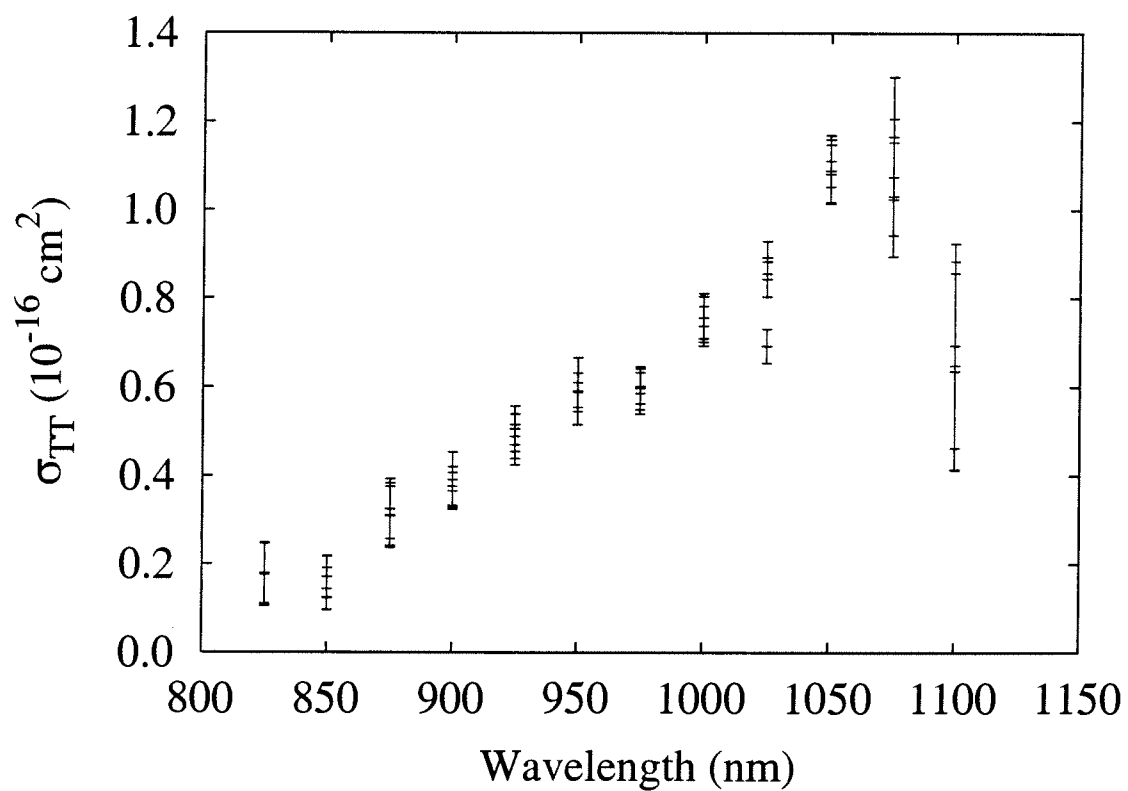


Figure 2.7: Rose bengal near-infrared triplet-triplet absorption spectrum. Error bars indicate the standard deviation in four sets of measurements based on 64 shot averages.

found at 1050 nm and 1075 nm gives an estimated triplet-triplet absorption cross section at 1064 nm of $(1.1 \pm 0.1) \times 10^{-16} \text{ cm}^2$ or in terms of an extinction coefficient $\epsilon_{T_1}(1064 \text{ nm}) = 28800 \text{ M}^{-1} \text{ cm}^{-1}$. The right-angle geometry is expected to be more accurate so this value of the triplet-triplet absorption cross section will be the one used in later parts of this work. This value is nearly identical to the absorption cross section, $1.18 \times 10^{-16} \text{ cm}^2$, found using the in-line geometry.

2.4 Discussion

To the best of our knowledge, this represents the first measurement of the triplet-triplet absorption cross section of rose bengal in the near infrared (800 - 1100 nm). The triplet-triplet absorption near 1064 nm is comparable to the ground state absorption ($1.8 \times 10^{-16} \text{ cm}^2$ at 532 nm), in contrast to the case between 600 and 680 nm where the cross section ranges between 6.4×10^{-18} and $1.3 \times 10^{-17} \text{ cm}^2$ [41]. The near infrared portion of the spectrum is of considerable interest for various reasons. On the positive side, near infrared light has the most favorable transport properties in biological tissue, and therefore exploitation of any biological effects resulting from excitation of higher-lying states will benefit from the ability to deliver this light efficiently. A negative effect may be that this complicates the use of multiphoton microscopy, which most commonly requires intense infrared light. Following the initial excitation of the dye through a multiphoton process the triplet state may be subsequently excited by the same light through a single photon process. This has the potential to create undesirable effects associated with the higher-lying states. Knowledge of the triplet-triplet absorption spectrum represents a critical first step towards understanding and controlling these effects.

Chapter 3

Intersystem crossing from higher-lying triplet states

3.1 Background

Although intersystem crossing has been identified primarily with transitions from the lowest excited singlet state of a molecule to an even lower-lying triplet state, intersystem crossing between other states may also occur. Well-known examples of triplet to singlet intersystem crossing include E- and P-type delayed fluorescence [42, 43]. E-type delayed fluorescence, also known as delayed thermal fluorescence, is observed when thermal activation causes population transfer from T_1 back to the more energetic S_1 state. The strength of E-type delayed fluorescence is strongly temperature dependent, and its lifetime reflects that of T_1 . The origin of this long-lived luminescence was first identified definitively in eosin (tetrabromofluorescein), hence the name E-type [44]. The other delayed fluorescence, P-type, occurs when the activation energy for transfer of the T_1 population back to singlet manifold is provided by triplet-triplet energy transfer. The strength of P-type delayed

fluorescence increases quadratically with the triplet concentration. The origin of this long-lived luminescence was first identified definitively in pyrene, hence the name P-type. The spectra of prompt fluorescence and both types of delayed fluorescence are identical since they all represent transitions from S_1 to S_0 .

Intersystem crossing may also occur from higher-lying triplet states where intersystem crossing to the singlet manifold competes with direct internal conversion to the lowest triplet state. This triplet-to-singlet transition has been called reverse intersystem crossing (RISC) in order to distinguish it from the more common S_1 to T_1 transition. Historically this process has received little attention since it has been believed to be an extremely improbable transition compared to internal conversion back to T_1 . This is an application of Vavilov's rule, which states that the yield of emission is independent of the state excited, implying that internal conversion is the only process occurring from a higher-lying state [45]. A related rule proposed by Kasha states that emission occurs only from the lowest excited state of a particular multiplicity. In other words, relaxation through internal conversion will predominate over emission from a higher-lying state [46]. Exceptions to Kasha's and Vavilov's rules are known to exist. For example, azulene predominantly exhibits $S_2 \rightarrow S_0$ fluorescence [47, 48]. This anomalous emission occurs because $S_2 \rightarrow S_1$ internal conversion is inhibited by an unusually large energy gap.

The conditions for significant reverse intersystem crossing are similar to those for $S_1 \rightarrow T_1$ intersystem crossing that were described in Chapter 1. The prohibition of intermultiplicity transitions must be weakened by the heavy atom effect, and a small energy gap between the two states is required for significant overlap between their vibrational manifolds. Efficient reverse intersystem crossing requires a smaller intermultiplicity energy gap than for $S_1 \rightarrow T_1$ intersystem crossing be-

cause other relaxation channels (radiation and internal conversion) are slower for S_1 than for the higher-lying states.

3.2 Measurement techniques for determining reverse intersystem crossing yields

A review of the literature reveals that studies of intersystem crossing from higher-lying triplet states have typically relied on two-step laser excitation to populate these energetic states [49–60]. Either time-resolved fluorescence or the transient absorption have been measured during two-step laser excitation, and with the appropriate analysis these have been used to determine the quantum yield of reverse intersystem crossing, Φ_{risc} . In this section the population dynamics induced by two-step laser excitation will be described, and the techniques for measuring RISC yields will be introduced. The two pulses of light used to excite the higher-lying triplet state may have the same wavelength, but for the sake of simplicity the dynamics described here are based on the assumption that they have different wavelengths. In particular, the ground state of the dye is assumed to be transparent to the second pulse.

Two-step laser excitation of the dye can result in transient changes in its absorption as well as the emission of fluorescence. The first pulse of light, \mathcal{P}_1 , is absorbed by the ground state of the molecule and directly or indirectly populates the lowest excited singlet state, S_1 . This state can relax radiatively to the ground state producing fluorescence. Alternatively it can undergo intersystem crossing to the lowest triplet state, T_1 . Ideally the second pulse, \mathcal{P}_2 , is delayed so that it arrives after S_1 has depopulated but before T_1 has relaxed substantially. The \mathcal{P}_2 light is absorbed by T_1 and populates a higher-lying triplet state, T_n , where

$n > 1$. This state can relax through internal conversion back to T_1 or through reverse intersystem crossing to a less energetic singlet state, S_m , where $m \geq 1$. Population in S_m rapidly decays to S_1 , where it can subsequently fluoresce or return to T_1 . The fluorescence method for determining the reverse intersystem crossing yield compares the magnitude of the fluorescence induced by \mathcal{P}_2 with the prompt fluorescence due to \mathcal{P}_1 . The absorption technique monitors the change in T_1 population induced by \mathcal{P}_2 through measurements of the absorption due to this state. We will refer to these techniques as two-step laser-induced fluorescence (TSLIF) and two-step laser-induced bleaching (TSLIB), respectively.

3.2.1 Two-step laser-induced bleaching

The yield of reverse intersystem crossing can be determined from the \mathcal{P}_2 -induced bleaching of the T_1 absorption. This bleaching results from the fraction of the population undergoing RISC which does not subsequently return to T_1 from the singlet manifold. In particular, we are interested in relating the fractional change in absorbance, $\Delta A/A_0$, to the $T_n \rightarrow S_m$ intersystem crossing yield, Φ_{risc, T_n} . A_0 is the absorbance due to T_1 immediately following \mathcal{P}_1 and ΔA is the change in absorbance measured after the relaxation of the sub-nanosecond transient caused by \mathcal{P}_2 . An idealized two-step laser-induced bleaching signal is shown in Fig. 3.1.

A_0 is proportional to the concentration of T_1 produced by \mathcal{P}_1 , $[T_1]_{\mathcal{P}_1}$, such that

$$A_0 = \epsilon_T [T_1]_{\mathcal{P}_1} \ell \quad (3.1)$$

where ℓ is the absorption probe pathlength. The concentration of T_n immediately following \mathcal{P}_2 is $[T_n]_{\mathcal{P}_2} = \sigma_{T_1 T_n} F_2 [T_1]_{\mathcal{P}_1} = \sigma_{T_1 T_n} F_2 A_0 / (\epsilon_T \ell)$, assuming that the delay between \mathcal{P}_1 and \mathcal{P}_2 is short compared to the T_1 lifetime. The photon fluence of \mathcal{P}_2 is given by F_2 and $\sigma_{T_1 T_n}$ is the triplet-triplet absorption

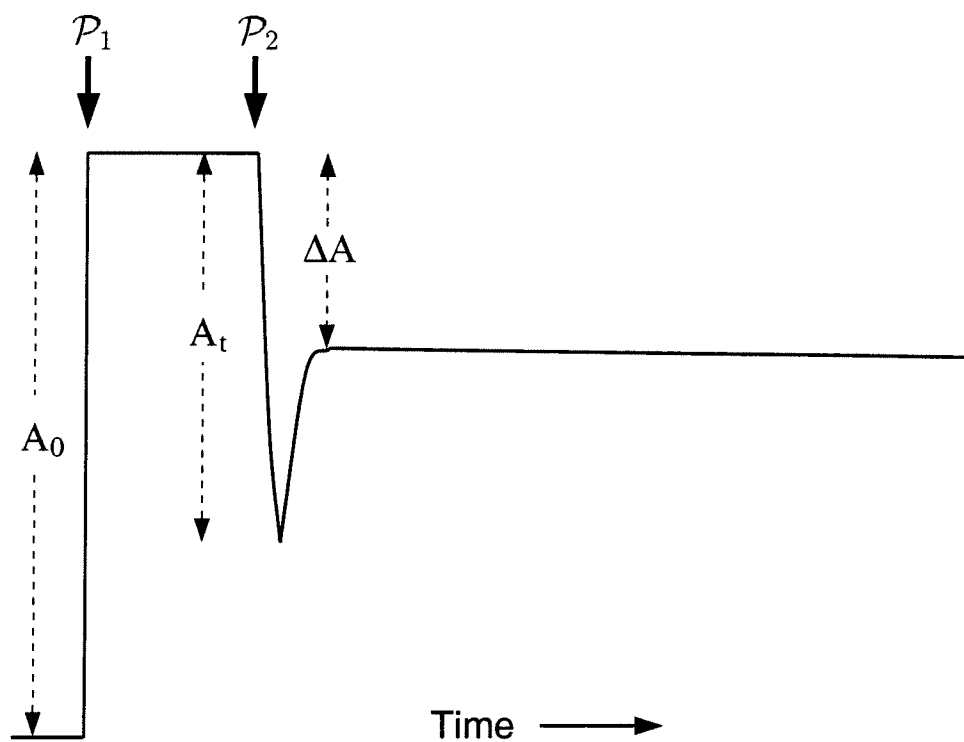


Figure 3.1: Idealized two-step laser-induced bleaching signal. Labeled arrows denote the arrival times of the two pump pulses. A_0 is the absorbance due to T_1 after \mathcal{P}_1 . Excitation of higher-lying triplet states by \mathcal{P}_2 depletes T_1 , producing an absorbance change, A_t . If some fraction of the excited population does not return to T_1 , a bleaching ΔA will be observed.

cross section. Reverse intersystem crossing from T_n populates S_m such that $[S_m]_{\mathcal{P}_2} = \Phi_{\text{risc}, T_n} [T_n]_{\mathcal{P}_2} = \Phi_{\text{risc}, T_n} \sigma_{T_1 T_n} F_2 A_0 / (\epsilon_T \ell)$ and the remainder of the population excited to T_n is assumed to return to T_1 through internal conversion. The S_m state is also assumed to relax with unity yield to S_1 which then returns to T_1 with a yield Φ_{isc} . The change in absorbance ΔA is due to the population which does not return to T_1 , giving

$$\begin{aligned} \Delta A &= -(1 - \Phi_{\text{isc}}) [S_1]_{\mathcal{P}_2} \epsilon_T \ell \\ &= -(1 - \Phi_{\text{isc}}) \Phi_{\text{risc}, T_n} \sigma_{T_1 T_n} F_2 A_0 \end{aligned} \quad (3.2)$$

which is easily rewritten in the form

$$\frac{\Delta A}{A_0} = -(1 - \Phi_{\text{isc}}) \Phi_{\text{risc}, T_n} \sigma_{T_1 T_n} F_2 . \quad (3.3)$$

One of the approximations implicit in this derivation was that \mathcal{P}_2 did not significantly deplete T_1 .

Reverse intersystem crossing is not the only process that can result in a decrease of the T_1 population following excitation of the higher-lying triplet state. As will be discussed in more detail in Chapter 4, photochemical reactions can also result in a reduction of the T_1 population. One approach that has been suggested as a means of verifying the photophysical rather than photochemical nature of the bleaching is to also monitor the change in ground state absorption. If reverse intersystem crossing is the only process occurring from the higher-lying triplet state, the decrease in T_1 population will equal the increase in S_0 population.

3.2.2 Two-step laser-induced fluorescence

In addition to the transient bleaching method described above, the reverse intersystem crossing quantum yield can also be determined from time-resolved fluorescence measurements. The integrated, \mathcal{P}_1 -induced prompt fluorescence, f_1 , is

proportional to the population excited to S_1 and is therefore given by

$$f_1 = a\sigma_{S_0S_1}F_1 \quad (3.4)$$

where a accounts for the fluorescence yield as well as factors associated with the experimental collection and detection of the light, $\sigma_{S_0S_1}$ is the ground state absorption cross section, and F_1 is the photon fluence of \mathcal{P}_1 . The repopulation of S_1 following the \mathcal{P}_2 pulse will result in a second emission of fluorescence. The integrated fluorescence following \mathcal{P}_2 , denoted by f_2 , depends on the yield of reverse intersystem crossing, Φ_{risc,T_n} , such that

$$f_2 = a\Phi_{\text{isc}}\Phi_{\text{risc},T_n}\sigma_{S_0S_1}F_1\sigma_{T_1T_n}F_2 \quad (3.5)$$

as can be shown through a derivation similar to that in §3.2.1. The two-step laser-induced fluorescence ratio f_R is defined by $f_R \equiv f_2/f_1$. Calculating this ratio using Eq. (3.4) and (3.5) we find that

$$f_R = \Phi_{\text{isc}}\Phi_{\text{risc},T_n}\sigma_{T_1T_n}F_2. \quad (3.6)$$

This ratio has the advantage of eliminating the need to measure a , a factor dependent on the particulars of the detection system. An idealized two-step laser-induced fluorescence signal is shown in Fig. 3.2.

3.2.3 Discussion of the Φ_{risc} measurement techniques

The reverse intersystem crossing yield measurement techniques described above are generally applicable, but the analytical expressions that were introduced in §3.2.1 and §3.2.2 must be used with care. One important assumption used in the derivation of Eq. (3.3) and (3.6) is that the population excited from T_1 to T_n is linearly proportional to $\sigma_{T_1T_n}F_2$. This condition is satisfied only while $[T_1] \gg [T_n]$. A common guideline that has been applied to the similar case

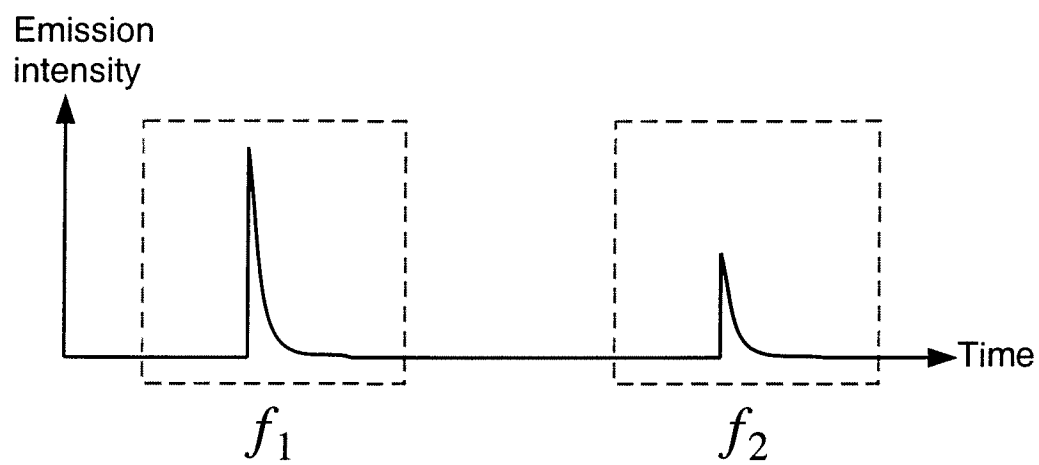


Figure 3.2: Idealized two-step laser-induced fluorescence signal. The fluorescence emissions due to the two pump pulses are indicated by f_1 and f_2 .

of ground state excitation is that $\sigma_{S_0S_1}F_1 \ll 0.1$. This fails to account for the effects of excited state relaxation, implicitly assuming that the excitation pulse is short compared to this time scale. Since the lifetime of T_n (\sim ps) is typically much shorter than that of S_1 (\sim ns), a more appropriate guideline in the case of excitation of higher-lying triplet states might appear to be $\sigma_{T_1T_n}F_2\tau_{T_n}/\tau_2 \ll 0.1$ where τ_{T_n} is the lifetime of the state T_n and τ_2 is the length of \mathcal{P}_2 . However, this fails to account for any photobleaching and thus the original, more conservative guideline would be more prudent. Beyond this limit a more complete model is required and frequently does not permit an analytic solution.

A popular method of calculating the excited state concentration uses actinometric techniques¹. This approach is prevalent in the laser flash photolysis community where several well-characterized molecules serve as actinometric standards for studies of long-lived triplet states. Such techniques must be carefully applied in studies of higher-lying states since another consequence of the short higher-lying state lifetime is the ease of exciting a single molecule to T_n multiple times during a single excitation pulse. In other words, values of $\sigma_{T_1T_n}F_2$ greater than 1 can be achieved if $\tau_2 > \tau_{T_n}$. In order to report such high-fluence effects appropriately, an actinometric standard with an absorption cross section significantly less than that of the species being studied must be selected so that it does not exhibit the effects of ground state depletion at these fluences.

Another approach that might be considered for quantification of the population excited to T_n involves measuring the relative change in T_1 absorption immediately following excitation by \mathcal{P}_2 . This would seem to be an ideal approach since it would correctly account for depletion effects. However, at best it can only

¹Actinometry is a technique for determining the number of photons in a pulse of light through the measurement of products resulting from a photophysical or photochemical reaction with a known quantum yield.

report the maximum instantaneous T_n population. Since it ignores all multiple-excitation effects this technique can be correctly applied only when $\tau_2 \ll \tau_{T_n}$. This approach is constrained even in that case since the transient absorption detection system must be capable of measuring the initial change in T_1 absorption following \mathcal{P}_2 -excitation. This transient decays with a lifetime of τ_{T_n} , necessitating a picosecond detector response, faster than is common for many laser flash photolysis systems.

When the experimental details outlined above can be satisfied for either technique, other considerations may influence which of these methods is selected for a specific measurement. In particular, the yield of $S_1 \rightarrow T_1$ intersystem crossing affects whether TSLIB or TSLIF is optimal for the particular molecule being studied. From Eq. (3.3) and Eq. (3.6) it can be seen that $\Delta A/A_0 \propto (1 - \Phi_{isc})$ whereas $f_R \propto \Phi_{isc}$. This suggests that the bleaching technique will be more favorable when $\Phi_{isc} < 0.5$ and two-step laser-induced fluorescence is to be preferred when $\Phi_{isc} > 0.5$.

3.3 Prior work

A review of the reverse intersystem crossing literature is presented in this section. This review is divided into three parts: studies in which molecules had reverse intersystem crossing yields less than 1%, studies reporting yields greater than 1%, and studies of reverse intersystem crossing in rose bengal. A summary of these studies appears in Table 3.1 at the end of this section.

3.3.1 Low-yield results

It appears that the earliest measurements of intersystem crossing from an excited triplet state back to the singlet manifold were reported by Keller in 1969 [49]. Keller used two-step excited fluorescence to study this process in naphthalene- d_8 , naphthalene- h_8 , quinoline, isoquinoline, fluorene, benzene, phenanthrene- d_{10} , triphenylene, and carbazole. Instead of using pulsed lasers, a system of shutters and filters was used to create the two-step excitation from a steady-state lamp. A reverse intersystem crossing yield of 5×10^{-7} was determined for naphthalene- d_8 , with naphthalene- h_8 approximately three times smaller. Two-step excited fluorescence was observed from quinoline, isoquinoline, and fluorene and was estimated to result from approximately the same order of magnitude reverse intersystem crossing yield as naphthalene. Benzene produced weak two-step excited fluorescence, but no estimates were made of the reverse intersystem crossing yield. The weak fluorescence was attributed to weak triplet-triplet absorption. No two-step excited fluorescence was observed from phenanthrene- d_{10} , triphenylene, and carbazole.

Anthracene and two derivatives (9-methyl-anthracene and 9-phenyl-anthracene) were studied by Kobayashi *et al.* in 1976 using a method based on fluorescence detection following two-step excitation [50]. Two-step excitation was produced by a flash lamp followed by a pulse from a ruby laser. The first pulse did not excite the anthracenes directly, but rather excited eosin which was also present in the sample. Energy transfer from eosin populated the T_1 state of the anthracenes, circumventing their low $S_1 \rightarrow T_1$ intersystem crossing yield. The second pulse excited higher-lying triplets but also produced fluorescence through two-photon excitation of S_0 . The contribution of two-photon excited fluorescence was found by also measuring the fluorescence in the case where the triplet state was not

populated prior to the laser pulse. Using a previously determined two-photon absorption cross section for anthracene, the two-photon excited fluorescence served as a reference for the collection and detection efficiency of the experimental system. The reverse intersystem crossing yields determined in these experiments were 4.5×10^{-6} , 6.1×10^{-5} , and 8.3×10^{-5} for anthracene, 9-methyl-anthracene, and 9-phenyl-anthracene, respectively.

One of the most detailed reports of two-step laser-induced fluorescence is the 1994 work of Tokumura *et al.* with 2,2'-bipyridine-3,3'-diol [57]. This represents a more complex system than discussed previously. The ultraviolet \mathcal{P}_1 pulse excited the S_1 state. Excited-state double-proton transfer produced the lowest-lying excited tautomer² singlet state, which they denoted as S'_1 . Intersystem crossing from S'_1 produced T'_1 . A higher-lying triplet state of the tautomer was excited by \mathcal{P}_2 , a pulse with a wavelength of approximately 670 nm. Reverse intersystem crossing repopulated the singlet manifold and resulted in $S'_1 \rightarrow S'_0$ fluorescence. Tokumura *et al.* demonstrated that this fluorescence does not occur if the \mathcal{P}_1 excitation is omitted. In addition, a TSLIF excitation spectrum in which \mathcal{P}_2 was scanned across the $T'_1 \rightarrow T'_3$ absorption band confirmed that the two-step laser-induced fluorescence was due to triplet-triplet absorption. The lifetime of the two-step laser-induced fluorescence was found to be nearly identical to that of the prompt fluorescence, as is expected if the upper triplet lifetime is much shorter than the S'_1 lifetime. Using a comparative technique with 9,10-dibromoanthracene as the reference (see §3.3.2, **High-yield results**), the yield of reverse intersystem crossing was found to be 0.0024. This yield was associated with the $T'_2 \rightarrow S'_1$ transition since that represents a smaller energy gap than a transition from T'_3 . Similar work was also performed by the group of Tokumura on two other systems

²A tautomer is a structural isomer of a molecule formed by intramolecular transfer of a proton and rearrangement of the bonding electrons.

exhibiting excited-state intramolecular proton transfer, 2',3',4',5',6'-pentamethyl-3-hydroxyflavone [56] and 3-hydroxyflavone [58]. Two-step laser-induced fluorescence was observed to follow excitation of a higher-lying triplet state of the tautomer, but no yield for the reverse intersystem crossing process was reported for these systems.

Chou *et al.* have also used a two-step laser induced fluorescence comparative method with 9,10-dibromoanthracene as the reference to study reverse intersystem crossing in several coumarins [55]. The particular goal of their study was to investigate $T_{n\pi^*} \rightarrow S_{\pi\pi^*}$ reverse intersystem crossing which had previously been predicted to be more probable ($10^8 - 10^9 \text{ s}^{-1}$) compared to the $T_{\pi\pi^*} \rightarrow S_{\pi\pi^*}$ transition [61]. Reverse intersystem crossing yields of 8.4×10^{-4} for 7-hydroxy-4-methylcoumarin (7HMC) and 1.4×10^{-3} for 7-diethyl-amino-4-methylcoumarin (7DAMC) were measured, but no TSLIF fluorescence was measurable for the parent compound, coumarin (CM). The yields for 7HMC and 7DAMC were characterized as “high” and attributed to the small energy gap between the $T_{n\pi^*}$ and $S_{\pi\pi^*}$ states. In the case of coumarin, $T_{n\pi^*}$ is believed to be less energetic than $S_{\pi\pi^*}$, explaining the lack of TSLIF but also a correspondingly higher forward intersystem crossing yield.

3.3.2 High-yield results

Although the bulk of the reverse intersystem crossing yields reported in the literature have been quite small, there have been a few notable exceptions. The best known of these exceptions was reported in the 1989 work of McGimpsey and Scaiano [53]. Using two-step laser-induced fluorescence and transient absorption techniques, McGimpsey and Scaiano determined that the reverse intersystem crossing yield of 9,10-dibromoanthracene was 0.17 in cyclohexane and 0.09 in benzene for

the triplet state excited by 467-nm light. Two-step laser-induced fluorescence was also observed following excitation of a higher-lying triplet state by 700-nm light, but a yield was not determined for this process.

Halogenated derivatives of anthracene were also studied by Kobayashi *et al.* in 1978 [51] in a series of experiments which refined and extended their earlier work with several other anthracene derivatives [50], described above in §3.3.1. These refinements were motivated by the large uncertainty in the two-photon absorption cross section for anthracene, which was used in the earlier study to calculate the collection and detection efficiencies in their two-step excited fluorescence technique. In this series of experiments P-type delayed fluorescence was used as a reference rather than the two-photon excited fluorescence. Revised yields of 2.6×10^{-5} , 3.6×10^{-4} and 4.7×10^{-4} were reported for anthracene, 9-methylanthracene, and 9-phenylanthracene. In addition, reverse intersystem crossing yields of 0.015 and 0.27 were reported for 9,10-dichloroanthracene and 9,10-dibromoanthracene, respectively, in ethanol.

In 1996 Reindl and Penzkofer reported near-unity reverse intersystem crossing yields for the well-known dyes erythrosin B, tetraphenylporphyrin (TPP), and rose bengal [59]. Yields of 0.62 ± 0.05 and 0.9 ± 0.1 were calculated for the triplet states of erythrosin B and TPP excited by 527-nm light. A more detailed description of their experimental technique appears below in the review of the rose bengal literature.

Including the phrase “remarkably efficient” in the title of their 1997 report, Redmond *et al.* clearly emphasized the unusual nature of their observations of substantial reverse intersystem crossing in several cyanine dyes [60]. Merocyanine 540 (MC540) and two derivatives (BO-Se and QI-Se) were studied using a two-step laser-induced bleaching method, in which the number of photons absorbed

by the triplet state was determined using tetraphenylporphyrin as an actinometric reference. Using 532- + 640-nm excitation, Redmond *et al.* determined reverse intersystem crossing yields of 0.77, 0.75, and 0.68 for MC540, BO-Se, and QI-Se, respectively. The fluorescence produced following reverse intersystem crossing was also observed and found to be spectrally identical to the prompt fluorescence. The large yields of reverse intersystem crossing were attributed to the large T_n - T_1 energy gap and to the presence of heavy atoms (sulfur in MC540 and selenium in BO-Se and QI-Se).

It is interesting to note that TPP, the actinometric reference used by Redmond *et al.*, is also the molecule with the largest yield of reverse intersystem crossing to be identified by Reindl and Penzkofer. This raises the question of whether the triplet concentration of TPP can be assumed to have a linear dependence on absorbed photons, especially at high fluences. Because of the relative scarcity of molecules known to have a substantial reverse intersystem crossing it would appear prudent to verify the Redmond *et al.* results using an alternative method.

3.3.3 Previous rose bengal results

Several reports of reverse intersystem crossing in rose bengal (RB) have been published [54, 59, 62]. Durán and Cilento described observations of fluorescence following generation of RB triplets by energy transfer from excited triplet acetone [62]. It was believed that higher-lying triplets of RB were populated through triplet-triplet excitation transfer and subsequently relaxed to S_1 through reverse intersystem crossing. The magnitude of the emission was compared for a series of xanthene dyes (fluorescein and its halogenated derivatives eosin and rose bengal). This study revealed that heavy-atom substitution enhanced the effect, providing

evidence for reverse intersystem crossing as a key process leading to the emission. Durán and Cilento did not associate this process with a particular triplet state and did not quantitate the yield of reverse intersystem crossing. This may be due to the fact that this study represents one of the few in which chemical rather than optical excitation was used to produce the higher-lying triplet states.

Ketsle *et al.* investigated transient absorption changes following two-pulse excitation (532 nm + 694 nm) of various fluorescein derivatives, including rose bengal, incorporated in polymer hosts [54]. Photobleaching of the T_1 absorption due to the second pulse was observed to have a component that was irreversible on the microsecond time scale. Complementary measurements of the ground state absorption were also made, and it was found that the decrease in concentration of T_1 equaled the increase in concentration of S_0 , providing evidence for a photophysical rather than photochemical process. Fluorescence emission was also observed coincident with the second pulse. On the basis of their two-step laser-induced bleaching measurements Ketsle *et al.* reported a reverse intersystem crossing quantum yield of 0.72 for the triplet state excited by red light, to be denoted as T_3 in the present work. An examination of their analysis reveals that Ketsle *et al.* calculated this yield using the formula

$$\frac{\Delta A}{A_t} = \Phi_{\text{risc},T_3} \quad (3.7)$$

where A_t is the prompt decrease in absorption due to \mathcal{P}_2 as shown in Fig. 3.1. As discussed in §3.2.1 it is more appropriate to interpret bleaching as resulting from the fraction that undergoes reverse intersystem crossing and in addition does not repopulate the triplet manifold through $S_1 \rightarrow T_1$ transfer. This latter interpretation of the bleaching fraction, also shared by Redmond *et al.* [60], gives

$$\frac{\Delta A}{A_t} = \Phi_{\text{risc},T_3} (1 - \Phi_{\text{isc}}) , \quad (3.8)$$

which is analogous to Eq. (3.3). Recalculating a yield using Eq. (3.8) and the Ketsle *et al.* bleaching fraction data found in Table I of Ref. [54] gives $\Phi_{\text{risc},T_3} \gg 1$. Since the reverse intersystem crossing yield cannot exceed unity, it appears that their experimental data was obtained under conditions in which the assumptions used to derive these equations do not apply. In particular, these equations are valid only when the A_t measured is equal to $\sigma_{T_1,T_n} F_2 A_0$. The conditions under which this assumption are satisfied were mentioned previously (§3.2.3), but briefly, they are that the length of the exciting pulse is shorter than the lifetime of the upper-triplet state and that the transient absorption detection system is capable of responding on this same time scale. Ketsle *et al.* do not report the length of their second pump pulse, but only state that it is from a ruby laser. It appears likely that their excitation pulse is longer than several nanoseconds, which is much greater than the expected upper-triplet lifetime of picoseconds or less. In addition, the time response of their transient absorption detection system is not reported. The use of long pulses or slow detection systems with this approach to two-step laser-induced bleaching will underestimate the number of absorbed photons, thus leading to values of Φ_{risc,T_3} that exceed unity.

Reindl and Penzkofer reported an 80% quantum yield of reverse intersystem crossing for T_4 , the state excited through absorption of green light (527 nm) by T_1 [59]. Their measurements were of rose bengal in methanol. Using a model of the population dynamics, the yield was extracted from measurements of the pulse-to-pulse variation in fluorescence for a train of 6-ps long pulses with a separation of 10 ns.

Recent work by Lambert *et al.* compared fluorescence following 532- + 532-nm excitation with that following 532- + 640-nm excitation [63]. The absolute values of the reverse intersystem crossing yields for these two processes were not

determined, but the relative amount of two-step laser-induced fluorescence was quantified. When the second pulse was at 532-nm there was 13 times more fluorescence than for the case of 640-nm excitation. This result should be treated with some care as it does not simply translate to a factor of 13 difference in reverse intersystem crossing yields. The number of photons absorbed in these two cases was not calculated so it is not possible to come to any clear conclusions. In both cases the fluences were such that the system could not be treated as being in the regime of linear response.

3.4 One-color experiment

The simple analytical theories described earlier (§3.2.1 and §3.2.2) were based on the assumption that the light absorbed by T_1 is not absorbed by the ground state. The case in which one color of light is absorbed by both states is also of interest. This was the case studied in the work of Reindl and Penzkofer described above [59]. The one-color case is particularly interesting since it is possible to excite both transitions during a single pulse if the pulse length is greater than the S_1 lifetime. Reindl and Penzkofer used a multiple pulse technique in their studies. In this section an alternative single-pulse technique will be described and used to determine the reverse intersystem crossing yield for the T_4 state of rose bengal in water.

3.4.1 Experimental methods

The single-pulse fluorescence measurements probing T_4 were made with the optical layout shown in Fig. 3.3. The laser system was previously described in §2.1.1. A half-wave plate in a computer-controlled rotary mount (WP) and polarizing beam

Table 3.1: Summary of reverse intersystem crossing yields appearing in the literature.

Molecule	Φ_{risc}	Ref.
anthracene	4.5×10^{-6} , 2.6×10^{-5}	[50, 51]
2,2'-bipyridine-3,3'-diol	0.0024	[57]
BO-Se	0.75	[60]
9,10-dibromoanthracene	0.09 (benzene)	[53]
	0.17 (cyclohexane)	[53]
	0.27 (ethanol)	[51]
9,10-dichloroanthracene	0.015	[51]
7-diethyl-amino-4-methylcoumarin	1.4×10^{-3}	[55]
erythrosin B	0.62	[59]
7-hydroxy-4-methylcoumarin	8.4×10^{-4}	[55]
Merocyanine 540	0.77	[60]
9-methyl-anthracene	6.1×10^{-5} , 3.6×10^{-4}	[50, 51]
naphthalene-d ₈	5×10^{-7}	[49]
naphthalene-h ₈	2×10^{-7}	[49]
9-phenyl-anthracene	8×10^{-5} , 4.7×10^{-4}	[50, 51]
QI-Se	0.68	[60]
rose bengal	0.8 (527 nm)	[59]
	0.72 (694 nm)	[54]
tetraphenylporphyrin	0.9	[59]

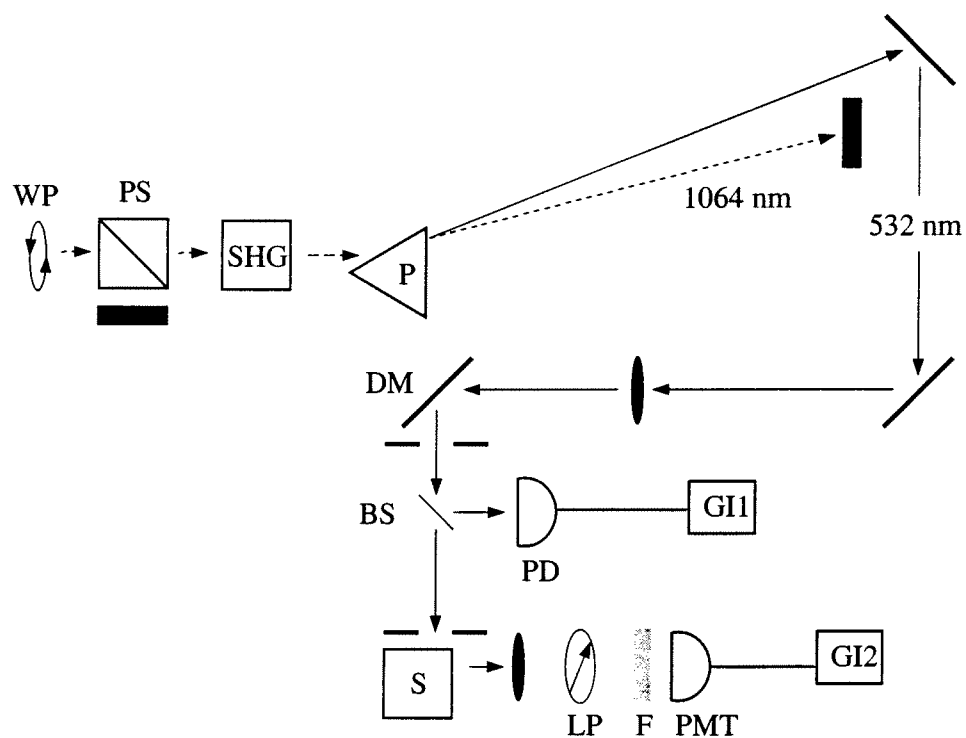


Figure 3.3: Experimental setup for one-color laser-induced fluorescence measurements. See Table 3.2 for symbol definitions.

Table 3.2: Equipment used in the one-color laser-induced fluorescence experiments

	Description	Details
BS	beam splitter	microscope slide ($\sim 4\%$ reflection)
DM	dichroic mirror	R@532 nm, T@1064 nm
F	interference filter long-pass filter	$\lambda_0 = 580$ nm, $\Delta\lambda = 10$ nm Schott, OG570
GI1-2	gated integrator	Stanford Research Systems, 250
LP	linear polarizer	at "magic angle" (54.7°)
P	prism	
PD	photodiode	EG&G, FND-100
PMT	photomultiplier tube	Burle, 6199
PS	polarizing beam splitter	$\lambda=1064$ nm
S	sample cuvette and beam mask	
SHG	second harmonic generator	KDP crystal
WP	half-wave plate	$\lambda=1064$ nm

splitter (PS) are used to control the energy of the pulse which generates the second harmonic ($\lambda = 532$ nm) in passing through a KDP crystal. The second harmonic and the fundamental ($\lambda = 1064$ nm) are separated using a prism (P), and the fundamental is dumped into a beam stop. The second harmonic pump pulse, \mathcal{P}_1 , is directed towards the sample cuvette (S) by a dichroic mirror (DM). This pulse overfills by approximately a factor of two a 2-mm diameter pinhole immediately prior to the sample cuvette. The fluorescence is collected perpendicular to the excitation pulse. This fluorescence passes through a linear polarizer (LP) oriented at approximately 54.7° relative to the linearly polarized pump pulse. This is the so-called “magic angle” that eliminates fluorescence anisotropy effects [64]. A long-pass filter and an interference filter centered at 580-nm are used to eliminate any scattered pump light. The fluorescence is then detected by a PMT and the signal digitized using a gated integrator (GI2). The energy of each pump pulse is monitored by reflecting a small fraction with a glass plate to a photodiode (PD) prior to the sample. The resulting signal is digitized using a gated integrator (GI1). This monitor signal is calibrated by placing an energy probe at the sample location.

3.4.2 Analytical methods

The green pump pulse used in this experiment had a pulse length approximately twice as long as the S_1 lifetime (~ 200 ps versus ~ 90 ps). At high fluences the ground state can be substantially depleted by the first half of the pulse, allowing the second half of the pulse to excite the resulting T_1 states to a higher-lying state, T_4 . Reverse intersystem crossing from T_4 will allow the fluorescence signal to continue to grow even though the ground state has been depleted. This process should modify the fluence-dependence of the fluorescence signal.

The orientational-average of the kinetic model used in the analysis is shown in Fig. 3.4. The rate equations describing the full orientation-dependent model are

$$\begin{aligned}
\frac{dp_{S_o}(\theta, t)}{dt} &= -3 \cos^2 \theta \sigma_{S_o S_1} (p_{S_o} - p_{S'_1}) I_1(t) + (1 - \Phi_{isc}) \tau_{S_1}^{-1} p_{S_1} + \tau_{T_1}^{-1} p_{T_1} \\
&\quad - k_{rot}(p_{S_o} - \langle p_{S_o} \rangle) \\
\frac{dp_{T_1}(\theta, t)}{dt} &= \Phi_{isc} \tau_{S_1}^{-1} p_{S_1} - \tau_{T_1}^{-1} p_{T_1} - 3 \cos^2 \theta \sigma_{T_1 T_4} (p_{T_1} - p_{T_4}) I_1(t) \\
&\quad + (1 - \Phi_{risc, T_4}) \tau_{T_4}^{-1} p_{T_4} - k_{rot}(p_{T_1} - \langle p_{T_1} \rangle) \\
\frac{dp_{S_1}(\theta, t)}{dt} &= k_r p_{S'_1} - \tau_{S_1}^{-1} p_{S_1} - k_{rot}(p_{S_1} - \langle p_{S_1} \rangle) \\
\frac{dp_{S'_1}(\theta, t)}{dt} &= 3 \cos^2 \theta \sigma_{S_o S_1} (p_{S_o} - p_{S'_1}) I_1(t) - k_r p_{S'_1} + \tau_{S_m}^{-1} p_{S_m} \\
&\quad - k_{rot}(p_{S'_1} - \langle p_{S'_1} \rangle) \\
\frac{dp_{S_m}(\theta, t)}{dt} &= + \Phi_{risc, T_4} \tau_{T_4}^{-1} p_{T_4} - \tau_{S_m}^{-1} p_{S_m} - k_{rot}(p_{S_m} - \langle p_{S_m} \rangle) \\
\frac{dp_{T_4}(\theta, t)}{dt} &= 3 \cos^2 \theta \sigma_{T_1 T_4} (p_{T_1} - p_{T_4}) I_1(t) - \tau_{T_4}^{-1} p_{T_4} - k_{rot}(p_{T_4} - \langle p_{T_4} \rangle),
\end{aligned} \tag{3.9}$$

where the $p_i(\theta, t)$ are the orientational subpopulations of S_o , T_1 , S_1 , S'_1 , S_m , and T_4 (arranged in order of increasing energy). The orientationally averaged population $\langle p_i(t) \rangle$ is given by Eq. (A.10). Table 3.3 lists the definitions and values of the photophysical parameters. The thermalization rate, k_r , has been assumed to be similar to that found in the closely related dye erythrosin [67, 68]. The unknown parameters are Φ_{risc, T_4} , τ_{T_4} , and τ_{S_m} . The pump pulse \mathcal{P}_1 has a Gaussian temporal

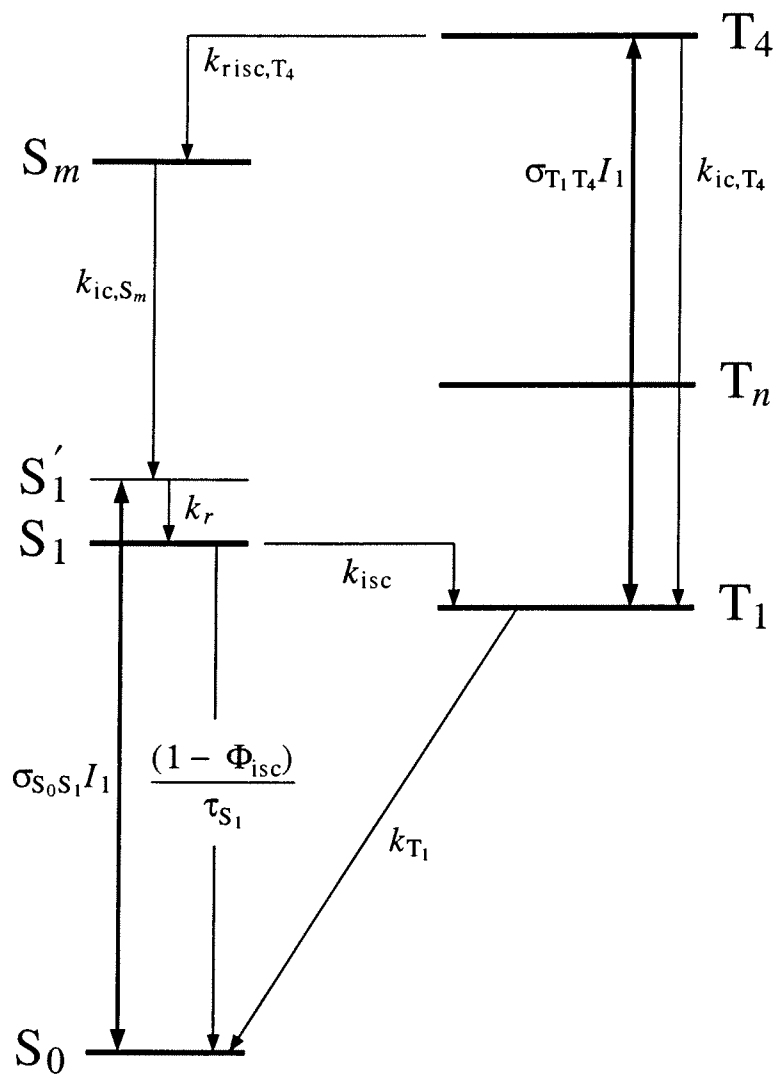


Figure 3.4: Energy-level scheme for 532-nm excitation dynamics. This diagram corresponds to an orientational-average of the kinetics described by Eq. (3.9). See Table 3.3 for parameter descriptions and values.

Table 3.3: Photophysical parameters of rose bengal in water that are relevant to 532-nm excitation. Parameters to be determined in the fitting process are indicated by t. b. d.

Symbol	Description	Value	Ref.
$\sigma_{S_0S_1}$	Ground-state absorption cross section at 532 nm ($S_0 + \hbar\omega \rightarrow S'_1$)	$1.8 \times 10^{-16} \text{ cm}^2$	[14]
$\sigma_{T_1T_4}$	Triplet absorption cross section at 532 nm ($T_1 + \hbar\omega \rightarrow T_4$)	$7.4 \times 10^{-17} \text{ cm}^2$	[14, 65]
τ_{S_1}	Lifetime of S_1	89 ps	[14–16]
τ_{S_m}	Lifetime of S_m	t. b. d.	—
τ_{T_1}	Lifetime of T_1 (includes both phosphorescence and oxygen quenching)	3 μs	[66]
Φ_{isc}	Intersystem crossing yield ($S_1 \rightarrow T_1$)	0.98	[16, 66]
Φ_{risc, T_4}	Reverse intersystem crossing yield ($T_4 \rightarrow S_m$)	t. b. d.	—
I_1	First pump-pulse photon intensity	variable	—
k_{ic, S_m}	Internal conversion rate ($S_m \rightarrow S'_1$)	$1/\tau_{S_m}$	—
k_{ic, T_4}	Internal conversion rate ($T_4 \rightarrow T_1$)	$(1 - \Phi_{risc, T_4})/\tau_{T_4}$	—
k_{isc}	Intersystem crossing rate ($S_1 \rightarrow T_1$)	Φ_{isc}/τ_{S_1}	—
k_r	Thermalization rate ($S'_1 \rightarrow S_1$)	$3 \times 10^{10} \text{ s}^{-1}$	[67, 68]
k_{risc, T_4}	Reverse intersystem crossing rate ($T_4 \rightarrow S_m$)	$\Phi_{risc, T_4}/\tau_{T_4}$	—
k_{rot}	Rotational diffusion rate	3.2 ns $^{-1}$	[69]
k_{T_1}	Relaxation rate of T_1	$1/\tau_{T_1}$	—

profile

$$I_1(t) = \frac{F_1}{\sqrt{2\pi\delta_1^2}} \exp(-t^2/(2\delta_1^2)) \quad (3.10)$$

where F_1 is the fluence (in units of photons/cm²) and δ_1 is related to the full width at half-maximum pulse length by $\text{FWHM} = \delta_1\sqrt{8\ln 2}$.

Excited state absorption from states other than T_1 has been neglected. Previous experiments have found no evidence for absorption of 532-nm light by S_1 [14]. The state T_4 may absorb 532-nm light and thus populate an even higher-lying state, but we assume that any such extremely high-lying state will relax back to T_4 essentially immediately. The validity of this assumption will be discussed in §3.4.3.

Computational techniques

The fluorescence f_1 due to \mathcal{P}_1 is proportional to the population of S_1 such that

$$f_1 = \frac{\Phi_f}{\tau_{S_1}} \left\langle \int_{-\infty}^{+\infty} p_{S_1}(t) dt \right\rangle \quad (3.11)$$

where Φ_f is the fluorescence quantum yield. The unknown photophysical parameters Φ_{risc,T_4} , τ_{T_4} , and τ_{S_m} are determined by fitting this model of the laser-induced fluorescence process to the fluence-dependent f_1 obtained experimentally. A numerical approach is required since analytical solutions cannot be obtained under the high-fluence conditions required to produce significant T_4 population. The numerical analysis consists of three major components: (a) a calculation of the fluence-dependent f_1 for a given trial set of photophysical parameters, (b) an algorithm that optimizes these parameters to provide the best fit to the experimental data, and (c) an estimate of the precision to which the extracted parameters are known based on a randomization and re-optimization technique.

Calculation of the fluence-dependent, one-color laser-induced fluorescence was based on the solution of the rate equations given in Eq. (3.9). These rate equations were solved using `stifbs`, an implementation of the algorithm of Bader and Deuffhard for solving a stiff set of ordinary differential equations [70,71]. A set of differential equations is “stiff” if the problem is characterized by two or more very different rates of change. In the case of the present model, T_1 relaxation takes place on the microsecond time scale whereas thermal relaxation of S_1 occurs a million times faster. More familiar algorithms such as the Runge-Kutta technique can often solve such sets of equations, but typically with less efficiency. Since the process of optimization requires the repeated solution of this set of equations it is prudent to select an efficient algorithm.

In order to compare the f_1 obtained from this model with the experimental data, it was necessary to scale the results to account for the unknown collection and detection efficiency. This was accomplished by selecting a multiplicative scaling factor, α , using standard linear least-squares fitting techniques such that the reduced χ_r^2 statistic,

$$\chi_r^2 = \frac{1}{N} \sum_{F_1} \left(\frac{f_{1,\text{expt}}(F_1) - \alpha f_{1,\text{model}}(F_1; \Phi_{\text{risc},T_4}, \tau_{T_4}, \tau_{S_m})}{\sigma_{1,\text{expt}}(F_1)} \right)^2, \quad (3.12)$$

was minimized. The standard deviations of the experimental measurements are given by $\sigma_{1,\text{expt}}$ and N is equal to the number of data points minus the number of free parameters (four, including α). The next step is to search parameter space in order to find the values of Φ_{risc,T_4} , τ_{T_4} , and τ_{S_m} that minimize χ_r^2 .

Since an analytical expression for the derivatives of $\chi_r^2(\Phi_{\text{risc},T_4}, \tau_{T_4}, \tau_{S_m})$ with respect to the free parameters is not available, it is necessary to select an optimization algorithm that only requires evaluation of χ_r^2 . The optimization algorithm used in this work was based on the downhill simplex method `amoeba`, though there are several others which would also be applicable [71]. These methods typically

require an initial guess for the set of free parameters and then look for a path downhill (relative to χ_r^2) through parameter space with the goal of finding a minimum. In the downhill simplex method defining the initial simplex requires $\mathcal{N} + 1$ guesses of starting parameter sets, where \mathcal{N} is the number of free parameters. In this case \mathcal{N} does not include α since that parameter is optimized separately. The method proceeds to a minimum by identifying the worst point in the simplex and then looking for a reflection or contraction in \mathcal{N} -space that will replace that point with one having a smaller χ_r^2 . Initially the simplex will move primarily through volume-conserving reflections, but as a minimum is approached contractions will reduce that volume. The algorithm is terminated when it has not improved on the best point for several iterations and the worst point is sufficiently close to the best point. The downhill simplex method will converge on at least a local minimum, but in order to increase confidence that the minimum is global, the optimization routine was repeated one or more times starting with a different initial simplex.

The downhill simplex method will report the set of parameters that provides the best fit, but it does not report the precision with which those parameters are known given the uncertainties in the experimental measurements. In this work an empirical approach was adopted, in which the precision was estimated by running the optimization routine on sets of fluence-dependent fluorescence curves, $f_{1,\text{mix}}$, calculated from

$$f_{1,\text{mix}}(F_1) = f_{1,\text{expt}}(F_1) + r\sigma_{1,\text{expt}}(F_1) , \quad (3.13)$$

where r is a uniformly distributed random number between -1 and 1. The standard deviations of the parameters found in minimizing ten such data sets provide the estimated precision to which the fit parameters are known.

3.4.3 Results

The fluence-dependent laser-induced fluorescence results for rose bengal excited by 532-nm light are shown in Fig. 3.5. During this series of experiments the pulse length was approximately 200 ps FWHM. Each point on the plot represents the average of six data sets, with error bars indicating the corresponding standard deviations. These data sets were obtained with various concentrations of rose bengal (55 nM to 24.6 μ M). The fluorescence signals in each data set were scaled using a multiplicative factor defined such that the fluorescence signal was equal to 1 at a fluence of 0.5×10^{16} photons/cm². With this scaling it was found that all data sets were in excellent agreement.

The parameters Φ_{risc,T_4} , τ_{T_4} , and τ_{S_m} can be determined by analyzing the nonlinear dependence of the fluorescence on fluence using the multistate kinetic model described in Eq. (3.9). This analysis of the data shown in Fig. 3.5 gives $\Phi_{\text{risc},T_4} = 0.12 \pm 0.02$ with $\chi_r^2 = 0.30$. The length of the excitation pulse is such that population undergoing reverse intersystem crossing will not significantly repopulate T_1 until after the pulse has passed. As a result the one-step laser-induced fluorescence signal is not strongly dependent on τ_{T_4} or τ_{S_m} . The fitting algorithm consistently finds $\Phi_{\text{risc},T_4} = 0.12$ but values for τ_{T_4} and τ_{S_m} range from 0.2 to 45 ps depending on the initial seed. Upper state lifetimes in this range produced identical χ_r^2 to three significant figures. All curves shown in this section were generated using $\tau_{T_4} = 1.9$ ps and $\tau_{S_m} = 7.7$ ps. The fluence-dependent fluorescence for the case of no reverse intersystem crossing is also shown in Fig. 3.5.

The population dynamics calculated from this model for S_0 , S_1 , T_1 , and T_4 are shown in Fig. 3.6 for the case of $F_1 = 4 \times 10^{16}$ photons/cm² using the parameters given in Table 3.3 and the best fit values reported above. At this high fluence T_1 is substantially populated even before the peak of the pulse arrives at ~ 430 ps.

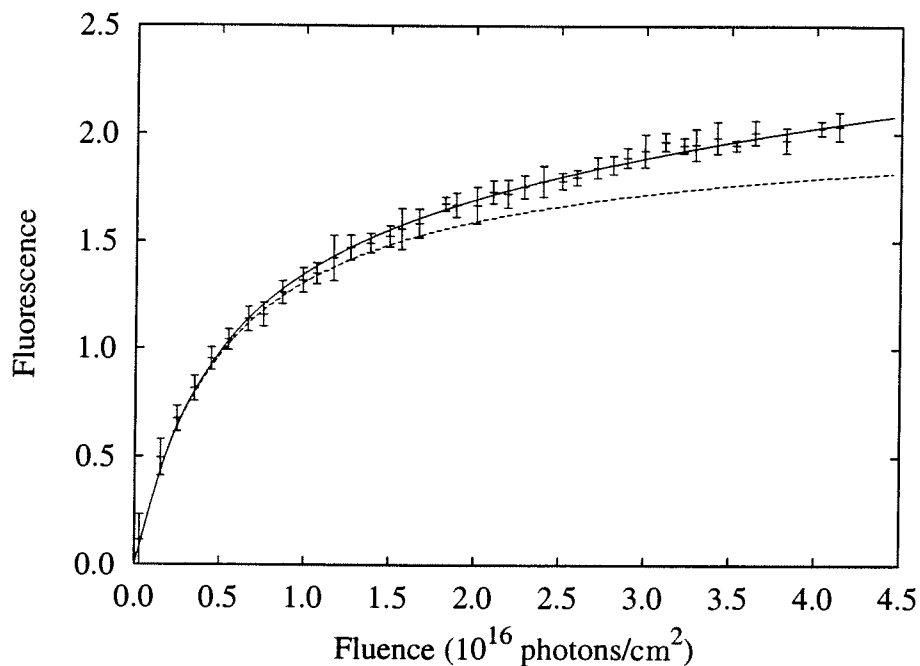


Figure 3.5: Experimental results of one-color laser-induced fluorescence measurements ($\lambda = 532$ nm). Best fit from model described by Eq. (3.9) (—); model without reverse intersystem crossing (- - -). The best fit is given by $\Phi_{\text{risc},T_4} = 0.12 \pm 0.02$ with $\chi_r^2 = 0.30$. This fit is insensitive to τ_{T_4} and τ_{S_m} . Error bars indicate the standard deviation calculated from six data sets, each resulting from a 64-shot average.

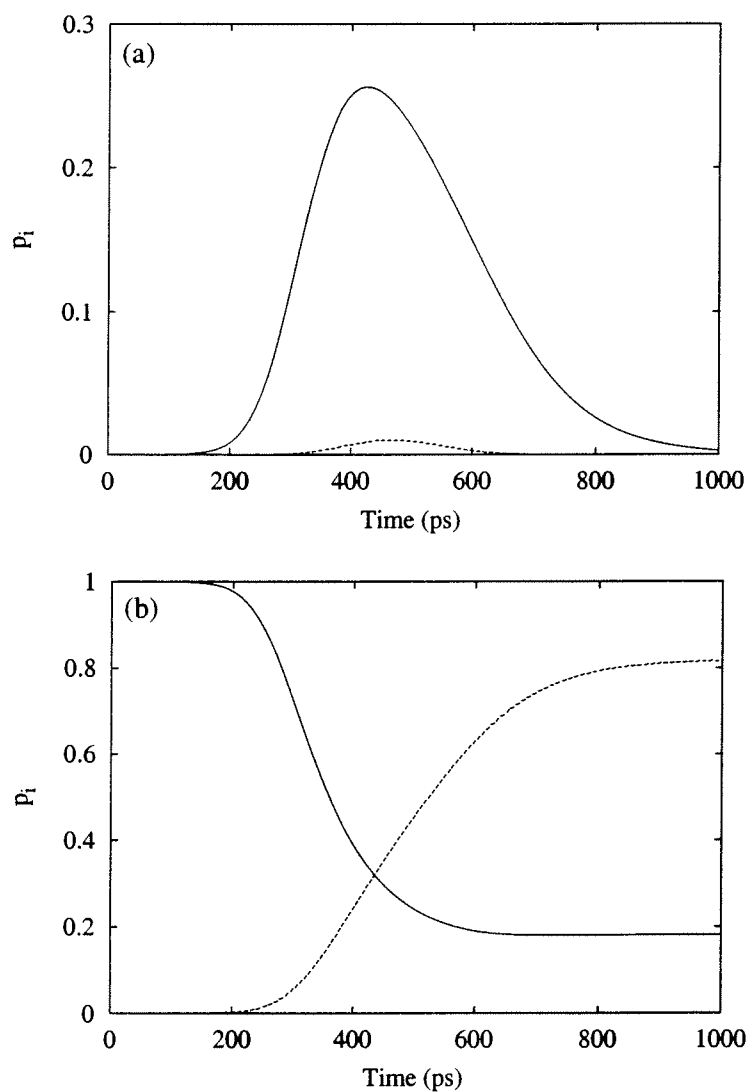


Figure 3.6: Population dynamics during one-color excitation. (a) S_1 (—); T_4 (- - -). (b) S_0 (—); T_1 (- - -). Calculations based on the model given in Eq. (3.9) using the parameters in Table 3.3 and the best fit values obtained from the data plotted in Fig. 3.5. The peak of the pulse occurs at ~ 430 ps and $F_1 = 4 \times 10^{16}$ photons/cm².

This allows for population of T_4 through triplet-triplet absorption by the later portions of the pulse.

Reverse intersystem crossing from T_4 leads to a repopulation of S_1 , as shown in Fig. 3.7. This figure compares the time-dependent S_1 population for a model with triplet-triplet absorption and reverse intersystem crossing with that obtained from a model in which these processes are not included. Because fluorescence is proportional to the S_1 population, this figure also shows that reverse intersystem contributes to an increased fluorescence signal at higher fluences.

The relevance of including rotational diffusion in the model of one-color laser-induced fluorescence is illustrated by Fig. 3.8. The fluorescence signal is limited by the depletion of the ground state, which is dependent on photoselection effects (see Appendix A). The solid curve and dashed curve were computed using the rotational diffusion rate found experimentally for rose bengal in water ($k_{rot} = 3.2 \times 10^9 \text{ s}^{-1}$, Ref. [69]) and a much faster rate ($k_{rot} = 10^{12} \text{ s}^{-1}$) that is essentially equivalent to ignoring rotational effects for the time scale of the pulses used in this study. For example, at $F_1 = 3 \times 10^{16} \text{ photons/cm}^2$ the fast rotation model results in a 17% greater fluorescence than the model incorporating the actual rotational rate. The S_1 thermalization rate also affects the fluence-dependence of the fluorescence. The crosses in Fig. 3.8 represent a curve in which both fast rotation and fast thermalization ($k_r = 10^{12} \text{ s}^{-1}$) have been included. If the experimental data shown in Fig. 3.5 are re-fit using the faster rotational diffusion rate and thermalization rate the values of the free parameters are shifted. In this case $\Phi_{\text{risc},T_4} = 0.18$, $\tau_{T_4} = 31 \text{ fs}$, and $\tau_{S_m} = 83 \text{ fs}$ with $\chi_r^2 = 0.70$.

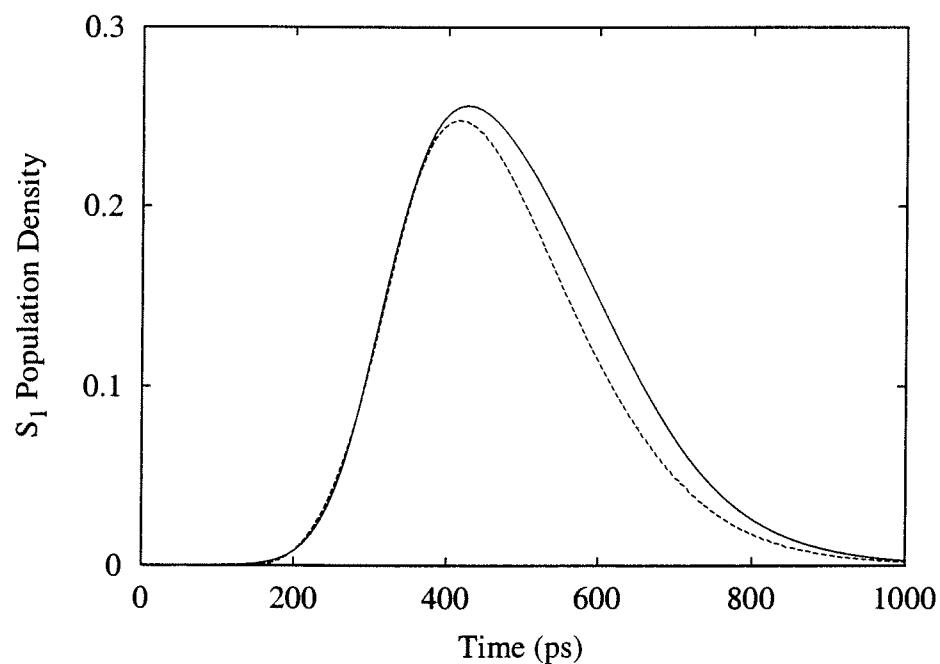


Figure 3.7: Effect of triplet-triplet absorption and reverse intersystem crossing on S_1 dynamics during one-color excitation. Model with $T_1 \rightarrow T_4$ absorption and reverse intersystem crossing (—); model with no excited state absorption (- - -). Calculations based on the model given in Eq. (3.9) using the parameters in Table 3.3 and the best fit values obtained from the data plotted in Fig. 3.5. The peak of the pulse occurs at ~ 430 ps and $F_1 = 4 \times 10^{16}$ photons/cm².

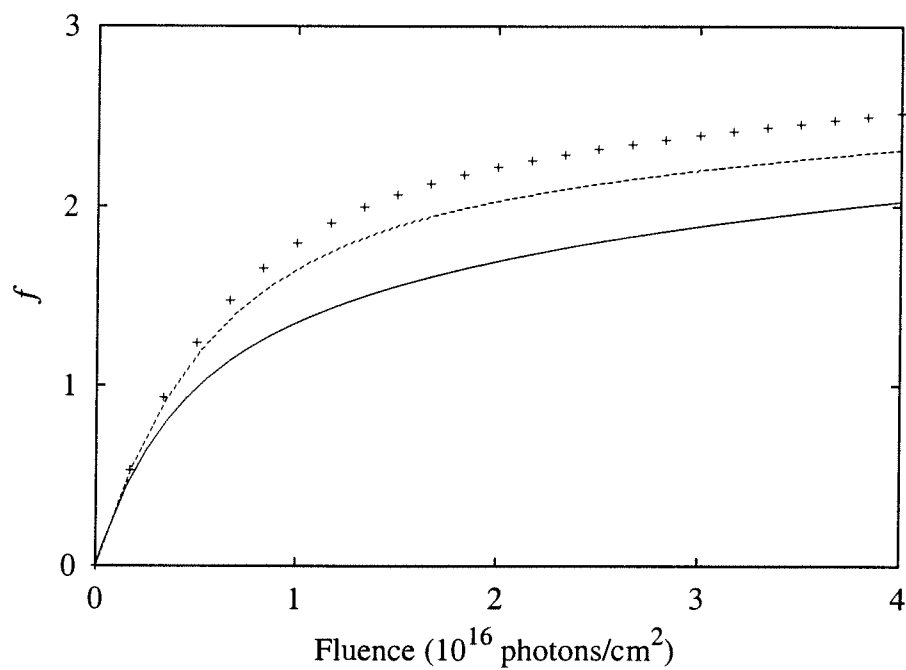


Figure 3.8: Effect of rotational diffusion and thermalization on one-color laser-induced fluorescence. $k_{rot} = 3.2 \times 10^9 \text{ s}^{-1}$ and $k_r = 3 \times 10^{10} \text{ s}^{-1}$ (—); $k_{rot} = 10^{12} \text{ s}^{-1}$ and $k_r = 3 \times 10^{10} \text{ s}^{-1}$ (- - -); $k_{rot} = k_r = 10^{12} \text{ s}^{-1}$ (+). Other parameters as given in Table 3.3 and from the best fit to the data plotted in Fig. 3.5.

3.5 Two-color experiments

3.5.1 Experimental methods

The two-step laser-induced fluorescence measurements probing T_2 were made with the optical layout shown in Fig. 3.9. Briefly, the final output of the laser system is a pulse with a length of ~ 190 ps, a wavelength of 1064 nm and an energy exceeding 2 mJ. In this experiment the second harmonic was generated from the laser fundamental using a KDP crystal (SHG), resulting in a pulse with a wavelength of 532 nm, a pulse length of ~ 130 ps, and energy greater than 250 μ J. To achieve a high degree of spectral separation between the fundamental and second harmonic pulses, a prism (P) is used to spatially disperse the two beams. The first pump pulse, \mathcal{P}_1 , has a wavelength of 532 nm, and the second pump pulse, \mathcal{P}_2 , has a wavelength of 1064 nm. \mathcal{P}_2 is delayed by 34 ns relative to \mathcal{P}_1 by traversal of a greater optical path length. The delay path includes a half-wave plate followed by a polarizing beam splitter, allowing for continuous variation of the second pump pulse energy. The pump pulses \mathcal{P}_1 and \mathcal{P}_2 are recombined spatially at a dichroic mirror (DM). The pulses pass through two pin holes, ensuring collimation, before irradiating a 2-mm diameter spot at the sample cuvette. A small fraction of the excitation light is reflected by a glass plate to a silicon photodiode. This signal is split before being sampled by two gated integrators (GI1 and GI2), which distinguish between the \mathcal{P}_1 and \mathcal{P}_2 signals. The pump-pulse signals are calibrated individually using an energy meter. Emission from the excited sample is collected, spectrally resolved using a monochromator (SP2), and detected by a photomultiplier tube. The signal from the PMT is split and sampled by an additional two gated integrators (GI3 and GI4). The temporal gate of GI3 is centered on the fluorescence excited by \mathcal{P}_1 . The center of the GI4 temporal gate is set to be 34 ns

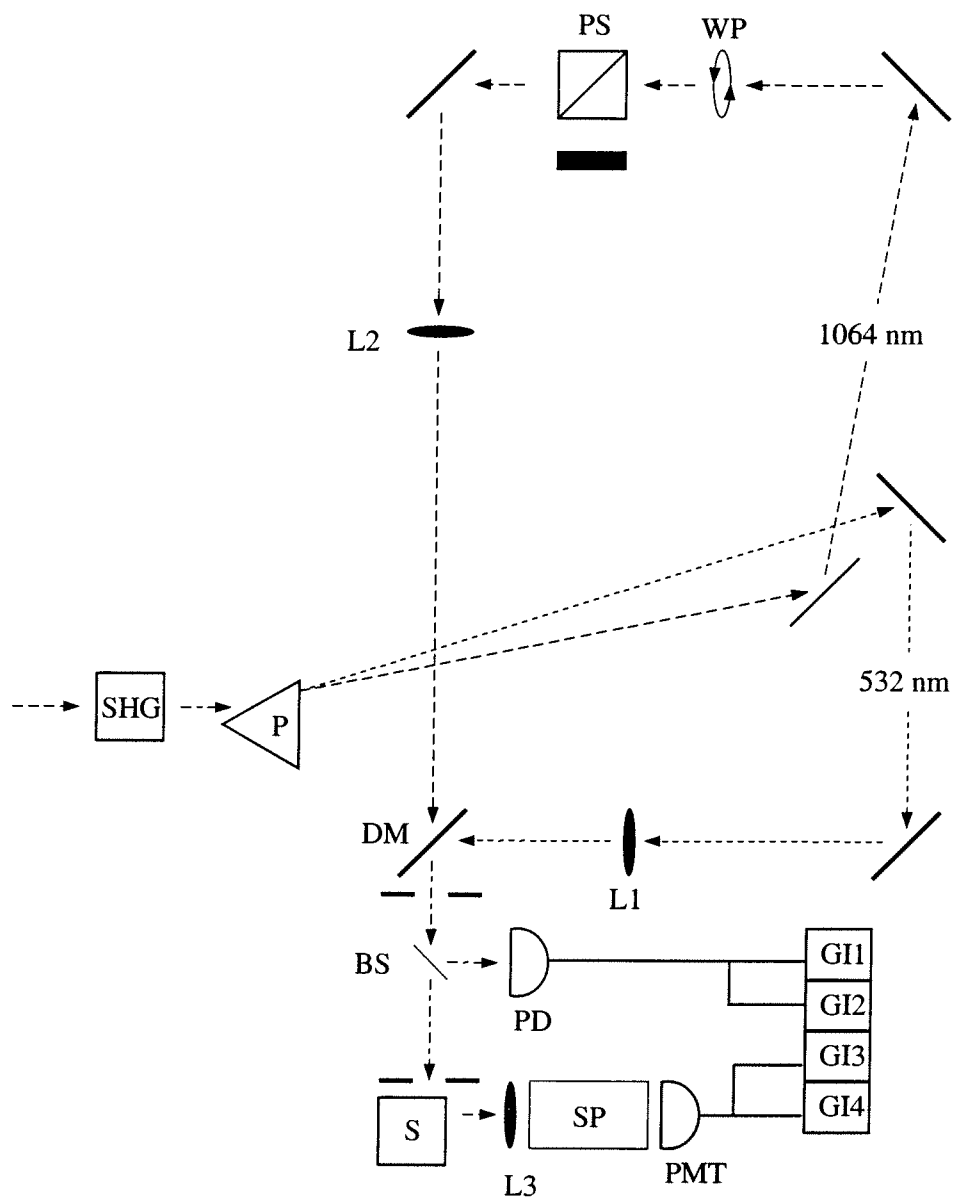


Figure 3.9: Experimental setup for two-step laser-induced fluorescence measurements ($\lambda_2 = 1064$ nm). See Table 3.4 for symbol definitions.

Table 3.4: Equipment used in the two-step laser-induced fluorescence experiments

	Description	Details
BS	beam splitter	microscope slide ($\sim 4\%$ reflection)
DM	dichroic mirror	R@532 nm, T@1064 nm
GI1-4	gated integrator	Stanford Research Systems, 250
L1-3	lenses	
P	prism	
PD	photodiode	EG&G, FND-100
PMT	photomultiplier tube	Burle, 6199
PS	polarizing beam splitter	$\lambda=1064$ nm
S	sample cuvette and beam mask	
SHG	second harmonic generator	KDP crystal
SP	monochromator, 4 nm BW	Photon Technology Intl., 102
WP	half-wave plate	$\lambda=1064$ nm

later than the center of the GI3 gate, corresponding to the time delay between the pump pulses. Both gates are 20 ns wide. The values of all four gated integrators are recorded by a computer for each shot.

Two-step laser-induced fluorescence measurements probing T_3 are made using a similar setup. In this case \mathcal{P}_2 , the 1064-nm pump pulse, is replaced by a 632-nm-wavelength pump pulse, while the first pulse remains at 532 nm. The 632-nm pulse is generated by stimulated Raman scattering of the Nd:YAG second harmonic in an 18-cm ethanol cell, resulting in 60 $\mu\text{J}/\text{pulse}$ with a pulse length of approximately 80 ps. The 632-nm light is separated from the 532-nm light by a pair of prisms before \mathcal{P}_2 enters the delay line. From this point the system is identical to the previously described two-step, laser-induced fluorescence system.

3.5.2 Analytical methods

The analytical model of two-step laser-induced fluorescence given by Eq. (3.6) is only applicable to low-intensity and low-fluence conditions. A more complex model that is less amenable to analytic solution can be used to determine several photophysical parameters associated with an upper triplet state from two-step laser-induced fluorescence (TSLIF) measurements collected over a range of second pump pulse (\mathcal{P}_2) fluences. These measurements are sensitive to the lifetime of the upper triplet state excited by \mathcal{P}_2 and the quantum yield of intersystem crossing from this state back to the singlet manifold. The upper triplet photophysical parameters can be determined by fitting a time-dependent model of the two-step laser-induced fluorescence process to the fluence-dependent TSLIF data.

Two-pulse kinetic model

The orientational-average of the kinetic model used to analyze the TSLIF experiments is shown in Fig. 3.10. The rate equations describing this model are

$$\begin{aligned}
\frac{dp_{S_o}(\theta, t)}{dt} &= -3 \cos^2 \theta \sigma_{S_o S_1} (p_{S_o} - p_{S_1'}) I_1(t) + (1 - \Phi_{isc}) \tau_{S_1}^{-1} p_{S_1} + \tau_{T_1}^{-1} p_{T_1} \\
&\quad - k_{rot} (p_{S_o} - \langle p_{S_o} \rangle) \\
\frac{dp_{T_1}(\theta, t)}{dt} &= \Phi_{isc} \tau_{S_1}^{-1} p_{S_1} - \tau_{T_1}^{-1} p_{T_1} - 3 \cos^2 \theta \sigma_{T_1 T_4} (p_{T_1} - p_{T_4}) I_1(t) \\
&\quad - 3 \cos^2 \theta \sigma_{T_1 T_n} (p_{T_1} - p_{T_n}) I_2(t) + (1 - \Phi_{risc, T_4}) \tau_{T_4}^{-1} p_{T_4} \\
&\quad + (1 - \Phi_{risc, T_n}) \tau_{T_n}^{-1} p_{T_n} - k_{rot} (p_{T_1} - \langle p_{T_1} \rangle) \\
\frac{dp_{S_1}(\theta, t)}{dt} &= k_r p_{S_1'} - \tau_{S_1}^{-1} p_{S_1} - k_{rot} (p_{S_1} - \langle p_{S_1} \rangle) \\
\frac{dp_{S_1'}(\theta, t)}{dt} &= 3 \cos^2 \theta \sigma_{S_o S_1} (p_{S_o} - p_{S_1'}) I_1(t) - k_r p_{S_1'} + \tau_{S_m}^{-1} p_{S_m} \\
&\quad + \Phi_{risc, T_n} \tau_{T_n}^{-1} p_{T_n} - k_{rot} (p_{S_1'} - \langle p_{S_1'} \rangle) \\
\frac{dp_{T_n}(\theta, t)}{dt} &= 3 \cos^2 \theta \sigma_{T_1 T_n} (p_{T_1} - p_{T_n}) I_2(t) - \tau_{T_n}^{-1} p_{T_n} - k_{rot} (p_{T_n} - \langle p_{T_n} \rangle) \\
\frac{dp_{S_m}(\theta, t)}{dt} &= + \Phi_{risc, T_4} \tau_{T_4}^{-1} p_{T_4} - \tau_{S_m}^{-1} p_{S_m} - k_{rot} (p_{S_m} - \langle p_{S_m} \rangle) \\
\frac{dp_{T_4}(\theta, t)}{dt} &= 3 \cos^2 \theta \sigma_{T_1 T_4} (p_{T_1} - p_{T_4}) I_1(t) - \tau_{T_4}^{-1} p_{T_4} - k_{rot} (p_{T_4} - \langle p_{T_4} \rangle)
\end{aligned} \tag{3.14}$$

where the p_i are the orientational subpopulations of S_o , T_1 , S_1 , S_1' , T_n , S_m , and T_4 (arranged in order of increasing energy), where $n = 2$ or 3 . Tables 3.3 and 3.5 list the definitions and values of the photophysical parameters. The unknown parameters are Φ_{risc, T_n} and τ_{T_n} . The pump pulses \mathcal{P}_1 and \mathcal{P}_2 have Gaussian

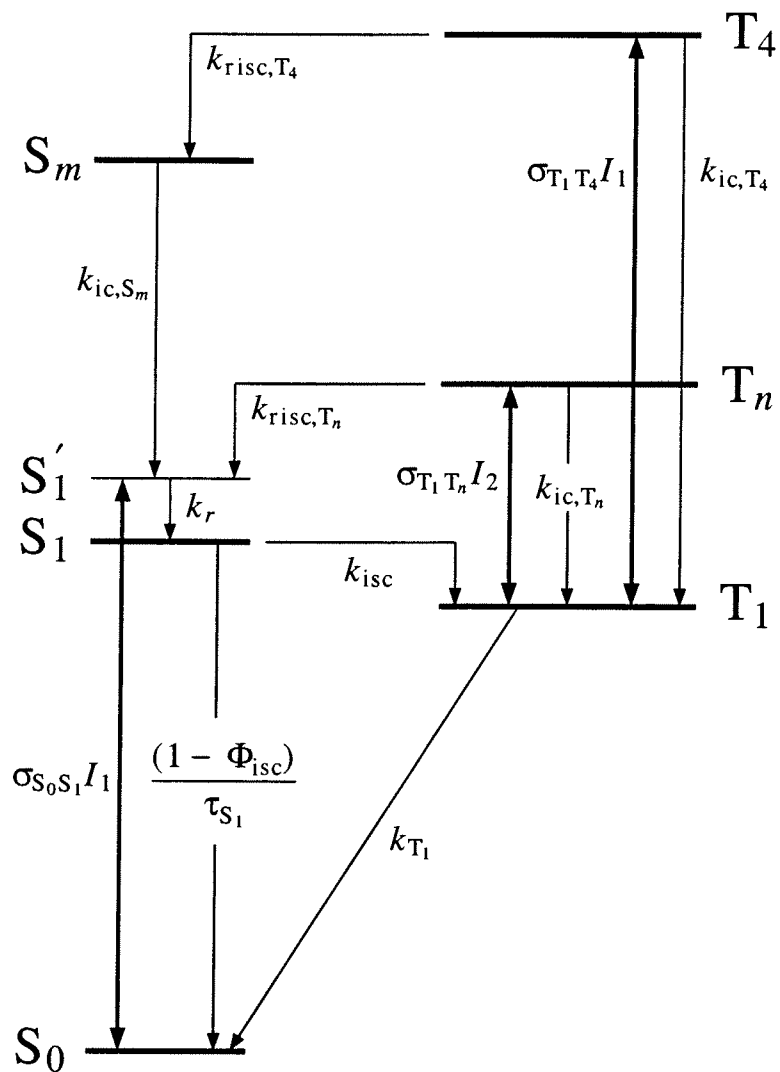


Figure 3.10: Energy-level scheme for description of two-color excitation dynamics. Complete two-step model corresponding to an orientational-average of Eq. (3.14). See Tables 3.3 and 3.5 for parameter descriptions and values.

Table 3.5: Photophysical parameters for two-color excitation of rose bengal

Symbol	Description	Value	Ref.
σ_{T_1, T_2}	Triplet absorption cross section at 1064 nm ($T_1 + \hbar\omega \rightarrow T_2$)	$1.1 \times 10^{-16} \text{ cm}^2$	Chap. 2
τ_{T_n}	Lifetime of T_n	t. b. d.	—
Φ_{risc, T_n}	Reverse intersystem crossing yield ($T_n \rightarrow S'_1$)	t. b. d.	—
F_1	First pump-pulse photon fluence	variable	—
F_2	Second pump-pulse photon fluence	variable	—
k_{ic, T_n}	Internal conversion rate ($T_n \rightarrow T_1$)	$(1 - \Phi_{\text{risc}, T_n}) / \tau_{T_n}$	—
k_{risc, T_n}	Reverse intersystem crossing rate ($T_n \rightarrow S'_1$)	$\Phi_{\text{risc}, T_n} / \tau_{T_n}$	—

temporal profiles such that

$$I_1(t) = \frac{F_1}{\sqrt{2\pi\delta_1^2}} \exp(-(t + \Delta/2)^2/(2\delta_1^2)) \quad (3.15)$$

and

$$I_2(t) = \frac{F_2}{\sqrt{2\pi\delta_2^2}} \exp(-(t - \Delta/2)^2/(2\delta_2^2)) , \quad (3.16)$$

where F_1 and F_2 are the fluences, δ_1 and δ_2 are related to the full width at half-maximum pulse lengths by $\text{FWHM} = \delta\sqrt{8\ln 2}$, and Δ is the time delay between the peaks of \mathcal{P}_1 and \mathcal{P}_2 .

As in the one-color laser-induced fluorescence experiment, excited state absorption from S_1 and T_4 has been neglected. In addition, absorption by T_n is also not included in this model. The validity of this assumption will be discussed in Sec. 3.5.3.

As a result of the large time delay between the pump pulses ($\Delta=34$ ns), it is possible to separate the system of rate equations (3.14) into two subsets. The set of equations describing the effects of the first pump pulse reduces to Eq. (3.9), the model used in the one-color laser-induced fluorescence experiments. These equations are used for $t = -\infty$ to $t = 0$. The time $t = 0$ is midway between the peaks of \mathcal{P}_1 and \mathcal{P}_2 , which are separated by a delay much greater than their pulse lengths and the lifetimes of all excited states except T_1 . The processes included in this first segment, where only the effects of \mathcal{P}_1 are relevant, are shown in Fig. 3.4.

This set of equations describing the effects of \mathcal{P}_1 neglects all terms containing I_2 . Since T_n is only populated by \mathcal{P}_2 , corresponding terms can be eliminated from Eq. (3.14). The process of reverse intersystem crossing is included in this model of the interaction of \mathcal{P}_1 with the sample. As shown earlier, the first pump pulse may be absorbed by both S_0 and by any T_1 population created by preceding parts of the same pulse. Absorption of \mathcal{P}_1 light by the T_1 state populates the T_4

state, which has a significant yield of reverse intersystem crossing. It is necessary to include this process for pulses longer than the $S_1 \rightarrow T_1$ intersystem crossing time, because it can lead to an apparent enhancement of the fluorescence yield, particularly at fluences resulting in depletion of the ground state. It is important to emphasize that the reverse intersystem crossing described above occurs from the triplet state populated by secondary absorption of the first pump pulse and is easily distinguished temporally from the process this experiment is designed to measure: reverse intersystem crossing from the triplet state populated by the second pulse.

The effects of \mathcal{P}_1 and \mathcal{P}_2 can be separated cleanly because the system has relaxed such that only S_0 and T_1 are populated at $t = 0$. The effects of only the second pump pulse are considered from this time to $t = +\infty$. The model of this second excitation step is shown in Fig. 3.11 after orientational-averaging. The equations describing this segment are

$$\begin{aligned}
\frac{dp_{S_0}(\theta, t)}{dt} &= (1 - \Phi_{\text{isc}})\tau_{S_1}^{-1}p_{S_1} + \tau_{T_1}^{-1}p_{T_1} - k_{\text{rot}}(p_{S_0} - \langle p_{S_0} \rangle) \\
\frac{dp_{T_1}(\theta, t)}{dt} &= \Phi_{\text{isc}}\tau_{S_1}^{-1}p_{S_1} - \tau_{T_1}^{-1}p_{T_1} - 3\cos^2\theta\sigma_{T_1, T_n}(p_{T_1} - p_{T_n})I_2(t) \\
&\quad + (1 - \Phi_{\text{risc}, T_n})\tau_{T_n}^{-1}p_{T_n} - k_{\text{rot}}(p_{T_1} - \langle p_{T_1} \rangle) \\
\frac{dp_{S_1}(\theta, t)}{dt} &= k_r p_{S'_1} - \tau_{S_1}^{-1}p_{S_1} - k_{\text{rot}}(p_{S_1} - \langle p_{S_1} \rangle) \\
\frac{dp_{S'_1}(\theta, t)}{dt} &= -k_r p_{S'_1} + \Phi_{\text{risc}, T_n}\tau_{T_n}^{-1}p_{T_n} - k_{\text{rot}}(p_{S'_1} - \langle p_{S'_1} \rangle) \\
\frac{dp_{T_n}(\theta, t)}{dt} &= 3\cos^2\theta\sigma_{T_1, T_n}(p_{T_1} - p_{T_n})I_2(t) - \tau_{T_n}^{-1}p_{T_n} - k_{\text{rot}}(p_{T_n} - \langle p_{T_n} \rangle).
\end{aligned} \tag{3.17}$$

In this segment all terms containing I_1 and p_{T_4} , the subpopulation of T_4 , are dropped from Eq. 3.14.

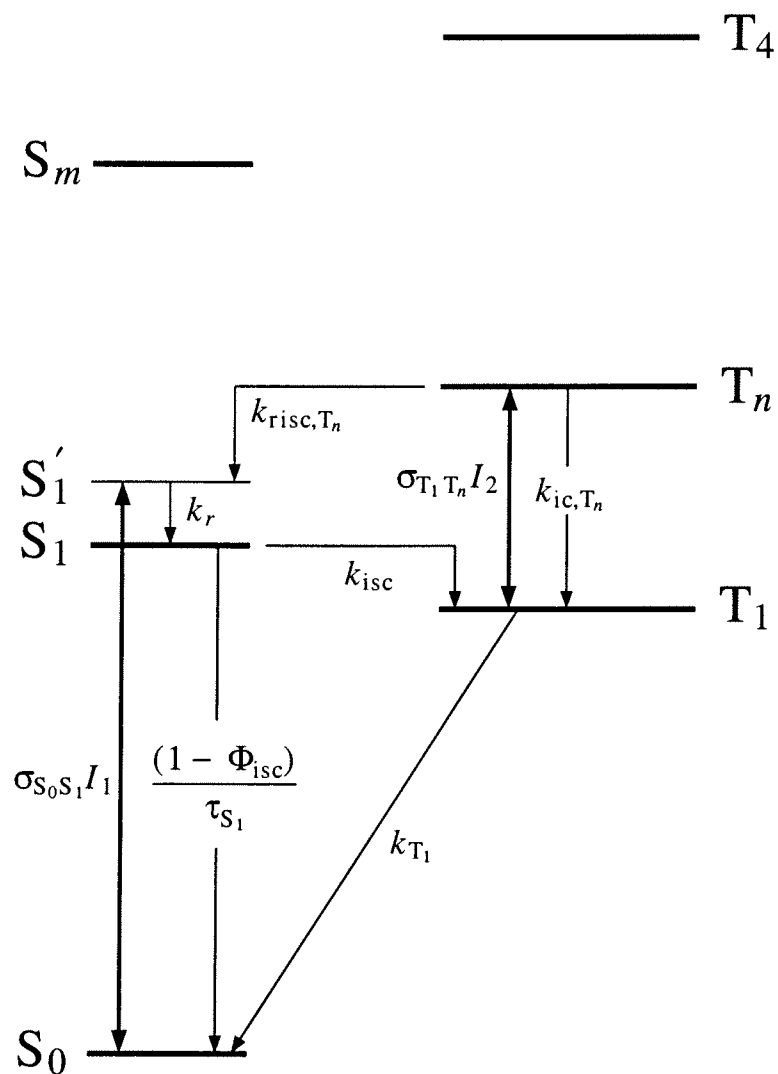


Figure 3.11: Energy-level scheme for two-color excitation dynamics. \mathcal{P}_2 subset of the model corresponding to Eq. (3.17) after orientational-averaging. See Tables 3.5 and 3.5 for parameter descriptions and values.

The fluorescence f due to the two pulses is proportional to the population of S_1 such that

$$f_1 = \frac{\Phi_f}{\tau_{S_1}} \left\langle \int_{-\infty}^0 p_{S_1}(t) dt \right\rangle \quad (3.18)$$

and

$$f_2 = \frac{\Phi_f}{\tau_{S_1}} \left\langle \int_0^{+\infty} p_{S_1}(t) dt \right\rangle \quad (3.19)$$

where Φ_f is the fluorescence yield. The two-step laser-induced fluorescence ratio f_R is defined by

$$f_R \equiv \frac{f_2}{f_1}. \quad (3.20)$$

This is a convenient quantity to compare with experimental results because fluorescence yield, collection, and detection efficiency factors are eliminated.

Thermal effects have not been included in this model because of the negligible increase in temperature with each pulse. The highest fluence of \mathcal{P}_2 is 9×10^{16} photons/cm², which corresponds to 0.017 J/cm² for 1064-nm light. Roughly 40% of this energy will be absorbed along the 1-cm path through the sample, giving an energy density of 7 mJ/cm³ in the excitation volume. If all of this energy is dissipated non-radiatively into the solvent the specific heat of water (4.18 J/g/° C) can be used to calculate that the transient temperature increase will be no more than 0.002° C. The sample is stirred throughout the experiment so no significant long-term temperature increase is expected.

Optimization technique

The T_n photophysical parameters Φ_{risc, T_n} and τ_{T_n} are determined by fitting this model of the two-step laser-induced fluorescence process to the fluence-dependent f_R obtained experimentally. As will be discussed in Sec. 3.5.3, extraction of both parameters requires f_R measurements over a range of F_2 fluences, which, at the upper limit, are sufficient to partially deplete the lowest triplet state. In addition,

the length of the second pump pulse must exceed the lifetime of T_n . A numerical approach similar to that used for the one-color laser-induced fluorescence analysis is adopted.

Calculation of the fluence-dependent, two-step laser-induced fluorescence ratio was based on the sequential solution of the rate equations given in Eq. 3.9 and 3.17. These rate equations were solved using `stifbs`, the algorithm for stiff sets of differential equations described previously. The agreement between the f_R obtained from this model and the experimental data can be quantified by the χ_r^2 statistic:

$$\chi_r^2 = \frac{1}{N} \sum_{\{F_1, F_2\}} \left(\frac{f_{R,\text{expt}}(F_1, F_2) - f_{R,\text{model}}(F_1, F_2; \tau_{T_n}, \Phi_{\text{risc}, T_n})}{\sigma_{R,\text{expt}}(F_1, F_2)} \right)^2, \quad (3.21)$$

which is summed over the set $\{F_1, F_2\}$ for which experimental measurements of the TSLIF ratio, $f_{R,\text{expt}}$ were made. The standard deviations of these measurements are given by $\sigma_{R,\text{expt}}$. In contrast with the one-color laser-induced fluorescence analysis, the use of the two-step laser-induced fluorescence ratio eliminates the need for the scaling factor α . As described previously, the next step is to search parameter space using the downhill simplex method in order to find the values of τ_{T_n} and Φ_{risc, T_n} that minimize χ_r^2 and then use the randomization and re-optimization technique to estimate the precision to which those parameters are known.

3.5.3 Results

The emission spectra for 532- + 1064-nm excitation of rose bengal are shown in Fig. 3.12. These spectra were obtained by scanning the monochromator while keeping the energies of \mathcal{P}_1 and \mathcal{P}_2 fixed. The nearly identical emission spectra confirms the $S_1 \rightarrow S_0$ origin of the emission following 1064-nm excitation. The increased spectral width of the \mathcal{P}_1 -induced emission may be attributed to power

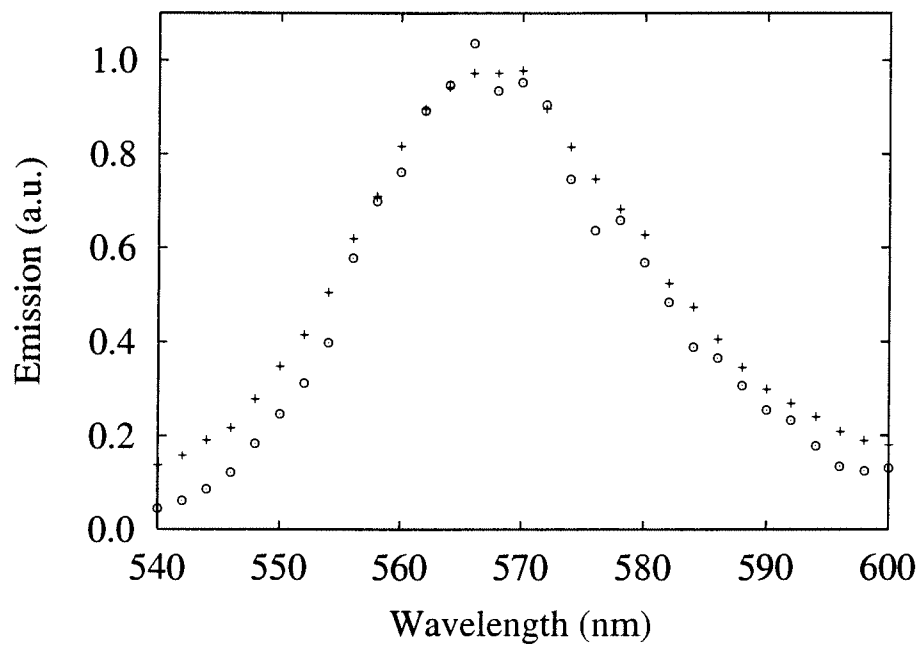


Figure 3.12: Emission spectra resulting from 532- + 1064-nm excitation. Emission following \mathcal{P}_1 (+); emission following \mathcal{P}_2 (o).

broadening [72]. Although \mathcal{P}_2 is more intense than \mathcal{P}_1 it does not lead to power broadening because \mathcal{P}_2 does not perturb S_0 and S_1 .

Fig. 3.13 shows the two-step laser-induced fluorescence ratio for 532- + 1064-nm excitation. The \mathcal{P}_1 fluence was held constant at 3.3 ± 0.2 mJ/cm², and the resulting fluorescence varied by less than 2%. No emission following \mathcal{P}_2 was detected when \mathcal{P}_1 was blocked. Each point in this plot represents the average of from 26 to 370 double-pulse excitations. The error bars indicate the corresponding standard deviations. The parameters Φ_{risc,T_2} and τ_{T_2} can be determined by analyzing the multistate kinetic model described by Eq. (3.14). Fitting this model to the data shown in Fig. 3.13 gives $\Phi_{\text{risc},T_2} = 0.0076 \pm 0.0002$ and $\tau_{T_2} = 1.56 \pm 0.01$ ps with $\chi_r^2 = 0.012$.

Although no analytical expression can be given for $f_R(F_1, F_2)$ that is applicable for the high fluences used in these experiments, it is possible to explain qualitatively the shape of the f_R versus F_2 curve shown in Fig. 3.13. This explanation also provides some justification for why the kinetic model analysis is sensitive to the lifetime of the upper triplet state. Under low-fluence and low-intensity conditions, Eq. (3.6) predicts that f_R will increase linearly with F_2 . Deviations from the predicted linear response are expected to occur only for \mathcal{P}_2 with sufficiently high fluence. When the pulse length is shorter than the lifetime of T_2 , the saturation fluence $F_{\text{sat}} = (\sigma_{T_1, T_2})^{-1}$ for $T_1 \rightarrow T_2$ excitation is 9×10^{15} photons/cm² (1.7 mJ/cm²). Multiple excitations are possible for pulses that are longer than the lifetime of T_2 . This allows the two-step laser-induced fluorescence ratio to continue to grow beyond the short-pulse saturation fluence limit. The maximum number of excitation cycles that can be achieved during a pulse is limited by the upper-triplet lifetime, τ_{T_2} , and the length of the second pump pulse, δ_2 . Since the nonlinear portion of the f_R curve is dependent on the upper-triplet lifetime it is

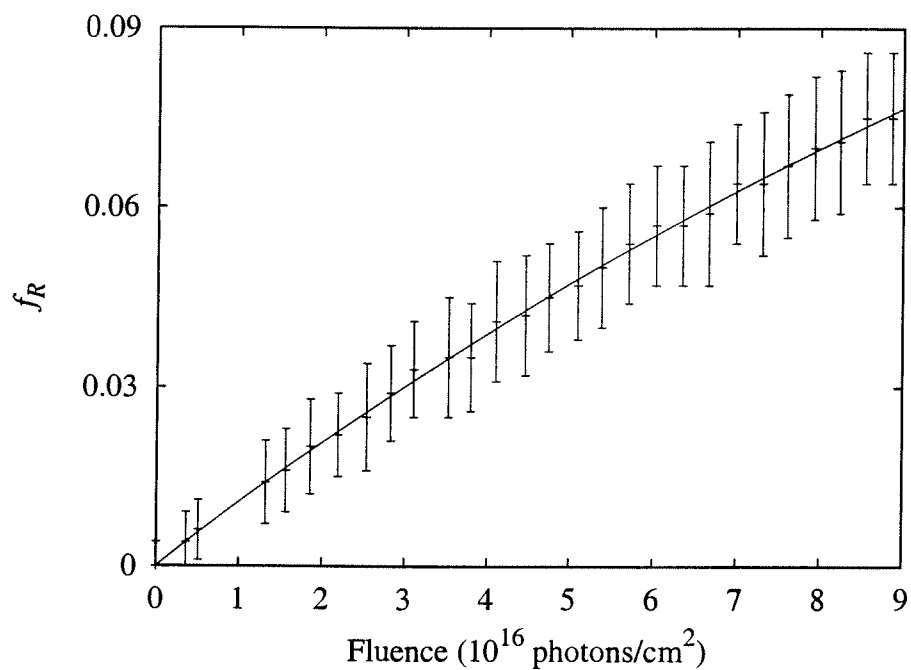


Figure 3.13: Two-step laser-induced fluorescence ratio versus \mathcal{P}_2 fluence for 532- + 1064-nm excitation. Fitting the model described by Eq. (3.14) gives $\Phi_{\text{risc},T_2} = 0.0076 \pm 0.0002$ and $\tau_{T_2} = 1.56 \pm 0.01$ ps with $\chi_r^2 = 0.012$. Error bars indicate the standard deviation of from 26 to 370 double-pulse excitations.

possible to extract this parameter from a fit of the kinetic model to data obtained under conditions where f_R exhibits deviation from linearity.

The multistate kinetic model illustrated in Fig. 3.10 is not the only possible explanation for fluorescence following 532- + 1064-nm excitation. An alternative model that deserves consideration includes absorption of 1064-nm light by T_2 to populate T_4 , a state already shown to have a significant reverse intersystem crossing yield. On the basis of energetic considerations, the $T_2 \rightarrow T_4$ absorption process appears to be plausible, although restrictions such as those based on parity may disallow this transition. If reverse intersystem crossing were to occur predominantly from T_4 , then the expression for f_R given in Eq. (3.6) should be modified to give

$$f_R = \Phi_{\text{isc}} \Phi_{\text{risc}, T_4} \sigma_{T_1, T_2} \sigma_{T_2, T_4} F_2^2. \quad (3.22)$$

According to this model, f_R increases quadratically rather than linearly in F_2 because population of T_4 from T_1 requires the sequential absorption of two 1064-nm photons. The experimental data shown in Fig. 3.13 do not exhibit this behavior, which justifies our elimination of this alternative model.

Similar measurements probing T_3 (532- + 632-nm excitation) failed to detect any two-step laser-induced fluorescence. Based on the fluorescence detection limits of this system the quantum yield of reverse intersystem crossing from T_3 can be constrained to $\Phi_{\text{risc}, T_3} < 0.06$ using Eq. (3.6) with σ_{T_1, T_3} determined from Ref. [41] and f_R set equal to the uncertainty in the TSLIF measurement.

3.6 Discussion

Our value for the reverse intersystem crossing yield from T_4 , the green-excited triplet state, is significantly different than that found by Reindl and Penzkofer (0.12 vs. 0.80) [59]. Some difference in reverse intersystem crossing yields is

not unexpected because different solvents were used (phosphate-buffered saline vs. methanol). A more detailed reading of their analysis methods also suggests further reasons for this discrepancy. First, the 6-ps pulses used in their study were substantially shorter than the rotational diffusion time of rose bengal in methanol (180 ps [69]) and were sufficiently energetic to deplete the ground state, so it would seem necessary to include orientation effects in their model (see Appendix A). Second, the Reindl and Penzkofer model also assumes that S_1 has a thermalization time much shorter than the pulse length. On the basis of fluorescence risetime measurements, Alfano and Shapiro reported a thermalization time of 33 ± 5 ps for erythrosin in methanol [67]. Rose bengal and erythrosin have many similar photophysical properties, so Reindl and Penzkofer's assumption that their 6-ps pulses were much longer than the thermalization time would appear to be inaccurate.

The impact of assuming fast rotational and thermalization rates was explored numerically. Extending the models developed in §3.4.2 to simulate multiple single-color pulses, synthetic fluorescence data was generated in which $\Phi_{\text{risc},T_4} = 0.1$, $k_r = 3 \times 10^{10} \text{ s}^{-1}$, and $k_{rot} = 5.6 \times 10^9 \text{ s}^{-1}$. This synthetic data was then fit using a model in which k_r and k_{rot} were chosen to satisfy the assumptions of Reindl and Penzkofer (10^{12} and 10^{13} s^{-1} respectively). When a two-pulse pair is analyzed using this method, the optimization algorithm finds a best fit with $\Phi_{\text{risc},T_4} = 0.66$ rather than the input value of 0.1 used to generate the synthetic data set. Analysis of a train of six pulses produces the slightly more accurate value of 0.43. Based on this exploration it would appear that differing assumptions of thermalization and rotation rates may account for much of the discrepancy between the present results and those of Reindl and Penzkofer. As these results show, the two-pulse method is less robust than the six-pulse method. Both of these multi-pulse, fixed-fluence

methods are more sensitive to assumptions about rotational and thermalization rates than the fluence-dependent, single-pulse method described in 3.4.3.

The value of α , the scaling factor used in analyzing the one-color laser-induced fluorescence data, can be estimated from instrumental parameters. The fluorescence is collected by a 2-inch diameter lens placed approximately 10 cm from the excitation volume. This lens will collect 2% of the fluorescence. Approximately 30% of this light will pass through the linear polarizer. The interference filter has 40% transmission in a 10-nm band centered at 580 nm. Approximately 7% of the fluorescence will be transmitted by this filter. The OG570 filter has approximately 80% transmission in this region. Therefore the light reaching the photomultiplier represents approximately 0.03% of the total light emitted. At 25 μM concentrations there will be roughly 4×10^{14} molecules in the excitation volume. Assuming a fluorescence quantum yield of 0.0005, approximately 4×10^{-8} J of light will be emitted and 1×10^{-11} J will reach the photomultiplier when half of the molecules are excited. The photomultiplier converts this light to an electrical signal with a charge of 0.2 μC . This results in a gated integrator reading of 5 V. Reflections from the various optical components would reduce that reading to 4 V. That corresponds to $\alpha = 200$ after correcting for the difference between the 0.02 yield for combined radiative and non-radiative transitions and the assumed 0.0005 yield for fluorescence used in this calculation. In the results described earlier the best fit for α was 105, within a factor of 2 of our order-of-magnitude estimation. This provides further support for the validity of these results.

Reverse intersystem crossing yields have been calculated for a growing number of molecules. An aspect of this study that makes it of particular interest is that these yields have now been calculated for several triplet states of rose bengal. Previous workers in this field have suggested that molecules excited to T_n relax

rapidly to the next-lowest triplet and that triplet-singlet transfer is predominantly due to reverse intersystem crossing from this less-energetic state [52,59]. According to this model, the reverse intersystem crossing yield should be independent of the high-lying triplet state initially excited; experimental measurements clearly contradict this with a yield of $\Phi_{\text{risc},T_4} = 0.12$ if T_4 is initially excited to the much lower yield of $\Phi_{\text{risc},T_2} = 0.0076$ for the case of direct population of T_2 , with Φ_{risc,T_3} lying somewhere between these two.

To understand these results it is instructive to consider the energies of the relevant triplet and singlet states. The energies of the singlet states can be estimated from the peaks of the ground-state absorption spectrum. Similarly, the energies of the triplet states relative to T_1 can be estimated from triplet-triplet absorption spectra (see Chapter 2 and Refs. [73] and [65]). The energy of T_1 is 1.75 eV as determined from the phosphorescence spectrum of rose bengal in an alcohol solvent at 77 K [74]. These results have been compiled in Table 3.6. The energy gaps between the excited triplet states and the nearest less energetic singlet state are $\Delta E(T_2S_2) \approx 0.5$ eV, $\Delta E(T_3S_3) \approx 0.4$ eV, and $\Delta E(T_4S_4) \approx 0.1$ eV. Thus we find that the transition with the smallest energy gap exhibits the greatest reverse intersystem crossing yield ($\Phi_{\text{risc},T_2} = 0.0076$, $\Phi_{\text{risc},T_3} < 0.06$, $\Phi_{\text{risc},T_4} = 0.12$). Although this ordering is consistent with a simple interpretation of the energy gap law for nonradiative transitions (see §1.4.2), such an interpretation must be considered critically. As developed by Englman and Jortner [10], the energy gap law applies to a particular triplet-singlet pair, whereas here we are considering three such pairs. The strength of the spin-orbit coupling between different states may vary by several orders of magnitude. Since we do not know the values of the coupling parameters for the three transitions under consideration it is impossible to definitively attribute the entire variation in reverse intersystem crossing yield to differences in the energy gap.

Table 3.6: Energies of rose bengal excited states. Singlet-state energies are estimated from the ground-state absorption spectrum. Triplet-state energies are estimated from the T_1 absorption spectrum.

State	Energy (eV)	Ref.
S_1	2.10	This work
S_2	2.41	This work
S_3	3.51	This work
S_4	3.95	This work
T_1	1.75	[74]
T_2	2.92	This work
T_3	3.86	[73]
T_4	4.03	[65]

Chapter 4

Photochemistry of higher-lying states

4.1 Overview

The interest in photosensitive dyes such as rose bengal has been motivated primarily by their application to photodynamic therapy. As described in §1.5, photodynamic therapy (PDT) is a cancer treatment based on light-activated chemistry. In conventional PDT, the T_1 state of a photosensitive dye is excited by visible or near-infrared light. Collisional energy transfer from T_1 to 3O_2 produces 1O_2 and returns the photosensitizer to its ground state. Singlet oxygen reacts with a variety of cellular targets and will result in cell death if a sufficient dose of 1O_2 is delivered. Chemistry resulting from states other than T_1 has commonly been ignored, but there has been some interest in any novel photochemistry that might be accessible following excitation of higher-lying states.

This chapter begins by describing several shortcomings of conventional photodynamic therapy as well as the various remedies that have been proposed. One

of those remedies addresses the limitations of conventional photodynamic therapy by proposing a two-step excitation of higher-lying states possessing novel photochemistry. Prior work with rose bengal has shown that it can produce oxygen-independent biological damage from certain higher-lying singlet and triplet states, but not from others. This damage results from the cleavage of one of rose bengal's carbon-iodine bonds.

The rose bengal T_2 state, newly identified here, possesses an energy of approximately 2.92 eV, greater than the carbon-iodine bond energy reported in many other molecules. This chapter describes experimental work conducted to determine whether excitation of T_2 results in cleavage of this bond. The data obtained in a two-step laser-induced bleaching experiment rule out any significant photochemistry from this state. One hypothesis for the presence of such chemistry in certain triplet states and not others is based on differences in reverse intersystem crossing yields. A theoretical model is presented that allows this hypothesis to be tested quantitatively. It is shown that reverse intersystem crossing cannot account for all of the observed differences. Finally, the feasibility of a two-step activated phototherapy is discussed.

4.2 Limitations of conventional photodynamic therapy and proposed remedies

The major side effect of photodynamic therapy using first generation photosensitizers is prolonged cutaneous photosensitivity. Low levels of the photosensitizing agent remain in the skin for many days after the treatment, necessitating the avoidance of brightly lit environments by the patient. In practice this means that the patient must avoid both direct and indirect sunlight as well as fluorescent

lights. In the case of Photofrin, cutaneous photosensitivity can last from one to four months [75]. Reactions include mild erythema¹ and inflammation, swelling, blistering, ocular discomfort, and pruritus². Despite warnings to wear proper clothing and avoid sunlight and bright fluorescent lights, patient compliance with these restrictions tends to be poor. Reducing the length of time during which patients must contend with cutaneous photosensitivity represents a significant improvement in photodynamic therapy.

Conventional photodynamic therapy requires oxygen and therefore may be limited in its effectiveness by the unavailability of oxygen. A lack of oxygen in the tumor can result from chronic, acute, or PDT-induced hypoxia. The condition labeled chronic hypoxia was identified in 1955 by Thomlinson and Gray [76]. Insufficient oxygenation in these cells simply results from an inadequate capillary density. The low density of capillaries causes a mismatch between the rate at which oxygen can be supplied and the rate at which it is consumed through metabolic processes. Such tumor regions were initially of interest because hypoxic cells can survive approximately three times more radiation than normally oxygenated cells [77].

Acute hypoxia, as described in 1979 by Brown [78], is a transient oxygen deficit resulting from the temporary closure of blood vessels in and around tumors. This type of hypoxia, unlike the chronic hypoxia described by Thomlinson and Gray, can even affect cells very close to blood vessels. More direct evidence for fluctuations in oxygenation comes from the work of Reinhold *et al.* [79] which monitored oxygenation in tumors using the NADH fluorescence technique of Chance *et al.* [80,81]. This work revealed that approximately 10 – 20% of the mouse tumor experienced acute hypoxia at any given time.

¹Erythema is an abnormal redness of the skin due to inflammation.

²Pruritus is a localized or general itching due to irritation of the sensory nerve endings.

In the 1990s the work of Foster *et al.* [82–85] demonstrated the existence of a type of hypoxia unique to photodynamic therapy. Oxygen is consumed during photodynamic therapy as singlet oxygen reacts with various biological targets. If the intercapillary spacing is large enough, PDT-induced oxygen consumption can exceed the rate of diffusional resupply. The PDT-induced hypoxic regions between capillaries are protected from further singlet oxygen-mediated damage, allowing these cells to survive. PDT-induced hypoxia results from an excessive rate of oxygen consumption and therefore depends on the irradiation fluence rate.

Various modifications of conventional photodynamic therapy have been proposed to address the problems of cutaneous photosensitivity and tumor hypoxia described above. These remedies have taken both chemical and physical approaches to solving one or both of these problems. A few of these alternatives will be reviewed before a two-step activation proposal that involves higher-lying states is described.

Several chemical approaches to minimizing cutaneous photosensitivity have been studied. These include the use of anti-oxidants to minimize the damage caused by singlet oxygen produced post-therapy [86] as well as the design of photosensitizers which have better specificity and/or clearance rates than Photofrin, the most successful first generation drug. Second-generation photosensitizers have already proven to be significantly superior compared to Photofrin, in this respect. For example, the tumor to muscle ratios of the photosensitizer lutetium texaphyrin have been reported to be as high as 10:1 within 5 hours of injection ($4.72 \mu\text{g/g}$ versus $0.46 \mu\text{g/g}$) [87]. Within twenty four hours the tumor to plasma ratio of lutetium texaphyrin is greater than 16:1. The animals treated in these studies showed no signs of skin photosensitivity. Another example in which the specific biological differences between normal and cancerous cells was exploited is a

study in which rose bengal was chemically modified to contain an acetate group which quenched fluorescence and intersystem crossing [88]. The targeted cells (rat glioma) display enhanced activity of the enzyme carboxylic esterase. This enzyme removes the acetate group, restoring the dye to its photodynamically-active form. As a result of the differences in the activity of this enzyme between normal and cancerous cells, the photodynamic effect can be targeted at only the undesirable cells.

The problem of PDT-induced hypoxia can be addressed by reducing the fluence rate, either by using a lower average power or by fractionating the dose. The decreased fluence rate reduces the rate of oxygen consumption, thereby minimizing this type of hypoxia. Experimental work by Foster *et al.* confirmed this theory in a multicell tumor spheroid system by demonstrating increased cytotoxicity with a reduction of the fluence rate [84]. Fluence rate effects had also been previously observed by Gibson *et al.* in Fischer rats implanted with the R3230AC mammary adenocarcinoma [89] and by Feins *et al.* in nude mice implanted with human mesothelioma [90]. A reduced fluence rate can help overcome PDT-induced hypoxia but does not address the problem of chronic or acute hypoxia.

Leupold and Freyer [91,92] have proposed an alternative approach based on the use of two-step excitation, as shown in Fig. 4.1. The two-step activation they proposed minimizes cutaneous photosensitivity and possibly results in oxygen-independent damage. This approach requires sensitizers that do not produce singlet oxygen following the absorption of a single photon. Such sensitizers would either have negligible intersystem crossing or have a triplet state lying below that needed for generation of $^1\text{O}_2(\Delta_g)$. Illumination by conventional light sources would therefore not produce any harmful effects. However, the much greater intensities that can be generated by a pulsed laser allow for two-step excitation of

either higher-lying singlet or triplet states as shown in Fig. 4.1. These states can potentially produce either monomolecular or bimolecular photochemistry. The existence of oxygen-independent chemistry involving these states is of particular interest.

4.3 Objections to the Leupold-Freyer two-step activation proposal

Several objections to the Leupold-Freyer two-step activation proposal have been raised by Vidoczy [93]. First, the possibility of bimolecular reactions from higher-lying states was challenged on the basis of the short lifetimes of these states. Vidoczy's second objection was that monomolecular damage mechanisms were not known to exist for photodynamic therapy. Finally, Vidoczy claimed that producing significant population in higher-lying states would require laser pulses with intensities that would cause dielectric breakdown and other unwanted effects. This last objection will be discussed in §4.8.

Vidoczy's claim that bimolecular reactions cannot occur from higher-lying states is contradicted by experimental observations of such reactions. As an example of a bimolecular reaction which does occur, Kobyshev *et al.* [94] report that the first excited singlet state of naphthalene can be generated by higher-lying triplet states of fluorescein. The energy transfer does not occur from T_1 , but requires the more energetic T_3 , which Kobyshev *et al.* produced by two-step excitation.

Numerous reports of monomolecular reactions for photosensitizers such as protoporphyrin-IX, hematoporphyrin derivative, and rose bengal refute Vidoczy's claim that monomolecular damage mechanisms do not exist for PDT. An exam-

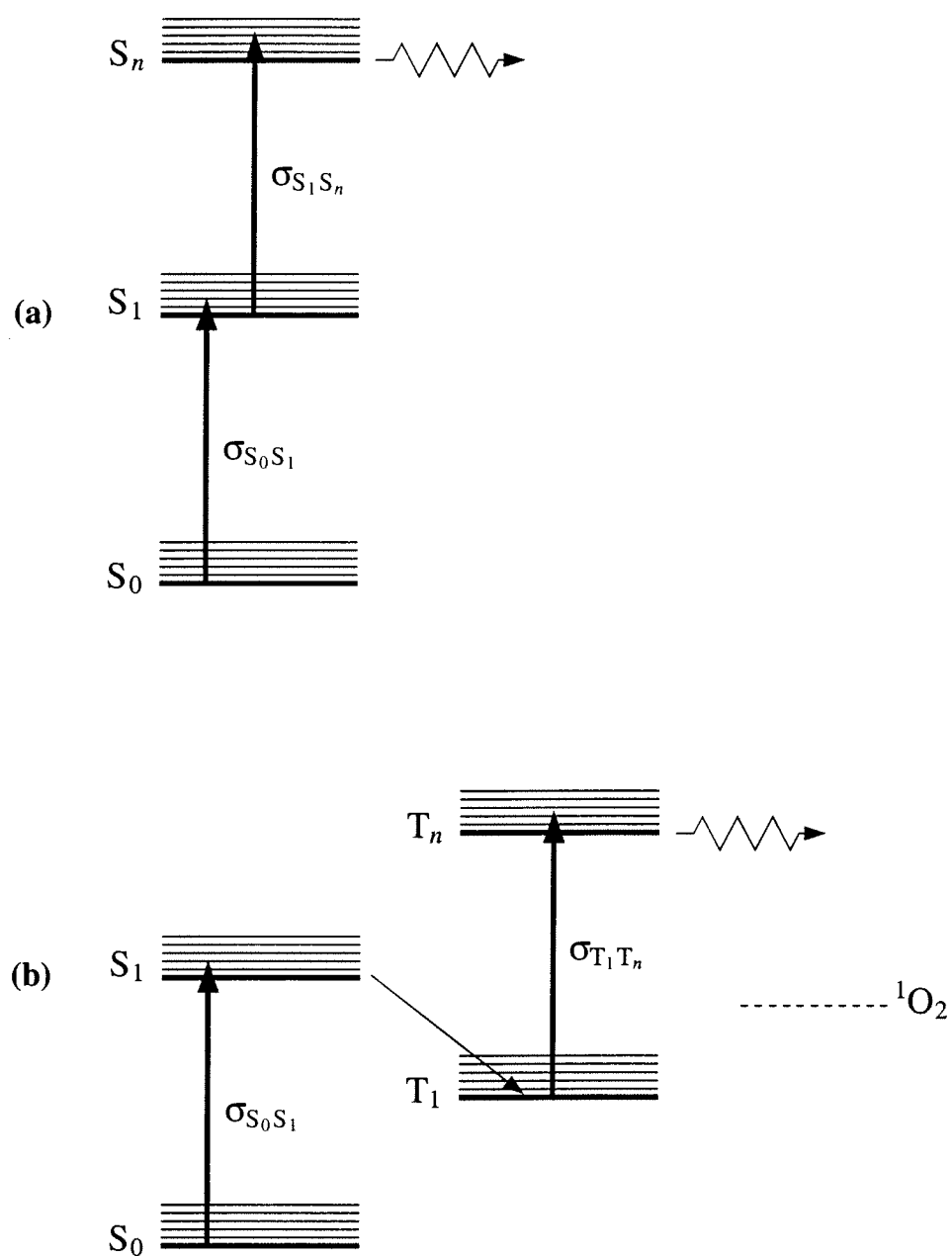


Figure 4.1: Energy level diagrams for two-step activated photodynamic therapy. Cutaneous photosensitivity can be avoided if photochemistry occurs only from (a) higher-lying singlet states or (b) higher-lying triplet states.

ple of such a reaction in protoporphyrin-IX was reported by Karu *et al.* [95] in 1981. They showed that photochemical reactions unique to the higher-lying singlet states could be produced by intense excitation of protoporphyrin-IX with picosecond pulses of 532-nm light. Monomolecular reactions have also been observed from the higher-lying states of hematoporphyrin derivative (HpD). In 1982 Andreoni *et al.* [96] described their two-step excitation of HpD by pulsed UV light. It was believed that cells could be damaged either by singlet oxygen produced from T_1 or by HpD radicals generated following the absorption of a second UV-photon. A biological assay found that pulsed irradiation was 1.5 times more toxic to HpD-incubated cells than continuous irradiation with the same average power. The damage resulting from pulsed irradiation was found to scale quadratically with the intensity of the nanosecond pulses of 337-nm light, indicating two-photon-activated photochemistry. A subsequent study by Andreoni [97] showed that similar damage could be produced by either one-color (630-nm) or two-color excitation (630- + 481-nm) of HpD by nanosecond pulses. By varying the interpulse delay in the two-step excitation, Andreoni was also able to determine that generation of high-lying triplets resulted in damage processes different from those occurring from high-lying singlet states. Enhanced photosensitization has also been discovered for the higher-lying states of rose bengal [63, 73, 98, 99].

4.4 Photochemistry of the higher-lying states of rose bengal

Rose bengal photochemistry has been the subject of ongoing studies by a group at the Wellman Laboratories of Massachusetts General Hospital [65, 73, 98–101]. In 1989 Fluhler *et al.* [98] reported enhanced photosensitizing efficiency when rose

bengal was excited by ultraviolet light. Using inhibition of red blood cell acetylcholinesterase as a biological assay for photodynamic damage, they found a 50% greater toxicity for excitation of a higher-lying singlet state of rose bengal by 308-nm light compared to the effect obtained by exciting S_1 using 514-nm light. Higher-lying state photochemistry was believed to be possible because of the relatively large energy gap between these states, suppressing rapid internal conversion. An attempt was also made to produce this effect through excitation of a higher-lying singlet by the sequential absorption of two photons of 532-nm light from a 40-ps pulse. No effect beyond that expected for conventional photosensitization was observed.

Results of further studies of high-lying singlet state photochemistry in rose bengal were reported in 1991 by Allen *et al.* [99]. Delivering up to a hundred times more photons than in the previous study, these authors found up to a 2-fold enhancement of photosensitization for 313-nm excitation compared to 514-nm excitation. Singlet oxygen production was monitored through the characteristic 1270-nm luminescence of the excited oxygen species. The yield of singlet oxygen was found to be independent of the excitation wavelength and therefore could not be used to explain the observed differences in photosensitization. Using the bleaching of N,N-dimethylnitrosoaniline (RNO) as an indicator of radical production revealed that radical production occurred only from the higher-lying singlet state. The nature of the radicals was revealed by a spectrophotometric assay for I_2 . Molecular iodine was believed to be a stable end product resulting from the I^\cdot radical generated by carbon-iodine bond cleavage. The quantum yield of iodine formation following 313-nm excitation as measured by this assay was 0.0041 ± 0.0005 . However, it is not clear from this measurement whether $I^{\cdot-}$ or the complementary $RB^{\cdot+}$ is the species responsible for the enhanced phototoxicity.

In either case, it appears to be much more potent than singlet oxygen. Allen *et al.* calculate that in order to account for the two-fold enhancement in enzyme inhibition the radicals must be approximately 183 times more damaging than singlet oxygen. In both this report and their earlier work, enzyme inhibition was found to depend linearly on the number of absorbed photons.

In 1994, Smith *et al.* [73] expanded the investigation of rose bengal photochemistry to include processes following excitation of higher-lying triplet states. A higher-lying triplet state was populated by two-color excitation with \mathcal{P}_1 either an 8-ns pulse at 308-nm or a 10-ns pulse at 532-nm, and \mathcal{P}_2 a 400-ns pulse at 640-nm. The two pulses were separated by 1.2 μ s. Smith *et al.* found strong evidence for radical formation from this higher-lying triplet state, which we denote as T_3 . First, a 50% transient bleaching of the T_1 absorption was observed following \mathcal{P}_2 , indicating that T_3 did not solely relax through internal conversion. Further photophysical evidence for radical formation includes the observation of increased absorption at 470 nm, the location of a $RB^{\cdot+}$ absorption peak [102]. Two biological assays were also employed in this study: the acetylcholinesterase inhibition measurement used in the previous investigations and a test of plasma membrane integrity using P388D₁ cells and trypan blue staining. Four cases were studied using each assay. These cases tested the difference between only \mathcal{P}_1 excitation and dual excitation by \mathcal{P}_1 and \mathcal{P}_2 under both air-saturated and nitrogen-purged conditions. Under the air-saturated conditions \mathcal{P}_1 excitation produced a 21% inhibition of enzyme activity whereas $\mathcal{P}_1 + \mathcal{P}_2$ resulted in 25% inhibition. Nitrogen-purging prevents enzyme inhibition if rose bengal is only excited by \mathcal{P}_1 , but the combination of $\mathcal{P}_1 + \mathcal{P}_2$ was still able to reduce enzyme activity by 16%. The ability to cause damage independent of oxygen is impressive, but the small enhancement in phototoxicity under air-saturated conditions is also noteworthy once one accounts

for the 50% T_1 depletion caused by \mathcal{P}_2 , indicating significant oxygen-independent damage also occurs under those conditions. Similar results are found with the membrane integrity assay. 14% of the cells are stained by trypan blue after \mathcal{P}_1 excitation in air-saturated samples, with that fraction increasing to 18% with two-color excitation. Nitrogen-purging does not completely eliminate the effects of \mathcal{P}_1 excitation (7% stained) but two-color excitation results in 16% of the cells taking up trypan blue. The radical quantum yield from T_3 was unknown but assumed to be approximately equal to that found for the UV-excited singlet state. A significant chemical yield despite a low quantum yield was explained by rapid cycling between T_1 and T_3 during the 400-ns long \mathcal{P}_2 pulse.

The possibility of using nanosecond pulses of 532-nm light to excite higher-lying triplet states of rose bengal through two-step sequential absorption was investigated in 1996 by Lambert *et al.* [65]. Two photons of 532-nm light provide sufficient energy to populate a state even more energetic than the high-lying states studied in the previous work of the Kochevar group. As mentioned above, Fluhler *et al.* had investigated the possibility of sequential two-photon absorption within the singlet manifold using 40-ps pulses and found no effect. A photophysical study by Stiel *et al.* confirmed that S_1 has no measurable absorption at 532 nm [14]. However, by using 8-ns pulses Lambert *et al.* could create T_1 with the first portion of the pulse and then excite it to a higher-lying triplet state, which we denote as T_4 , with the remainder of the pulse. No evidence of higher-lying state chemistry was observed using the acetylcholinesterase assay even though there is significant triplet-triplet absorption at 532-nm. Stiel *et al.* studied the non-linear transmission of picosecond and nanosecond pulses of 532-nm light through rose bengal. A kinetic model analysis of this data returned an upper limit of 0.0005 for the yield of photoproduct formation from T_4 . The kinetic model of Stiel *et al.* did

not include reverse intersystem crossing or photoselection effects. Our attempts to re-analyze the Stiel *et al.* transmission data with the more complete model described below failed to find any dependence on the radical formation yield.

In addition to the studies described above which explicitly investigated the photochemistry of higher-lying states, work by Ciulla *et al.* [100] at the Wellman Laboratory had found that rose bengal could cause single-strand breaks in pBR322 DNA under continuous illumination. They used a filtered quartz tungsten halogen lamp to produce 2.9 mW/cm^2 in a 50-nm band centered on 540 nm. The creation of single-strand breaks proceeded with a first order rate constant, and compared to an oxygen-saturated sample this rate increased by a factor of 3.9 and 24 for nitrogen and argon purged samples, respectively. The single-strand breaks were believed to be initiated by T_1 or RB' , but no mechanism was definitively assigned. This same phenomena was observed earlier by Peak *et al.* [103] but that study found no oxygen-dependence. As a result of the low light levels used in these studies, it does not appear that this non-oxygen-mediated damage can be ascribed to higher-lying state photochemistry.

4.5 Bond cleavage

Bond cleavage is believed to be the mechanism responsible for much of the oxygen-independent damage that results from excitation of a higher-lying state. The process of bond cleavage can result from direct excitation of a dissociative state. Alternatively, excitation of a high-lying bound state can result in bond cleavage if there is some overlap between the wavefunctions associated with that state and a dissociative state [104]. This second pathway is called predissociation, and the relevant states are illustrated by the potential energy curves shown in Fig. 4.2. The time scale for direct dissociation is one vibrational period of the bond under-

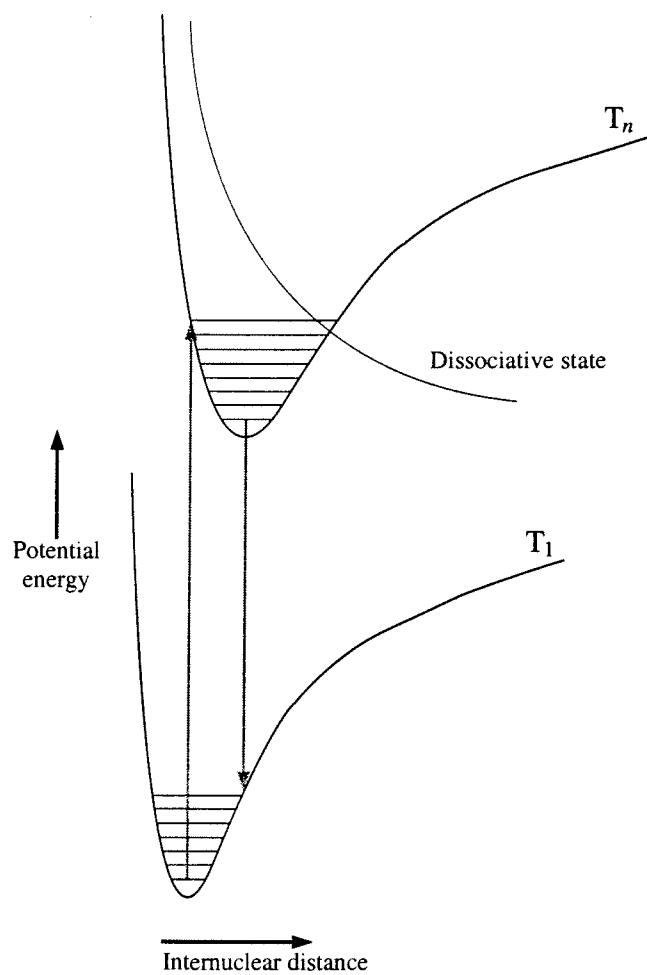


Figure 4.2: Potential energy curves for states in the predissociation pathway.

going dissociation. The predissociative mechanism takes place more slowly since it requires the transfer between two states which might have only a small overlap. In this case dissociation can require a hundred or more vibrational periods. Therefore bond cleavage that occurs through the predissociative mechanism will be more sensitive to the photophysical properties of the higher-lying state.

The carbon-iodine bond energy depends on its larger molecular context. For example, the review article by McMillen and Golden [105] states that the carbon-iodine bond energy is 65.4 ± 2 kcal/mol (2.8 ± 0.1 eV) for C_6H_5-I , 57.2 ± 0.3 kcal/mol (2.45 ± 0.01 eV) for CH_3-I , 53.4 ± 1 kcal/mol (2.29 ± 0.04 eV) for C_2H_5-I , and 48.2 ± 1.5 kcal/mol (2.1 ± 0.1 eV) for $CH_2C_6H_5-I$. The equivalent carbon-bromine bonds are approximately 20-25% stronger. Earlier reviews by Kerr [106] and Benson [107] report smaller values for the carbon-iodine bond dissociation energies in $CH_2C_6H_5-I$ (40 kcal/mol) and CH_3-I (56 kcal/mole) and a comparable value for C_2H_5 (53 kcal/mol). The bond dissociation energies listed in these three reviews are for gas phase molecules. According to Laarhoven *et al.* the bond dissociation energies in a nonpolar solvent should be the same as those in the gas phase [108]. However, bond dissociation energies will increase in polar solvents to include the energy required for solvation. Additional energy is required if there is hydrogen bonding between the solute and solvent. For example, the O-H bond dissociation energy in phenol ranges from 86.2 kcal/mol for the solvent isooctane to 96 kcal/mol in triethylamine.

Delivering energy greater than that required for bond dissociation is not necessarily sufficient to result in bond cleavage. For example, Scaiano *et al.* conclude that an upper triplet state of benzophenone, containing over 25 kcal/mol more energy than is required to cleave the weakest bond, does not produce any photo-products because it is efficiently quenched by the solvent (benzene) [109]. Thus, bond cleavage requires both excess energy and a higher-lying state that is sufficiently long-lived.

4.6 Measurements of T_2 photochemistry

Experiments were performed to determine whether bond cleavage occurs following excitation of rose bengal's T_2 state and are described in this section. A two-step laser-induced bleaching technique was used to measure the yield of bond cleavage following excitation of T_2 . We discussed a similar technique in the context of reverse intersystem crossing in Chapter 3. The modifications required to include photochemistry in the analysis of two-step laser-induced bleaching are discussed before a description of the experimental setup.

4.6.1 Theoretical basis of two-step laser-induced bleaching

Higher-lying triplet states can be populated through two-step laser excitation. The first pulse of light, \mathcal{P}_1 , is absorbed by the ground state of the molecule and populates an excited singlet state, S_1 . This state can relax to the ground state, producing fluorescence. Alternatively, it can undergo intersystem crossing to the lowest triplet state, T_1 . The second pulse, \mathcal{P}_2 , is delayed so that it arrives after S_1 has depopulated, but before T_1 has relaxed substantially. The \mathcal{P}_2 light is absorbed by T_1 and populates a higher-lying triplet state, T_n , where $n > 1$. This state can relax through internal conversion back to T_1 or through reverse intersystem crossing it can populate a less energetic singlet state, S_m , where $m \geq 1$. Population in S_m rapidly decays to S_1 , where it can subsequently fluoresce or return to T_1 . This process is the subject of Chap. 3. Alternatively, molecules in the energetic T_n state can undergo chemical reactions such as bond cleavage which reduce the concentration of the photosensitizer.

The bleaching of T_1 due to reverse intersystem crossing and photochemical reactions during two-step excitation can be measured using transient absorption spectroscopy. The state T_n has a short lifetime compared to that of T_1 . If

internal conversion is the only process occurring from T_n , the pre- \mathcal{P}_2 and post- \mathcal{P}_2 populations of T_1 will be virtually identical. However, reverse intersystem crossing and chemical reactions will reduce the fraction of molecules excited to T_n that subsequently return to T_1 , producing a transient photobleaching.

The fractional change in T_1 absorption resulting from photochemistry is given by

$$\left(\frac{\Delta A}{A_0}\right)_{\text{chem}} = -\Phi_{\text{chem},T_n} N_{\text{abs}} \quad (4.1)$$

where Φ_{chem,T_n} is the quantum yield of the chemical reaction occurring following excitation of T_n and N_{abs} is the average number of photons absorbed by a molecule in the T_1 state during \mathcal{P}_2 . The bleaching due to reverse intersystem crossing results from the fraction of the population transferred from T_n to the singlet manifold but which does not subsequently return to T_1 via intersystem crossing from S_1 . The fractional change in triplet-triplet absorption resulting from this photophysical effect is given by

$$\left(\frac{\Delta A}{A_0}\right)_{\text{risc}} = -(1 - \Phi_{\text{isc}})\Phi_{\text{risc},T_n} N_{\text{abs}} \quad (4.2)$$

where Φ_{risc,T_n} is the $T_n \rightarrow S_1$ intersystem crossing yield that can be determined using techniques such as those described in Chap. 3.

The observed change in T_1 absorption because of \mathcal{P}_2 will equal the sum of these two effects:

$$\left(\frac{\Delta A}{A_0}\right)_{\text{expt}} = \left(\frac{\Delta A}{A_0}\right)_{\text{chem}} + \left(\frac{\Delta A}{A_0}\right)_{\text{risc}} \quad (4.3)$$

$$= -[\Phi_{\text{chem},T_n} + (1 - \Phi_{\text{isc}})\Phi_{\text{risc},T_n}] N_{\text{abs}} \cdot \quad (4.4)$$

It is therefore possible to determine Φ_{chem,T_n} from two-step laser-induced bleaching measurements if Φ_{isc} and Φ_{risc,T_n} are known. This analysis has assumed that \mathcal{P}_2 is not at a wavelength absorbed by the ground state and that the absorption probe

wavelength is exclusively absorbed by T_1 . If these assumptions are not met a more complete model of the kinetics is required.

The number of photons absorbed by $T_1 \rightarrow T_2$ excitation during \mathcal{P}_2 can be calculated using the kinetic model described by

$$\begin{aligned}
 \frac{dp_{S_0}(\theta, t)}{dt} &= (1 - \Phi_{\text{isc}})\tau_{S_1}^{-1}p_{S_1} + \tau_{T_1}^{-1}p_{T_1} - k_{\text{rot}}(p_{S_0} - \langle p_{S_0} \rangle) \\
 \frac{dp_{T_1}(\theta, t)}{dt} &= \Phi_{\text{isc}}\tau_{S_1}^{-1}p_{S_1} - \tau_{T_1}^{-1}p_{T_1} - 3\cos^2\theta\sigma_{T_1T_2}(p_{T_1} - p_{T_2})I(t) \\
 &\quad + (1 - \Phi_{\text{risc}, T_2})\tau_{T_2}^{-1}p_{T_2} - k_{\text{rot}}(p_{T_1} - \langle p_{T_1} \rangle) \\
 \frac{dp_{S_1}(\theta, t)}{dt} &= k_r p_{S'_1} - \tau_{S_1}^{-1}p_{S_1} - k_{\text{rot}}(p_{S_1} - \langle p_{S_1} \rangle) \\
 \frac{dp_{S'_1}(\theta, t)}{dt} &= -k_r p_{S'_1} + \Phi_{\text{risc}, T_2}\tau_{T_2}^{-1}p_{T_2} - k_{\text{rot}}(p_{S'_1} - \langle p_{S'_1} \rangle) \\
 \frac{dp_{T_2}(\theta, t)}{dt} &= 3\cos^2\theta\sigma_{T_1T_2}(p_{T_1} - p_{T_2})I(t) - \tau_{T_2}^{-1}p_{T_2} - k_{\text{rot}}(p_{T_2} - \langle p_{T_2} \rangle)
 \end{aligned} \tag{4.5}$$

where the p_i are the orientational subpopulations of S_0 , T_1 , S_1 , S'_1 , and T_2 . See Appendix A for a discussion of optical transitions and molecular orientation. Table 4.1 lists the definitions and values of the photophysical parameters. The orientational average of this model, which eliminates the θ dependence, is shown in Fig. 4.3. It should be noted that this model does not include a rate for photochemical reactions from T_2 . The yield of this process is unknown and the intent of the two-step laser-induced bleaching experiment is to determine it. The yield is expected to be small so its exclusion from the model should cause only a minor change in N_{abs} . The time-dependent absorption rate is integrated temporally and spatially averaged to give

$$N_{\text{abs}} = \left\langle \int_{-\infty}^{+\infty} 3\cos^2\theta\sigma_{T_1T_2}(p_{T_1} - p_{T_2})I(t) dt \right\rangle \tag{4.6}$$

Table 4.1: Photophysical parameters for 1064-nm excitation of the T_1 state of rose bengal

Symbol	Description	Value	Ref.
σ_{T_1, T_2}	Triplet absorption cross section at 1064 nm ($T_1 + \hbar\omega \rightarrow T_2$)	$1.1 \times 10^{-16} \text{ cm}^2$	Chap. 2
τ_{S_1}	Lifetime of S_1	89 ps	[14–16]
τ_{T_1}	Lifetime of T_1 (includes both phosphorescence and oxygen quenching)	3 μs	[66]
τ_{T_2}	Lifetime of T_2	1.56 ps	Chap. 3
Φ_{isc}	Intersystem crossing yield ($S_1 \rightarrow T_1$)	0.98	[16, 66]
Φ_{risc, T_2}	Reverse intersystem crossing yield ($T_2 \rightarrow S'_1$)	0.0076	Chap. 3
I	\mathcal{P}_2 photon intensity	variable	—
k_{ic, T_2}	Internal conversion rate ($T_2 \rightarrow T_1$)	$(1 - \Phi_{\text{risc}, T_2})/\tau_{T_2}$	—
k_{risc, T_2}	Reverse intersystem crossing rate ($T_2 \rightarrow S'_1$)	$\Phi_{\text{risc}, T_2}/\tau_{T_2}$	—
k_r	Thermalization rate ($S'_1 \rightarrow S_1$)	$3 \times 10^{10} \text{ s}^{-1}$	[67, 68]
k_{rot}	Rotational diffusion rate	3.2 ns $^{-1}$	[69]

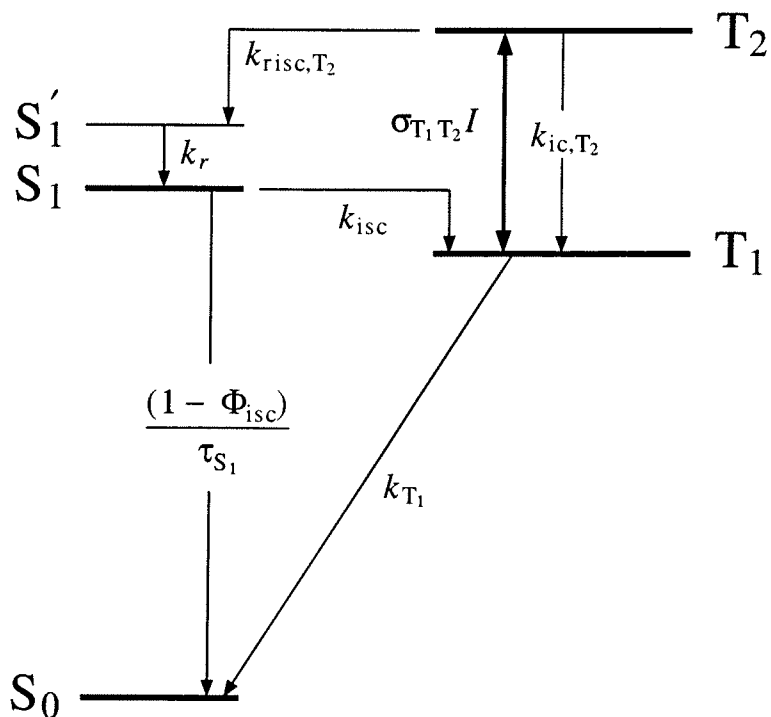


Figure 4.3: Energy-level scheme for 1064-nm excitation of the T_1 state of rose bengal, corresponding to an orientational-average of Eq. (4.5). See Table 4.1 for parameter descriptions and values.

where $p_{T_1}(\theta, t)$ and $p_{T_2}(\theta, t)$ are calculated from the kinetic model described by Eq. (4.5). The conditions immediately prior to the arrival of \mathcal{P}_2 were set to $\langle p_{T_1} \rangle \leftarrow 0.99 \langle p_{T_1} \rangle$ and $\langle p_{S_0} \rangle \leftarrow \langle p_{S_0} \rangle + 0.01 \langle p_{T_1} \rangle$, accounting for the decay of T_1 population between \mathcal{P}_1 and \mathcal{P}_2 .

If there is minimal depletion of T_1 during \mathcal{P}_2 then $N_{\text{abs}} = \sigma_{T_1, T_n} F_2$, where σ_{T_1, T_n} is the triplet-triplet absorption cross section and F_2 is the photon fluence of \mathcal{P}_2 . The extent of the depletion of T_1 also depends on τ_2 , the pulse length of \mathcal{P}_2 , and τ_{T_n} , the lifetime of T_n . The minimal depletion limit applies when

$$\sigma_{T_1, T_n} F_2 e^{-\tau_2/\tau_{T_n}} < 0.1 \quad (4.7)$$

and

$$(\Phi_{\text{chem}, T_n} + \Phi_{\text{risc}, T_n}) \sigma_{T_1, T_n} F_2 < 0.1 . \quad (4.8)$$

When these conditions are not met N_{abs} must be determined from the more detailed calculation accounting for the complete population dynamics, described above. It should be noted that the photoselection effects discussed in Appendix A also apply to triplet-triplet absorption and must be considered if significant depletion of T_1 occurs. In the T_2 bleaching experiments described below, such an approach was used because $\sigma_{T_1, T_2} F_2 \approx 6.9$ and photoselection effects for rose bengal in water are significant for pulse lengths of ~ 190 ps.

4.6.2 Experimental methods and results

The two-step laser-induced bleaching measurements probing radical formation from T_2 were made with the optical layout shown in Fig. 4.4. The final output of the laser system is a pulse with a length of ~ 190 ps, a wavelength of 1064 nm and an energy exceeding 2 mJ. In this experiment the second harmonic was generated from the laser fundamental using a KDP crystal (SHG), resulting in a pulse with

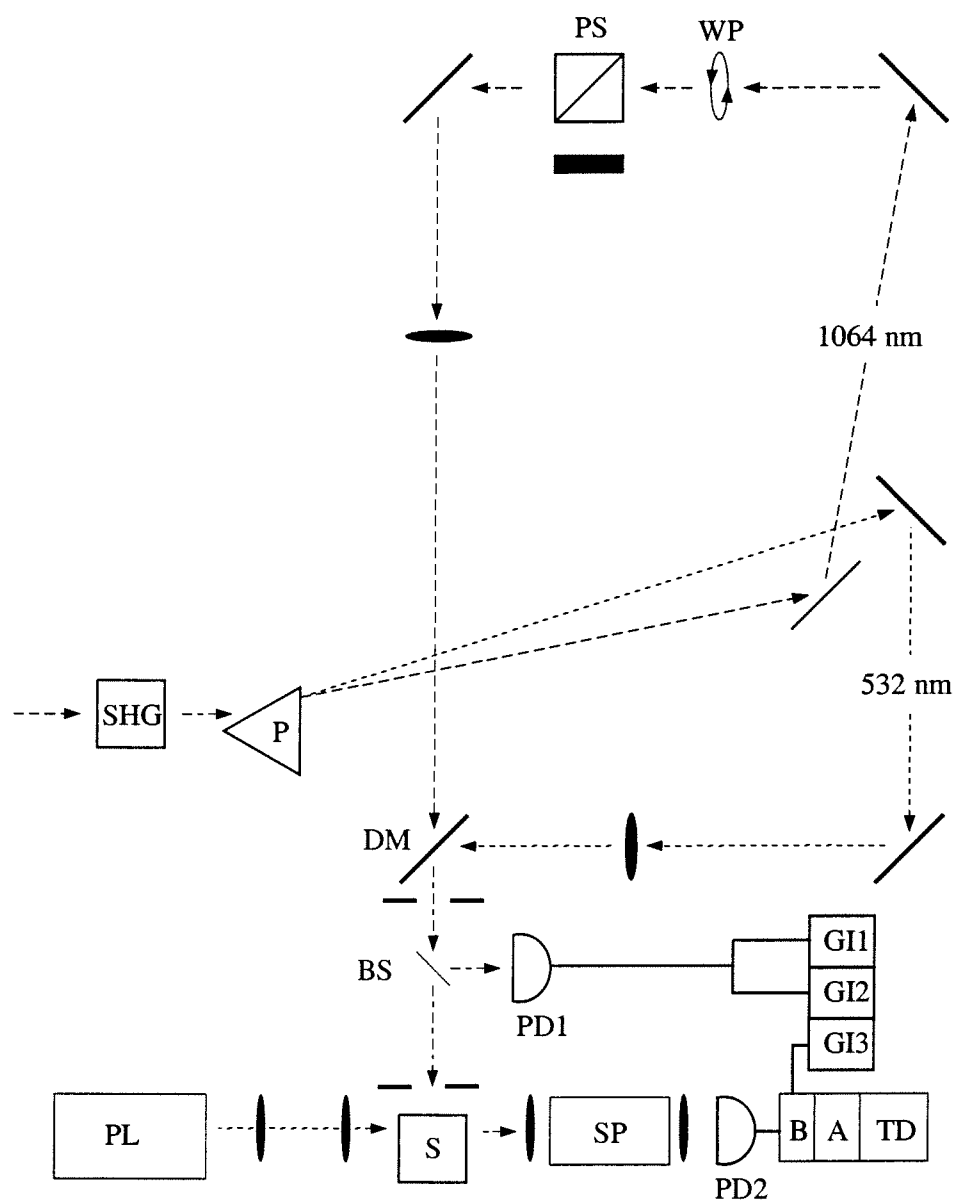


Figure 4.4: Experimental setup for two-step laser-induced bleaching measurements ($\lambda_1 = 532$ nm and $\lambda_2 = 1064$ nm). See Table 4.2 for symbol definitions.

Table 4.2: Equipment used in the two-color laser-induced bleaching experiments

	Description	Details
A	fast amplifier	EG&G, 574
B	back-off circuit	
BS	beam splitter	microscope slide ($\sim 4\%$ reflection)
DM	dichroic mirror	R@532 nm, T@1064 nm
GI1-3	gated integrator	Stanford Research Systems, 250
P	prism	
PD1-2	photodiode	EG&G, FND-100
PL	mercury arc lamp fast shutter long-pass filter	Olympus, 100 W Vincent Assoc., Uniblitz VS25 Schott, RG695
PS	polarizing beam splitter	$\lambda=1064$ nm
S	sample cuvette and beam mask	
SHG	second harmonic generator	KDP crystal
SP	monochromator, 13 nm BW	Instruments SA, H20
TD	digitizing oscilloscope	Hewlett-Packard, HP54201A
WP	half-wave plate	$\lambda=1064$ nm

a wavelength of 532 nm, a pulse length of ~ 130 ps, and energy greater than $250 \mu\text{J}$. To achieve a high degree of spectral separation between the fundamental and second harmonic pulses, a prism (P) is used to spatially disperse the two beams. The first pump pulse, \mathcal{P}_1 , has a wavelength of 532 nm and the second pump pulse, \mathcal{P}_2 has a wavelength of 1064 nm. \mathcal{P}_2 is delayed by 34 ns relative to \mathcal{P}_1 by traversal of a greater optical path length. The pump pulses are recombined spatially at a dichroic mirror (DM). The pulses overfill a 2-mm by 4-mm opening in a masked cuvette holder (S). A small fraction of excitation light is reflected by a glass plate shortly after the dichroic mirror and is incident upon a silicon photodiode. The signal generated by this monitor light is sampled by two gated integrators (GI1 and GI2) which distinguish between the \mathcal{P}_1 and \mathcal{P}_2 signals. The pump-pulse signals are calibrated individually using an energy meter. Transient absorption changes are probed by a broadband light beam traveling along the length of the irradiated zone (perpendicular to the pump pulses). The probe pulse has a 20-ms duration and is produced by a mercury lamp followed by a long-pass filter and fast mechanical shutter. This collection of elements is represented by PL in Fig. 4.4. The probe pulse passes through a monochromator (SP) before being detected by a silicon photodiode (PD2). The photodiode signal is passed through an electronic back-off circuit (B). The back-off circuit consists of a sample-and-hold unit and a differential amplifier. The sample-and-hold unit is used to acquire the baseline voltage. This baseline is then subtracted from the transient produced by the two pump pulses by the differential amplifier. This baseline-corrected signal is then increased by a multistage amplifier (A) to levels which would not be possible if the baseline were included, increasing the sensitivity of the system. This amplified signal is then recorded by a digital oscilloscope (TD). The baseline voltage acquired by the sample-and-hold circuit is sampled by a

gated integrator (GI3). The average signal from 256 shots is then transferred at 11-bit resolution to a computer for analysis.

The probe wavelength in the two-step laser-induced bleaching experiment is 920 nm. This is a wavelength of light absorbed by T_1 and not by the ground state, as shown in Figures 2.4 and 2.7. The use of such a wavelength simplifies analysis of triplet bleaching by eliminating absorption changes due to other states. Although not at the peak of the near-infrared triplet-triplet absorption, 920-nm light is more efficiently detected by the silicon photodiode than 1064-nm light, and therefore has a greater signal-to-noise ratio than wavelengths closer to the absorption peak. In addition, the use of a probe at 920 nm reduces interference that might occur from scattered \mathcal{P}_1 or \mathcal{P}_2 light.

The transient absorption detection system described is unable to temporally resolve between the arrival of \mathcal{P}_1 and \mathcal{P}_2 , so the bleaching due to higher-lying triplets can be seen only in the microsecond time-scale response. In order to properly compare the two irradiation schemes the \mathcal{P}_1 fluence must be kept constant and samples must contain identical concentrations of photosensitizer. It is essential that a new sample be used for each measurement as photobleaching via singlet oxygen-, S_1 -, or T_1 -mediated processes may occur [110]. These processes do not depend on the excitation of a higher-lying state. Bleaching using only 532-nm excitation was observed in rose bengal, as shown in Fig. 4.5. This figure shows the difference in transient transmission between a fresh sample and that same sample after an additional 54 minutes of 532-nm excitation. If a single sample was used for one-step and then two-step excitation, the observed increase in transmission might be mistaken as resulting from T_2 photochemistry. In order to distinguish between the various types of bleaching it is critical that a fresh sample be used for each measurement.

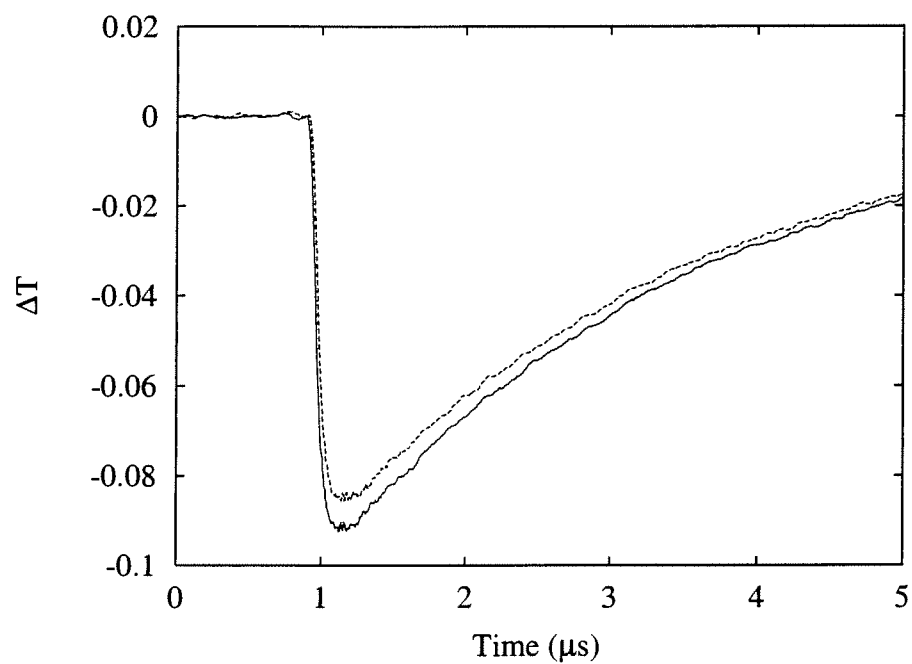


Figure 4.5: Transient transmission at 920 nm induced by 532-nm excitation reveals long-term photobleaching effects. Fresh sample (—); sample after 54 minutes of 532-nm excitation (- - -).

The transient transmission at 920 nm for one-step and two-step excitation is shown in Fig. 4.6. Each curve represents the average from four samples, with the response from each sample reported as the average of 256 consecutive shots. As noted above, the two-step excitation curve cannot show the idealized two-step response sketched in Fig. 3.1 because of the detection system response time.

4.6.3 Analysis and discussion

The transient transmission at 920 nm induced by one-step and two-step excitation are shown again in Fig. 4.7, but this time the curves are overlaid to facilitate comparison. The two curves are essentially indistinguishable, indicating that there is minimal bleaching through either reverse intersystem crossing or radical formation at \mathcal{P}_2 fluences as high as 6.25×10^{16} photons/cm² (11.7 mJ/cm²). For purposes of analysis it is more relevant to examine absorbance since it is linearly-dependent on the concentration of T₁. In order to emphasize the difference between the curves shown in Fig. 4.6, the relative change in absorbance, $\mathcal{R} = (\Delta A_{532+1064} - \Delta A_{532})/\Delta A_{532}$, calculated from these curves is shown in Fig. 4.8 for the time interval labeled 1.2 to 2.0 μ s. The time-averaged value of the relative change in absorbance, $\overline{\mathcal{R}}$, is 0.0004 with a standard deviation $\sigma_{\mathcal{R}} = 0.0019$. A line representing $\overline{\mathcal{R}}$ as well as lines for $\overline{\mathcal{R}} \pm \sigma_{\mathcal{R}}$ are shown in this figure. From Eq. 4.2, the relative change in absorbance resulting from reverse intersystem crossing is -0.0005 for $\Phi_{\text{risc}, T_2} = 0.0076$. Similarly, the bleaching due to radical formation is -0.015 if $\Phi_{\text{chem}, T_2} = 0.004$, the yield found for the 308-nm excited singlet state [99]. Note that N_{abs} was calculated numerically as described above.

A radical formation yield as high as 0.004 can be ruled out since that would result in a relative change in absorbance more than $8\sigma_{\mathcal{R}}$ away from the experi-

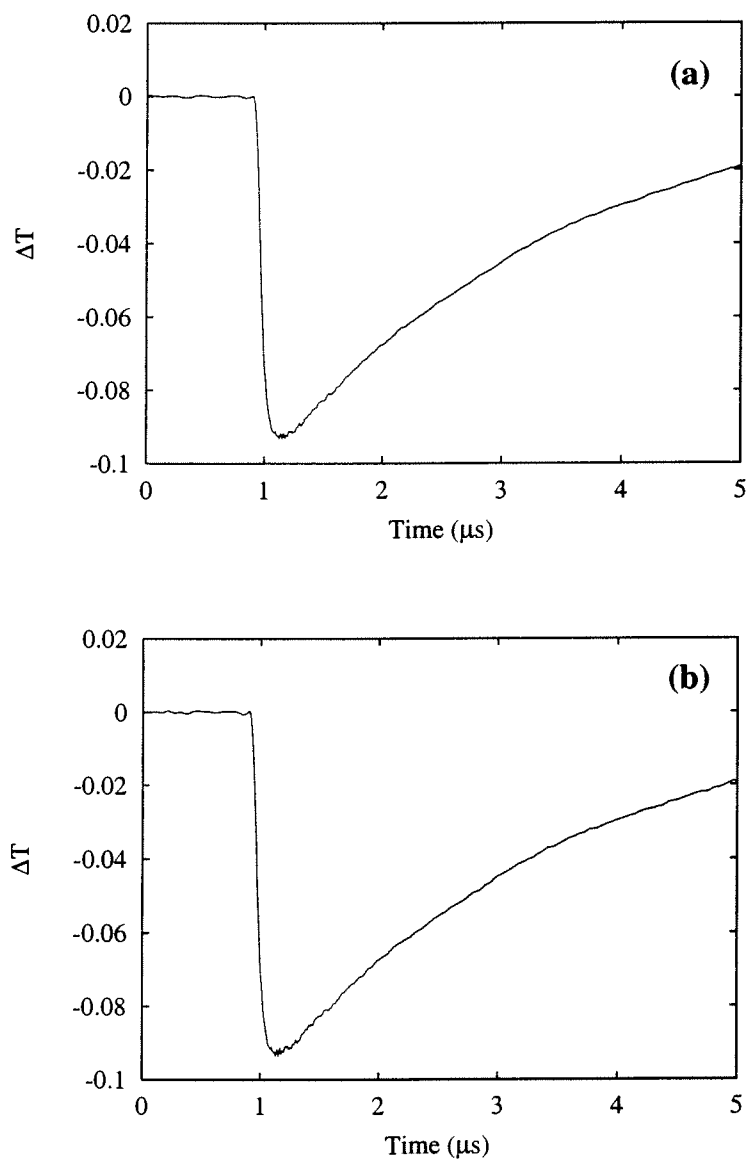


Figure 4.6: Transient transmission at 920 nm induced by one- and two-step excitation. (a) 532-nm excitation only; (b) 532- + 1064-nm excitation. The separation between pulses is 34 ns and the average fluence of the 1064-nm pulse is 6.25×10^{16} photons/cm².

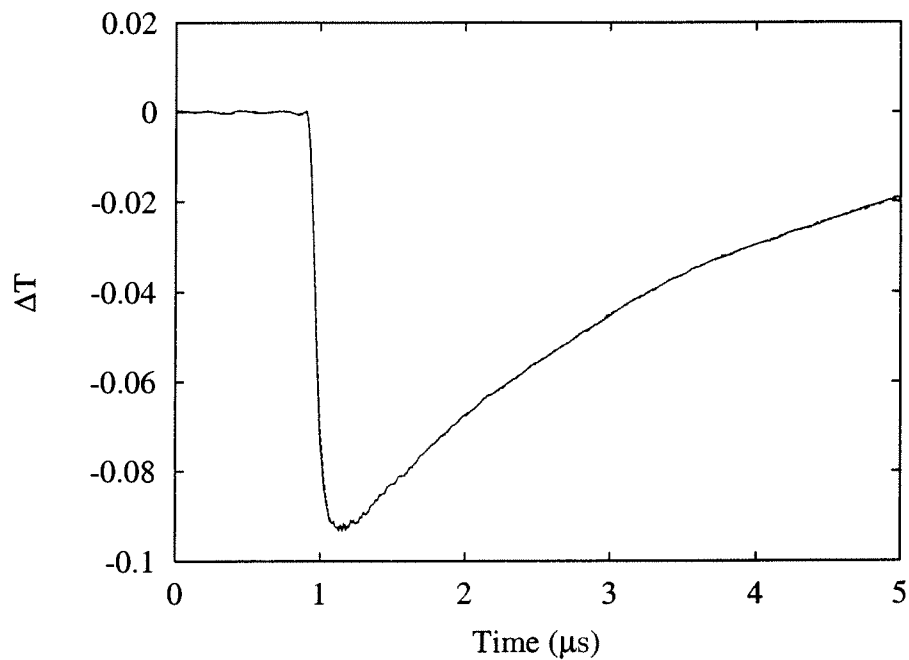


Figure 4.7: Comparison of transient transmission at 920 nm induced by one- and two-step excitation. 532-nm excitation only (—); 532- + 1064-nm excitation (- - -). The separation between pulses is 34 ns and the average fluence of the 1064-nm pulse is 6.25×10^{16} photons/cm². Note that the two curves are virtually indistinguishable.

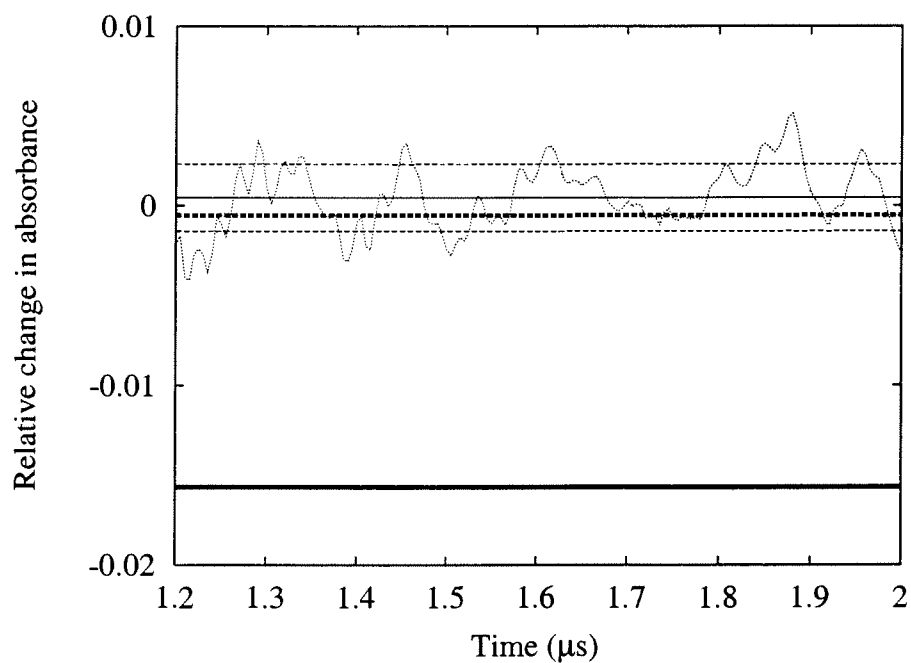


Figure 4.8: Relative change in absorbance, $R = (\Delta A_{532+1064} - \Delta A_{532})/\Delta A_{532}$, at 920 nm induced by two-step excitation. Relative change in absorbance calculated from data in Fig. 4.7 (\cdots); average of experimental data in time interval shown ($-$); average \pm standard deviation of experimental data ($- - -$); theoretical bleaching from $\Phi_{\text{risc},T_2} = 0.0076$ and $\Phi_{\text{chem},T_2} = 0.004$ (---); theoretical bleaching from $\Phi_{\text{risc},T_2} = 0.0076$ (- - -). The separation between pulses is 34 ns and the average fluence of the 1064-nm pulse is 6.25×10^{16} photons/cm².

mentally measured $\overline{\mathcal{R}}$. Using a $2\sigma_{\mathcal{R}}$ confidence interval, the maximum quantum yield of radical formation from T_2 consistent with this data is 0.0008. Therefore Φ_{chem,T_2} is at least a factor of five less than the quantum yield of radical formation reported for the 308-nm excited singlet state [99]. The radical yield from T_3 has not been measured, but has been assumed to be approximately equal to that of the 308-nm excited singlet state [73].

All of the identified higher-lying triplet states of rose bengal have energies exceeding 2.8 eV, as shown in Table 4.3. This energy, 2.8 eV, is the maximum C-I bond energy found in the review of the literature described in §4.5. To our best knowledge, no theoretical calculation of this energy has been completed for rose bengal. Therefore it is plausible that T_2 , with an energy of 2.9 eV estimated from the triplet-triplet absorption spectrum, is not sufficiently energetic to result in C-I bond cleavage. The two states that produce oxygen-independent damage have energies approximately 1 eV greater than this. The lack of radical formation from T_4 can not be explained easily, as it is even more energetic.

4.7 Explanation of photochemical differences based on reverse intersystem crossing

The lack of evidence for oxygen-independent chemistry following 532- + 532-nm excitation of rose bengal was a puzzle which motivated several studies by the group at the Wellman Laboratories, beginning with the work of Fluhler *et al.* [98] in 1989. Oxygen-independent photochemistry had been expected from the state, T_4 , populated by double 532-nm excitation since it was even more energetic than the UV-excited singlet state for which the oxygen-independent effect had first been observed or T_3 , the triplet state populated by 532- + 640-nm excitation [73].

Table 4.3: Energies and radical yields of rose bengal excited states. The energy data, with references, also appears in Table 3.6.

State	Energy (eV)	Ref.	Φ_{chem}	Ref.
S ₁	2.10	Chap. 2	—	—
S ₂	2.41	Chap. 2	—	—
S ₃	3.51	Chap. 2	—	—
S ₄	3.95	Chap. 2	0.0041	[99]
T ₁	1.75	[74]	—	—
T ₂	2.92	Chap. 2	< 0.0008	This chapter
T ₃	3.86	[73]	~ 0.004	[73]
T ₄	4.03	[65]	< 0.0005	[14]

Explanations for a significant chemical yield of radicals despite the low quantum yield for the process had been based on a model requiring multiple excitations of the higher-lying triplet state during each two-pulse sequence. The short lifetime of the higher-lying triplet state would allow for many excitations of this state during the 400 ns pulse used by Smith *et al.* [73]. The observed chemical difference between T_3 and T_4 might therefore be due to a photophysical process which inhibited rapid, multiple excitations of T_4 .

With Reindl and Penzkofer's report of 80% reverse intersystem crossing from T_4 [59], a potentially significant photophysical difference between T_4 and T_3 was identified. Depopulation of the triplet manifold via reverse intersystem crossing would decrease the population repeatedly excited to the higher-lying triplet states, and therefore decrease the total yield of radicals. This possible explanation was presented in our talk given at the 1998 meeting of the American Society for Photobiology [34] and was subsequently adopted as the sole explanation of the different biological observations in an article by Lambert *et al.* [63]. This article did not provide support for the contention that reverse intersystem crossing was the sole factor responsible for the observed differences between T_3 and T_4 .

Through the use of kinetic models it is possible to explore the effects of reverse intersystem crossing on photoproduct formation in a more quantitative fashion. The system of equations describing two pulse excitation, Eq. 3.14, were modified by including the rate of photoproduct formation, $\Phi_{\text{chem},T_n}\tau_{T_n}^{-1}p_{T_n}$, in the dp_{T_n}/dt equation. The total radical production resulting from excitation of T_n is equal to

$$\left\langle \int_0^{+\infty} \Phi_{\text{chem},T_n}\tau_{T_n}^{-1}p_{T_n} dt \right\rangle \quad (4.9)$$

where $p_{T_n}(\theta, t)$ is found from the kinetic model. Photophysical parameters for T_2 are used in this exploration with $F_1 = 1.75 \times 10^{16}$ photons/cm² and $F_2 = 8.00 \times 10^{16}$ photons/cm². Fig. 4.9 shows the results from this model for a fixed photoproduct formation quantum yield ($\Phi_{\text{chem},T_n} = 0.004$) and a variable reverse

intersystem crossing quantum yield, with the radical production being scaled to unity for $\Phi_{\text{risc}} = 0$. The solid curve represents the case in which the $S_1 \rightarrow T_1$ intersystem crossing yield of 0.98 is used in the model, most closely matching the conditions of the experiments described in Chap. 3. In this case reverse intersystem crossing has a relatively small effect on radical production, reducing it by not much more than 10% even at $\Phi_{\text{risc}} = 0.9$. For these relatively long pulses, 400 ns for \mathcal{P}_2 , the reduction of radical production is primarily occurring due to depletion of the excited states by $S_1 \rightarrow S_0$ transitions following reverse intersystem crossing, reducing the population repeatedly excited to the higher-lying states. Much greater differences are seen in radical production as a function of reverse intersystem crossing yield for the cases of decreased $S_1 \rightarrow T_1$ intersystem crossing. As shown in Eq. 4.2, the loss of population from T_1 depends on Φ_{isc} as well as Φ_{risc} . The yield of intersystem crossing is strongly dependent on the local environment. For example, $\Phi_{\text{isc}} = 0.98$ in water but 0.75 in methanol.

Fig. 4.10 shows the dependence of radical formation on reverse intersystem crossing yield for the cases of two different upper-state lifetimes, $\tau_{T_n} = 10$ ps and $\tau_{T_n} = 100$ ps. As demonstrated by the figure, there is little or no dependence on the upper state lifetime for these 400-ns long pulses. For a radical yield of 0.004 and no reverse intersystem crossing, the population of T_1 after n excitations relative to the initial T_1 population is $(0.996)^n$. Therefore, approximately 1725 excitations are required to convert 99.9% of the initial T_1 to photoproducts. This implies that for 400-ns pulses the radical yields should be essentially independent of upper state lifetime for lifetimes of 230 ps or less.

The results of this modeling suggest that it is problematic to attribute the large differences in biological effects solely to differences in reverse intersystem crossing yields. One issue that should be addressed in future work are changes

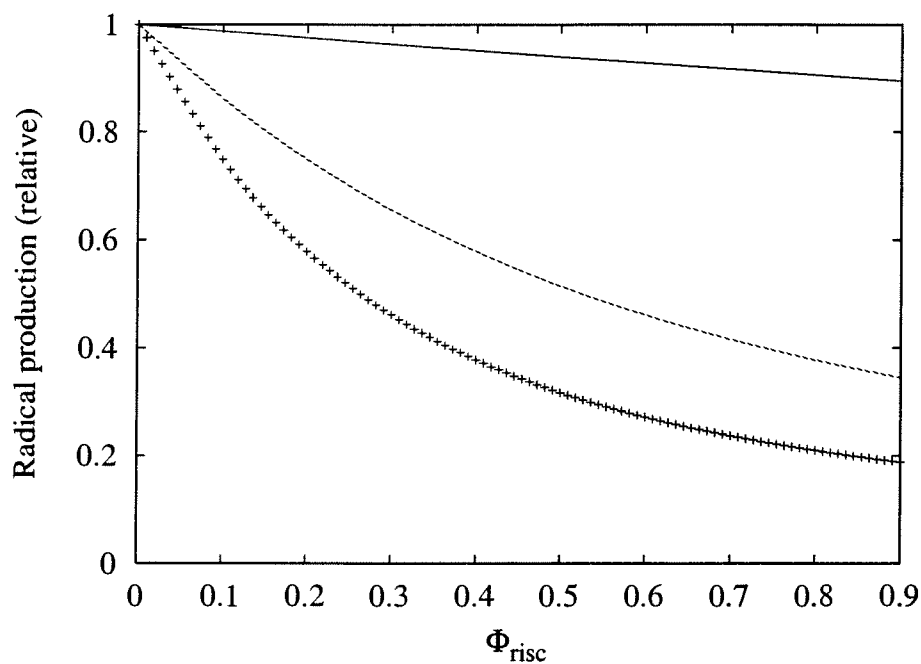


Figure 4.9: Theoretical dependence of radical production on the forward and reverse intersystem crossing yields. Radical production, calculated from the kinetic model developed in Chapters 3 and 4, is dependent on the $S_1 \rightarrow T_1$ and $T_n \rightarrow S_m$ intersystem crossing yields. $\Phi_{\text{isc}} = 0.98$, the intersystem crossing yield for rose bengal in water (—); $\Phi_{\text{isc}} = 0.75$, the intersystem crossing yield for rose bengal in methanol (- - -); $\Phi_{\text{isc}} = 0.50$ (+).

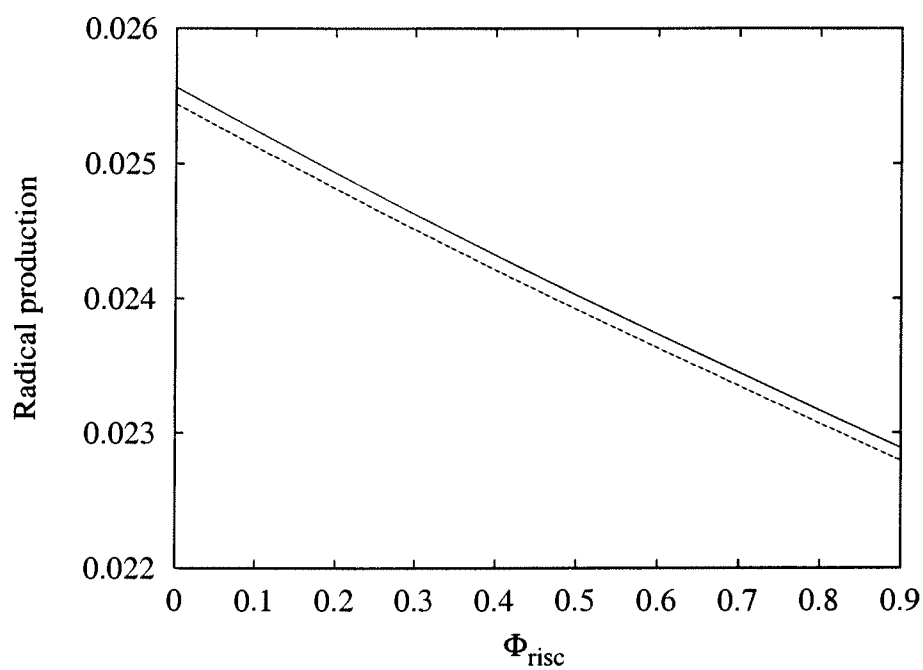


Figure 4.10: Theoretical dependence of radical production on the reverse intersystem crossing yield and upper triplet state lifetime. Radical production is calculated from the kinetic model developed in Chapters 3 and 4. $\tau_{T_n} = 10$ ps (—); $\tau_{T_n} = 100$ ps (- - -).

in the photophysical parameters when rose bengal is no longer in simple solvents, but is instead in the more complex biological media used in the assays for cytotoxicity. Determining photophysical parameters under these conditions poses new challenges, but is an important step in connecting the fundamental properties of the photosensitizer with the biological work.

4.8 Discussion of two-step activation feasibility

Once a photosensitizer has been identified to produce oxygen-independent damage following two-step excitation, is it reasonable to consider its use in therapy? As described in §4.3, there have been claims that therapies based on two-step activation are not feasible. One of the claims was that production of significant population in higher-lying states would require laser pulses with intensities sufficient to cause dielectric breakdown and other unwanted effects [93]. However, this only considered excitation by isolated picosecond pulses. If the goal is to produce significant damage from a unimolecular process occurring from a higher-lying triplet state a more suitable approach is to consider the use of two-step excitation. The high peak intensities required for simultaneous two-photon absorption are not necessary in the case of sequential two-photon absorption because of the presence of a real intermediate state.

A model of two-step activated photodynamic therapy corresponding to Fig. 4.1b will be considered in order to examine the feasibility of this approach. The rate of monomolecular photoproduct formation from a higher-lying triplet state is

$$\frac{dN_{\text{chem}}}{dt} \approx r \Phi_{\text{isc}} \Phi_{\text{chem}, T_n} \sigma_{S_0 S_1} \sigma_{T_1 T_n} F_1 F_2 N \quad (4.10)$$

where r is the repetition rate of two-pulse excitation, Φ_{chem, T_n} is the yield of the monomolecular process leading to reactive photoproducts, and N is the number

of photosensitizer molecules in the excitation volume. The hypothetical photosensitizer is assumed to have strong ground state absorption in the near-infrared ($\sigma_{S_0S_1} = 3 \times 10^{-16} \text{ cm}^2$ at $\lambda = 800 \text{ nm}$) and strong triplet-triplet absorption in the red ($\sigma_{T_1T_n} = 3 \times 10^{-16} \text{ cm}^2$ at $\lambda = 630 \text{ nm}$). In addition, intersystem crossing and photoproduct formation yields comparable to those found in rose bengal are adopted ($\Phi_{isc} = 0.98$ and $\Phi_{chem,T_n} = 0.004$).

Several factors influence the choice of excitation parameters for the two pulses, \mathcal{P}_1 and \mathcal{P}_2 . First, the average power must be kept below approximately 200 mW/cm^2 in order to avoid thermal effects. Second, unwanted multiphoton absorption effects can be minimized by keeping the peak power below 1 MW/cm^2 . Finally, the length of \mathcal{P}_1 should be comparable to the S_1 lifetime and \mathcal{P}_2 less than the T_1 lifetime. On the basis of these guidelines, average powers for \mathcal{P}_1 of 50 mW/cm^2 and \mathcal{P}_2 of 100 mW/cm^2 with a pulse repetition rate of 100 Hz are selected. The corresponding photon fluences at 800 nm and 630 nm are 2×10^{15} and $3.2 \times 10^{15} \text{ photons/cm}^2$. Pulse lengths of 5 ns and 100 ns for \mathcal{P}_1 and \mathcal{P}_2 are reasonable choices for efficient excitation. These pulse lengths result in peak intensities of approximately 100 kW/cm^2 and 10 kW/cm^2 for \mathcal{P}_1 and \mathcal{P}_2 respectively. Using these parameters in Eq. (4.10), the rate of photoproduct formation is found to be $0.23N \text{ s}^{-1}$. For comparison, conventional photodynamic therapy produces singlet oxygen at a rate

$$\frac{dN_{oxy}}{dt} \approx \Phi_{isc} \Phi_{\Delta} \sigma_{S_0S_1} F_1 N , \quad (4.11)$$

where Φ_{Δ} is the yield of triplet quenching by oxygen. Assuming excitation of 50 mW/cm^2 at 630 nm with the absorption cross sections used above results in a singlet oxygen production rate of $35N \text{ s}^{-1}$ if $\Phi_{\Delta} = 0.75$. The photoproducts generated from a higher-lying state may have a different potential for causing cellular damage compared to singlet oxygen. For example, the radicals created following

excitation of the higher-lying states of rose bengal have been found to be roughly 180 times more damaging than singlet oxygen [99]. Assuming the same toxicity for photoproducts generated by the hypothetical photosensitizer under consideration, it is found that a photoproduct formation rate of $0.23N \text{ s}^{-1}$ is equivalent to a singlet oxygen generation rate of $41N \text{ s}^{-1}$. Thus it seems plausible that a two-step activated photosensitizer could produce damage at a rate comparable to a conventional photosensitizer.

In the typical idealized model of conventional photodynamic therapy there is no bleaching of the photosensitizer. In actuality, photobleaching can be a significant effect. For Photofrin[®] photobleaching occurs as a result of reactions between singlet oxygen and the photosensitizer [110]. The fraction of generated singlet oxygen reacting with the photosensitizer is given by

$$\Phi_{\text{bleach}} \approx \frac{k_{\text{os}}[\text{S}_0]}{k_{\text{oa}}[\text{A}]} \quad (4.12)$$

where k_{os} is the bimolecular rate constant for singlet oxygen reactions with ground-state photosensitizer, k_{oa} is the bimolecular rate constant for singlet oxygen reactions with cellular substrates, and $[\text{A}]$ is the concentration of cellular substrates. In Eq. (4.12) the term $k_{\text{os}}[\text{S}_0]$ has been dropped from the denominator since it is assumed to be a much smaller rate than that of reactions between singlet oxygen and other targets. From this photobleaching yield it can be estimated that the photosensitizer will produce approximately $1/\Phi_{\text{bleach}}$ singlet oxygens before undergoing bleaching. From their experiments with Photofrin-sensitized EMT6 spheroids Georgakoudi *et al.* determined that $k_{\text{os}}/k_{\text{oa}}[\text{A}] = 76 \text{ M}^{-1}$. Therefore each photosensitizer can produce roughly 700 singlet oxygens before bleaching, assuming a ground-state sensitizer concentration of $20 \mu\text{M}$.

Photoproduct formation from a higher-lying state is generally assumed to be destructive if it is a monomolecular process such as the radical formation observed

in rose bengal. In this case each sensitizer can produce only one photoproduct. Assuming the same enhanced toxicity as above, this is equivalent to 180 singlet oxygens per two-step-activated sensitizer. On the basis of this analysis of a hypothetical sensitizer, the maximum possible dose from two-step activated photodynamic therapy is roughly four times less than that of conventional photodynamic therapy.

Oxygen-dependent selection between singlet oxygen-mediated and radical-mediated photodynamic therapy is possible with a double-pulse excitation scheme. Radical formation via bond cleavage directly results in the bleaching of the photosensitizer whereas the energy transfer from the dye to molecular oxygen returns the photosensitizer to its ground state, allowing it to undergo the photodynamic energy transfer cycle repeatedly. This suggests that the singlet oxygen-mediated process is preferable in regions of adequate oxygenation. However, regions of hypoxia are also to be expected. In those areas singlet oxygen-mediated therapy will not proceed and the radical-mediated process becomes desirable. A double-pulse excitation scheme can be devised that will switch between these two mechanisms depending on the local oxygen concentration.

The first pulse is intended to excite the ground state sensitizer, and its wavelength should be chosen to maximize this transition. Following intersystem crossing, the excited photosensitizer molecules will be in the T_1 state. The primary routes for T_1 relaxation are the energy transfer process to molecular oxygen, phosphorescence, and intersystem crossing to S_0 . In the case of rose bengal, the lifetime of T_1 in the absence of quenchers has been reported to be 150 ms and the bimolecular rate constant for oxygen quenching is $k_{\Delta} + k_{SO} = 1.6 \times 10^9 \text{ M}^{-1}\text{s}^{-1}$ [66]. Quenching by oxygen produces $^1\text{O}_2(\Delta_g)$ at the rate $k_{\Delta}[^3\text{O}_2]$ and the superoxide anion radical, $\text{O}_2^{\cdot-}$, at the rate $k_{SO}[^3\text{O}_2]$. The ratio of these two rates is sensitive to

the local environment. The experiments of Lambert and Kochevar indicate that the singlet oxygen process predominates in biological environments [101]. Therefore we will assume that $k_{\Delta} \approx 1.6 \times 10^9 \text{ M}^{-1}\text{s}^{-1}$. At oxygen concentrations of $120 \mu\text{M}$ the resulting T_1 lifetime is

$$\frac{1}{(1.6 \times 10^9 \text{ M}^{-1}\text{s}^{-1})(120 \mu\text{M}) + (150 \text{ ms})^{-1}} = 5.2 \mu\text{s} \quad (4.13)$$

and at $10 \mu\text{M}$ oxygen the lifetime is $62 \mu\text{s}$. This difference in triplet lifetimes is the basis for the oxygen-dependent selection between singlet oxygen-mediated and radical-mediated damage.

The wavelength of the second pulse is chosen to effectively excite a higher-lying triplet state that will undergo bond cleavage and thus produce oxygen-independent damage. The higher-lying triplet state will only be excited if the second pulse arrives while T_1 is still populated. If the second pulse is delayed relative to the first pulse by a time that exceeds several lifetimes of T_1 in conditions of abundant oxygen then the desired switching between the two damage mechanisms can occur. For example, if the second pulse is delayed by $20 \mu\text{s}$ then about 98% of the molecules originally excited to T_1 in an environment with $120 \mu\text{M}$ oxygen will have been quenched by oxygen before the second pulse arrives, leaving only 2% to be excited to a higher-lying state. On the other hand, only 28% of the T_1 molecules will have been quenched by oxygen in $20 \mu\text{s}$ if the environment contains $10 \mu\text{M}$ oxygen, leaving 72% to be excited by the second pulse to a higher-lying triplet state. With this double-pulse configuration the singlet oxygen-mediated process will dominate in regions of a tumor that are highly oxygenated, but the radical-mediated process will play a more significant role in those regions where the availability of oxygen is limited.

4.9 Conclusion

Our two-step laser-induced bleaching experiments on the T_2 state of rose bengal have found essentially no difference between one- and two-step excitation. On the basis of this data it is concluded that there is little or no yield of radicals, $\Phi_{\text{chem},T_2} < 0.0008$, from the T_2 state of rose bengal. This also suggests that the energy required for the cleavage of the C-I bond in rose bengal in water is greater than 2.9 eV.

An explanation of the lack of oxygen-independent photochemistry from the T_4 state of rose bengal based on a high reverse intersystem crossing yield has been examined quantitatively. Results from a kinetic model suggest that reverse intersystem crossing accounts for a minor portion of the observed differences in biological effects between this state and T_3 . It is also shown that the effect becomes greater as $S_1 \rightarrow T_1$ intersystem crossing becomes less probable. A full explanation of the biological results requires that the relevant photophysical parameters for rose bengal be determined in the biological environment.

The feasibility of two-step activation in a therapeutic context is considered. Reasonable parameters for the two excitation pulses are estimated to produce the same damage, within an order of magnitude, as conventional singlet oxygen-mediated therapy. A scheme for oxygen-dependent selection between radical-mediated and singlet oxygen-mediated damage is proposed. This excitation scheme favors conventional PDT under conditions of abundant oxygen, but in hypoxic regions it would produce radical-mediated damage. The results of this idealized model suggest that further experimental study of oxygen-independent chemistry from higher-lying states in rose bengal and other photosensitizers is warranted and could potentially result in a modified form of photodynamic therapy better able to treat hypoxic regions.

Chapter 5

Simultaneous multiphoton absorption and the effects of higher-lying states

Molecular transitions requiring the simultaneous absorption of two or more photons can now be excited routinely by using pulsed lasers. However, the desired transition may not be the only one excited, especially if the pulses occur at a high repetition rate. Under these circumstances higher-lying states can begin to play a role in the resulting molecular behavior. This chapter examines multiphoton excitation and the effect that higher-lying states can have on the resulting fluorescence. The process of reverse intersystem crossing will be shown to have a significant impact on a common method of determining the two-photon absorption cross section.

5.1 Background

At naturally occurring light intensities, radiative transitions involve the absorption or emission of a single photon. The existence of radiative transitions involving the simultaneous absorption of two photons was predicted by Maria Göppert-Mayer [111] in her dissertation published in 1931. This process does not require a real intermediate state and is therefore different from the sequential absorption of two photons. However, it can be helpful to think of simultaneous two-photon absorption as occurring via a virtual intermediate state, as indicated by the dashed line in Fig. 5.1.

According to the Heisenberg uncertainty relation $\Delta E \Delta t \geq \hbar$, the energy of a state is not well-defined if it is occupied for only a short time. The inclusion of a virtual state in a model of two-photon absorption is a way of recognizing that an electron can be briefly excited to an energy that is not allowed in the long-time description of the system. The virtual state can be thought of as a superposition of states rather than a single eigenstate. This concept of a virtual intermediate state also allows for a more precise definition of “simultaneous” absorption. Using the energy-time uncertainty relation, a lifetime of

$$\tau_v < \frac{\hbar}{\Delta E} \quad (5.1)$$

can be assigned to the virtual state, where ΔE is the energy gap between the virtual state and the nearest real state. Therefore, simultaneous two-photon absorption requires that both photons be absorbed within a time τ_v . For example, if $\Delta E = 1.2$ eV then $\tau_v \approx 0.6$ fs.

The virtual state model can also be used to predict \mathcal{R} , the rate of two-photon excitation. The probability of exciting the virtual state in a time τ_v is approximately $\sigma_{iv} I \tau_v$, where σ_{iv} is the one-photon $i \rightarrow v$ absorption cross section

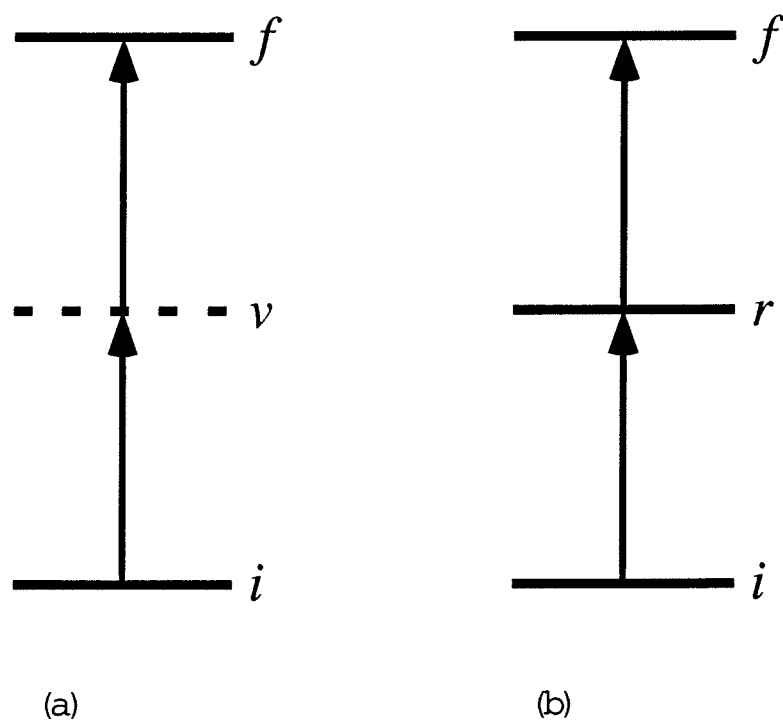


Figure 5.1: Models of (a) simultaneous and (b) sequential two-photon absorption. Initial and final states are denoted by i and f , respectively. Virtual and real intermediate states are denoted by v and r , respectively.

and I is the intensity of the light. The excitation rate of the final state from the virtual state is given by $\sigma_{vf}I$ where σ_{vf} is the one-photon $v \rightarrow f$ absorption cross section. Therefore,

$$\mathcal{R} \approx (\sigma_{iv}I\tau_v)(\sigma_{vf}I) = (\sigma_{iv}\sigma_{vf}\tau_v)I^2 \quad (5.2)$$

which is of the same form as $\mathcal{R} = \delta I^2$, a more conventional expression for the rate of two-photon excitation in terms of the two-photon absorption cross section δ . This interpretation of δ is not universally accepted. A review of the literature shows many workers in the field have identified δI^2 as the rate of molecular excitation [112–116]. Others have identified δI^2 as the rate of photon absorption [117–119], and therefore the rate of molecular excitation is given by $\frac{1}{2}\delta I^2$. The existence of these two different interpretations for the same symbol does not appear to be openly recognized and may account for some of the disagreement over the two-photon absorption cross section for various molecules found in the literature. The two-photon absorption cross section δ in this chapter will be based on the molecular excitation-rate interpretation.

On the basis of these equations it is found that δ is approximately equal to $\sigma_{iv}\sigma_{vf}\tau_v$. A rough estimate of $\delta \approx 10^{-49} \text{ cm}^4 \cdot \text{s}$ can be made by adopting the reasonable assumptions that $\sigma_{iv} \approx \sigma_{vf} \approx 10^{-17} \text{ cm}^2$ and $\tau_v \approx 10^{-15} \text{ s}$. Two-photon absorption cross sections are also commonly given in terms of the göppert-mayer (GM), where $1 \text{ GM} \equiv 10^{-50} \text{ cm}^4 \cdot \text{s}$. In terms of this new unit, the predicted two-photon absorption cross section is 10 GM. Reference [120] contains this estimate as well as similar ones for higher-order multi-photon absorption cross sections. Although resulting from an extremely idealized model, this cross section is within an order of magnitude of those found experimentally. For example, $\delta = 210 \pm 55 \text{ GM}$ for 840-nm excitation of Rhodamine B, $\delta = 38 \pm 9.7 \text{ GM}$ for 782-nm excitation of fluorescein, and $\delta = 12 \pm 4$ for 700-nm excitation of Indo-1 [118]. The rate of

sequential two-photon absorption is expected to be as much as 10^6 times greater because the lifetime of the real intermediate state is nanoseconds rather than the sub-femtosecond lifetime of the virtual state.

Another difference between one- and two-photon absorption can easily be seen using this model. For one-photon absorption, the transition matrix element was proportional to $\langle\psi_f|\mathbf{er}|\psi_i\rangle$. This led to the Laporte selection rule for centrosymmetric molecules that only allowed one-photon transitions between states of different parity ($g\rightarrow u$ and $u\rightarrow g$). The transition matrix element for two-photon absorption is proportional to $\langle\psi_f|\mathbf{er}|\psi_v\rangle\langle\psi_v|\mathbf{er}|\psi_i\rangle$. Therefore allowed two-photon transitions occur between states of the same parity ($g\rightarrow g$ and $u\rightarrow u$).

5.2 Fluorescence technique for determining the two-photon absorption cross section

Although predicted theoretically in 1931, two-photon excitation was not observed until 1961. The intensity of light required for efficient two-photon excitation required the development of a new light source, the laser. Using a ruby laser to excite a $\text{CaF}_2:\text{Eu}^{2+}$ crystal, Kaiser and Garrett [121] were the first to observe fluorescence resulting from two-photon excitation. Numerous articles reporting on various aspects of multiphoton absorption have appeared since that time. The interested reader might begin with the review articles Refs. [113, 122, 123].

Two-photon excited fluorescence has become one of the accepted methods for measuring relative two-photon absorption cross sections [118]. The measured fluorescence rate, $F(t)$, in the excitation volume is proportional to \mathcal{R} such that

$$F(t) = \int \alpha \Phi_f C \delta I^2 dV \quad (5.3)$$

where α is the fluorescence collection efficiency, Φ_f is the fluorescence quantum

yield, and C is the dye concentration. Note that this expression differs by a factor of two from that found in Ref. [118] because that article uses the photon absorption-rate definition of δ . It is often possible to separate the light intensity $I(\mathbf{r}, t)$ into a spatial and temporal distribution such that $I(\mathbf{r}, t) = S(\mathbf{r})I_0(t)$. If this is the case, most of the parameters can be removed from the spatial integral giving

$$F(t) = \Phi_f C \delta \alpha I_0^2(t) \int S^2(\mathbf{r}) dV . \quad (5.4)$$

Calculation of \mathcal{F} , the total fluorescence collected following an excitation pulse, is found by taking the temporal integral such that

$$\mathcal{F} = \Phi_f C \delta \alpha \left(\int I_0^2(t) dt \right) \left(\int S^2(\mathbf{r}) dV \right) . \quad (5.5)$$

The unknown two-photon absorption cross section of a dye can be determined by using the same experimental system to measure the fluorescence of both that molecule and a reference dye. By calculating the ratio, the instrumental parameters α , $\int I_0^2(t) dt$, and $\int S^2(\mathbf{r}) dV$ can be eliminated. Therefore

$$\delta_u = \frac{\mathcal{F}_u}{\mathcal{F}_r} \left(\frac{C_r \Phi_{f,r}}{C_u \Phi_{f,u}} \right) \delta_r \quad (5.6)$$

where the properties of the dye with the unknown cross section are labeled by u and the reference by r .

5.3 Intensity-squared dependence of two-photon excited fluorescence

On the basis of the theory described above, one might expect that two-photon-excited fluorescence would depend quadratically on the excitation intensity. This is indeed the case for single pulses with moderate excitation intensity. When

these conditions are not satisfied several complicating processes can result in deviations from the expected quadratic behavior. Restricting a review of the literature to only xanthene dyes, it is found that numerous groups have reported a less-than-quadratic behavior in what they described as two-photon excited-fluorescence [115, 124–126]. These studies were conducted with excitation pulses lasting nanoseconds (Hermann and Ducuing, Ref. [125]), picoseconds (Bradley *et al.*, Ref. [115]), and femtoseconds (Fischer *et al.*, Ref. [126]).

Fischer *et al.* [126] studied two-photon excited fluorescence for dyes from the coumarin and xanthene families excited by 80 to 130-fs pulses from a titanium-sapphire laser which could be tuned from 750 to 850 nm. The coumarin dyes Coumarin 1, 120, and 151 followed the expected intensity square law but the xanthene dyes fluorescein, Rhodamine 6G (Rh6G), and Rhodamine B (RhB) were better fit by a power law of 1.4 (fluorescein) or 1.8 (the Rhodamines) for excitation fluxes between 8×10^{26} and 3×10^{28} photons $\text{cm}^{-2} \text{s}^{-1}$. Fischer *et al.* proposed that this behavior could be explained by a model that included excited-state absorption, as shown in Fig. 5.2a. Population excited to the high-lying state, S_n , was assumed to not return to any of the lower-lying states. Lacking from this model is any justification for this unusual assumption. The conventional assumption (Kasha's rule) is that any such high-lying state will relax rapidly to a lower-lying singlet state, with little or no loss. The evidence supporting the Fischer model is that it produces a less than quadratic behavior, though it could still be argued that the model fails to convincingly agree with their data (see Fig. 4 in Ref. [126]).

If one chooses to pursue the Fischer *et al.* model further it is necessary to propose a loss mechanism from S_n that prevents internal conversion to S_1 with unity yield. Although fluorescence quantum yields are often assumed to be wavelength-

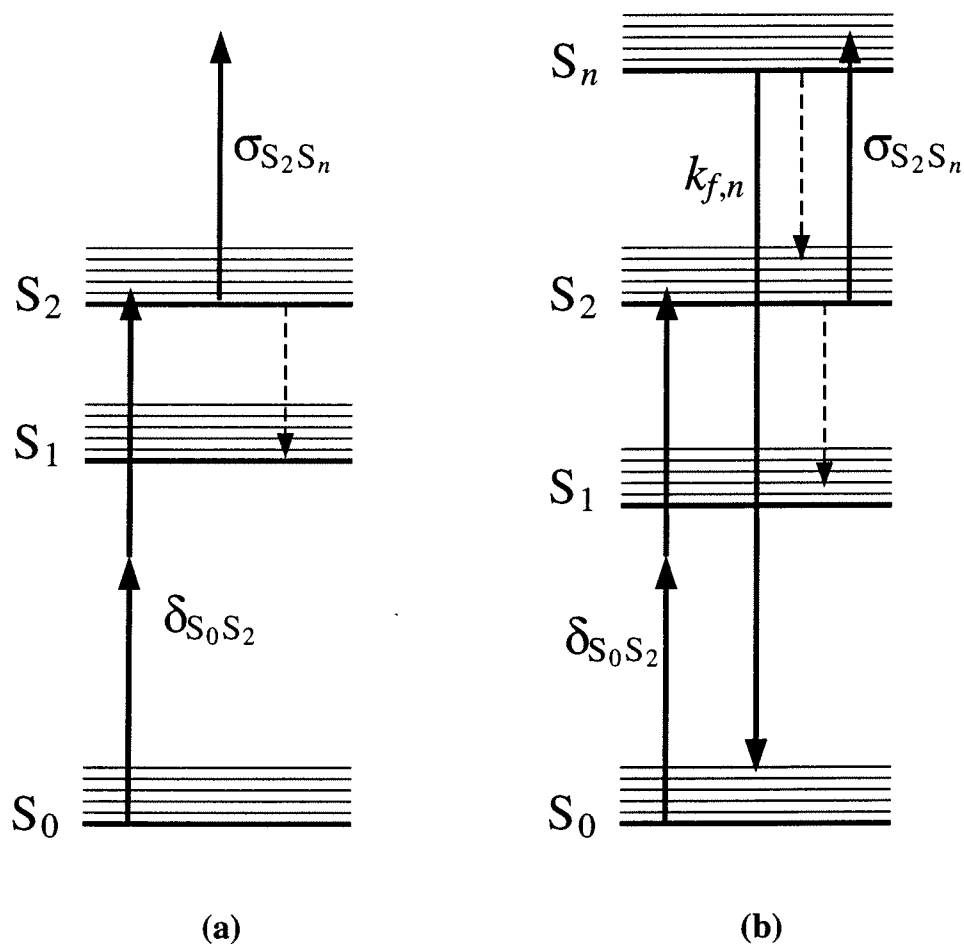


Figure 5.2: Models of two-photon excited fluorescence quenching via excited-state absorption. (a) Fischer model with unspecified loss process following S_n excitation and (b) model with $S_n \rightarrow S_0$ fluorescence. Interval conversion and vibrational relaxation are shown using dashed (- -) lines. The $S_n \rightarrow S_0$ fluorescence rate is given by $k_{f,n}$.

independent (Vavilov's rule), in practice this is not always the case. In particular, it is possible for higher-lying singlet states to have a direct transition to the ground state, possibly emitting light at a shorter wavelength than the expected $S_1 \rightarrow S_0$ fluorescence, as shown in Fig 5.2b. This process was measured previously by Falkenstein *et al.* [127] for Rh6G and RhB. In their study two photons of 530-nm light were sequentially absorbed to populate a higher-lying singlet state. This is energetically similar to the 2+1 photon absorption of near-infrared light described by the excited-state absorption model. Falkenstein *et al.* determined that 30% of the high-lying singlets returned directly to the ground state in the case of Rhodamine B, and 5% in the case of Rhodamine 6G. Fluorescence from S_n would reduce the yield of internal conversion to S_1 , but would not totally eliminate it as proposed in the Fischer model. The excited state absorption cross sections originally determined using this model can be adjusted to account for the non-unity loss process such that $\sigma_{S_2S_n} = 3.4 \times 10^{-15} \text{ cm}^2$ for Rh6G and $1.7 \times 10^{-15} \text{ cm}^2$ for RhB.

It should be noted that femtosecond two-photon excited fluorescence experiments have also been conducted by Watt Webb's group [118,128] under conditions similar to those reported by Fischer *et al.* and the xanthene dyes fluorescein, Rhodamine 6G, and Rhodamine B were found to follow a quadratic dependence to within 4%. However, as will be shown below, a quadratic dependence does not necessarily imply that higher-lying states do not affect the fluorescence signal.

5.4 Two-photon excited fluorescence and reverse intersystem crossing in rose bengal

Two-photon excitation of dyes with pulses lasting longer than the S_1 lifetime provides an opportunity for triplet-triplet one-photon absorption to occur during the latter part of the pulse. Triplet-triplet absorption may even occur with ultrashort pulsed excitation if the pulse repetition rate exceeds approximately 1 MHz. In that case population excited to the triplet state by the previous pulse has not fully relaxed back to the ground state before the arrival of the current pulse. Repopulation of S_1 may occur if reverse intersystem crossing can occur from the higher-lying triplet excited in this secondary process. This repopulation of S_1 will produce fluorescence in addition to that produced by the primary process of two-photon absorption. This enhancement of the fluorescence, if not properly interpreted, could lead to miscalculations of the two-photon absorption cross section.

Two-photon excitation experiments were performed with rose bengal in order to determine the magnitude of error in two-photon absorption cross sections that could result if the process of reverse intersystem crossing is not properly included in the analysis. The selected reference dye was Rhodamine 6G. This dye has been the subject of several studies of two-photon excitation.

5.4.1 Experimental methods and results

The setup for the two-photon excited fluorescence experiments is shown in Fig. 5.3. The 1064-nm light is the final output of the laser system described in §2.1.1. A fraction of this pulse is diverted by a glass plate to a photodiode, allowing the energy in each pulse to be monitored. The remainder of the beam is down-

collimated using lenses L1 and L2 and then passed through pinhole P to produce a beam of diameter 0.49 mm in the sample cuvette. Fluorescence is collected by lens L3 and directed into the PMT by lens L4. Scattered 1064-nm light is removed by placing filter F (Schott, KG3) before the photomultiplier tube. The fluorescence signal and energy monitor are time-gated and averaged using a gated integrator (Stanford Research Systems, 250), digitized (Stanford Research Systems, 240), and transferred to a computer via GPIB (general purpose interface bus).

The 0.49 mm beam diameter in the dye was measured by removing the cuvette and placing a CCD camera (Panasonic GP-MF602) at the same location. The CCD camera is very sensitive so the beam was highly attenuated using neutral density filters prior to lens L1. The combination of camera and frame grabber produced a final resolution of approximately 15 μm per pixel.

Two-photon-excited fluorescence was measured in a 12 μM sample of rose bengal in phosphate-buffered saline (pH 7) and in a 57.5 μM sample of Rhodamine 6G in ethanol. The results of those measurements are shown in Fig. 5.4. The slope of the best fit line on a log-log graph determines the exponent n in a power law model, $f \propto F^n$, of the dependence of the fluorescence f on excitation fluence F . The rose bengal fluorescence data exhibited saturation effects at the highest fluences used in this experiment and only the portion of the data following a power-law behavior has been used in the analysis appearing in this chapter. The portion of the rose bengal data selected for analysis is fit by $n = 2.19$ and the Rhodamine 6G fluorescence is fit by $n = 2.05$. Both of these results confirm the two-photon nature of the primary excitation process.

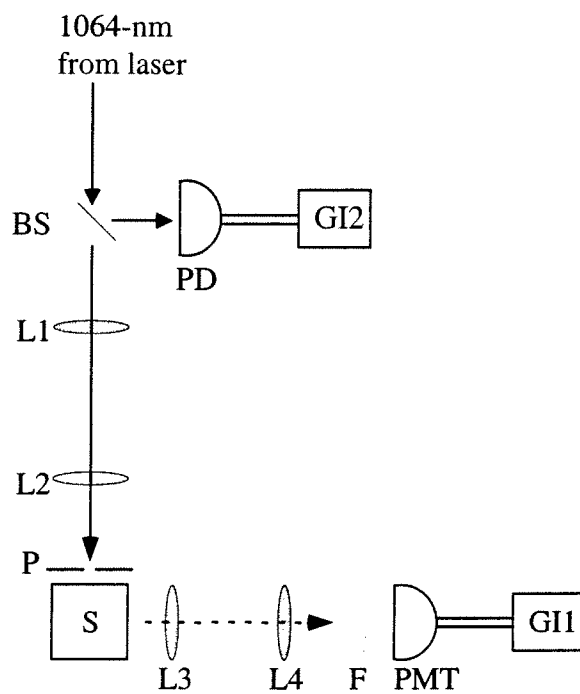


Figure 5.3: Experimental setup for two-photon excited fluorescence measurements. BS, glass plate beam splitter; L1-L4, lenses; P, pinhole; S, quartz cuvette; F, KG3 short-pass filter; PMT, photomultiplier tube; PD, silicon photodiode; GI1 and GI2, gated integrators.

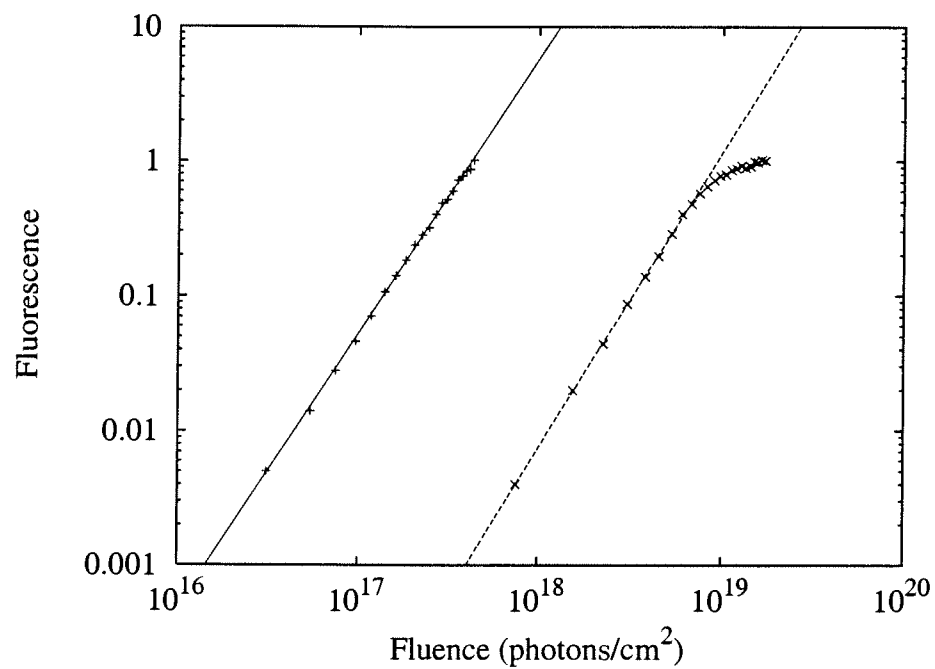


Figure 5.4: Two-photon excited fluorescence of rose bengal (\times) and Rhodamine 6G ($+$) excited by 1064-nm light. The best-fit power law is 2.19 for rose bengal (- - -) and 2.05 for Rhodamine 6G (—).

5.4.2 Analysis

The kinetic model introduced in previous chapters was modified such that the $S_0 \rightarrow S_1$ transition resulted from two-photon absorption rather than a one-photon process. In order to account properly for photoselection effects, the two-photon absorption term must also include a factor of $5 \cos^4 \theta$ rather than the factor of $3 \cos^2 \theta$ associated with one-photon absorption. The rate equations describing the model are

$$\begin{aligned}
 \frac{dp_{S_0}(\theta, t)}{dt} &= -5 \cos^4 \theta (p_{S_0} - p_{S'_1}) \delta I^2(t) + (1 - \Phi_{isc}) \tau_{S_1}^{-1} p_{S_1} + \tau_{T_1}^{-1} p_{T_1} \\
 &\quad - k_{rot}(p_{S_0} - \langle p_{S_0} \rangle) \\
 \\
 \frac{dp_{T_1}(\theta, t)}{dt} &= \Phi_{isc} \tau_{S_1}^{-1} p_{S_1} - \tau_{T_1}^{-1} p_{T_1} - 3 \cos^2 \theta \sigma_{T_1, T_2} (p_{T_1} - p_{T_2}) I(t) \\
 &\quad + (1 - \Phi_{risc, T_2}) \tau_{T_2}^{-1} p_{T_2} - k_{rot}(p_{T_1} - \langle p_{T_1} \rangle) \\
 \\
 \frac{dp_{S_1}(\theta, t)}{dt} &= k_r p_{S'_1} - \tau_{S_1}^{-1} p_{S_1} - k_{rot}(p_{S_1} - \langle p_{S_1} \rangle) \tag{5.7} \\
 \\
 \frac{dp_{S'_1}(\theta, t)}{dt} &= 5 \cos^4 \theta (p_{S_0} - p_{S'_1}) \delta I^2(t) - k_r p_{S'_1} + \Phi_{risc, T_2} \tau_{T_2}^{-1} p_{T_2} \\
 &\quad - k_{rot}(p_{S'_1} - \langle p_{S'_1} \rangle) \\
 \\
 \frac{dp_{T_2}(\theta, t)}{dt} &= 3 \cos^2 \theta \sigma_{T_1, T_2} (p_{T_1} - p_{T_2}) I(t) - \tau_{T_2}^{-1} p_{T_2} - k_{rot}(p_{T_2} - \langle p_{T_2} \rangle) ,
 \end{aligned}$$

where the p_i are the orientational subpopulations of S_0 , T_1 , S_1 , S'_1 , and T_2 . The orientational average of this model is shown in Fig. 5.5. The relevant photophysical parameters for rose bengal and Rhodamine 6G are in Tables 5.1 and 5.2, respectively. The rotation rate and T_1 lifetime of Rhodamine 6G were assumed to be equal to that of rose bengal. This model was first used to calculate the fluence-

dependent fluorescence signal for Rhodamine 6G. The results of this modeling were used to calculate the instrumental response parameter. This instrumental response parameter was then factored out of the rose bengal fluorescence data, allowing this data to be fit using the above model with the rose bengal two-photon absorption cross section being the only free parameter.

The goodness of fit, χ^2 , for various δ is shown in Fig. 5.6 where all data points were weighted equally and

$$\chi^2 = \frac{1}{N} \sum_F (f_{\text{expt}}(F) - \alpha f_{\text{model}}(F; \delta))^2 . \quad (5.8)$$

The scaling parameter α was determined from a fit of the Rhodamine 6G data shown in Fig. 5.4 using the model described above with the known Rhodamine 6G photophysical parameters. The relevance of reverse intersystem crossing is demonstrated by including the results for a model which neglects this process and a model which includes an erroneously high reverse intersystem crossing yield ($\Phi_{\text{risc},T_2} = 0.12$). Using the reverse intersystem crossing yield found in Chap. 3, $\Phi_{\text{risc},T_2} = 0.0076$, we find that the best fit occurs when $\delta = 0.028 \pm 0.001$ GM, as shown in Fig. 5.6. A fit based on a model which neglects reverse intersystem crossing suggests that $\delta = 0.036 \pm 0.001$ GM. This 28% difference between the two cross sections resulted from only a 0.0076 reverse intersystem crossing yield. Fig. 5.6 also shows the case of a larger reverse intersystem crossing yield, $\Phi_{\text{risc},T_2} = 0.12$. Using that value in the model gives $\delta = 0.012 \pm 0.001$ GM, less than half the two-photon absorption cross section determined using the reverse intersystem crossing yield determined for this state in Chap. 3. It is expected that the discrepancy in two-photon absorption cross sections would be even greater for larger errors in the reverse intersystem crossing yield.

The best fit curves for $\Phi_{\text{risc},T_2} = 0.0076$ and $\Phi_{\text{risc},T_2} = 0$ are shown in Fig. 5.7. Quadratic behavior is seen with or without reverse intersystem crossing. These

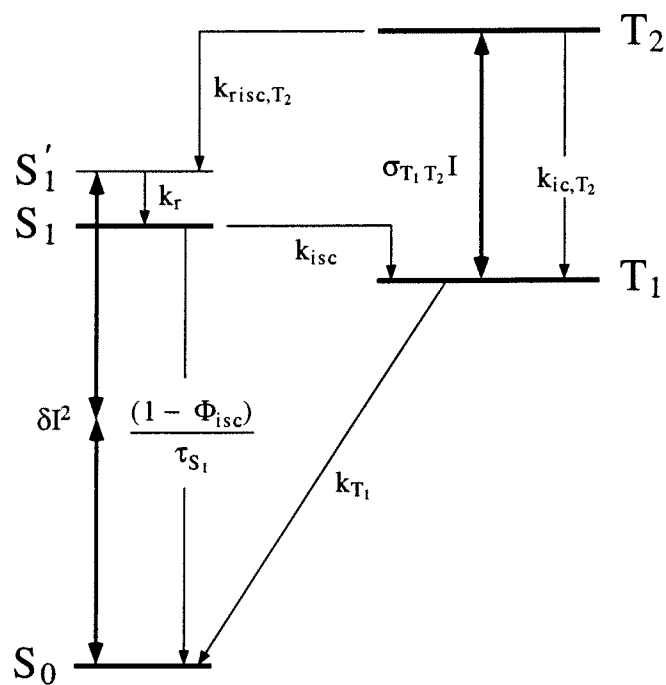


Figure 5.5: Energy-level scheme for 1064-nm multiphoton excitation dynamics. This diagram corresponds to an orientational average of the kinetics described by Eq. (5.7). See Tables 5.1 and 5.2 for parameter descriptions and values.

Table 5.1: Photophysical parameters of rose bengal in water that are relevant to 1064-nm excitation. Parameters to be determined in the fitting process are indicated by t. b. d.

Symbol	Description	Value	Ref.
δ	Two-photon absorption cross section at 1064 nm ($S_0 + 2\hbar\omega \rightarrow S'_1$)	t. b. d.	—
σ_{T_1, T_2}	Triplet absorption cross section at 1064 nm ($T_1 + \hbar\omega \rightarrow T_2$)	$1.1 \times 10^{-16} \text{ cm}^2$	Chap. 2
τ_{S_1}	Lifetime of S_1	89 ps	[14–16]
τ_{T_1}	Lifetime of T_1 (includes both phosphorescence and oxygen quenching)	3 μs	[66]
τ_{T_2}	Lifetime of T_2	1.56 ps	Chap. 3
Φ_{isc}	Intersystem crossing yield ($S_1 \rightarrow T_1$)	0.98	[16, 66]
Φ_{risc, T_2}	Reverse intersystem crossing yield ($T_2 \rightarrow S'_1$)	0.0076	Chap. 3
I	Photon intensity	variable	—
k_{ic, T_2}	Internal conversion rate ($T_2 \rightarrow T_1$)	$(1 - \Phi_{\text{risc}, T_2})/\tau_{T_2}$	—
k_{isc}	Intersystem crossing rate ($S_1 \rightarrow T_1$)	$\Phi_{\text{isc}}/\tau_{S_1}$	—
k_r	Thermalization rate ($S'_1 \rightarrow S_1$)	$3 \times 10^{10} \text{ s}^{-1}$	[67, 68]
k_{risc, T_2}	Reverse intersystem crossing rate ($T_2 \rightarrow S'_1$)	$\Phi_{\text{risc}, T_2}/\tau_{T_2}$	—
k_{rot}	Rotational diffusion rate	3.2 ns^{-1}	[69]
k_{T_1}	Relaxation rate of T_1	$1/\tau_{T_1}$	—

Table 5.2: Photophysical parameters of Rhodamine 6G in ethanol that are relevant to 1064-nm excitation.

Symbol	Description	Value	Ref.
δ	Two-photon absorption cross section at 1064 nm ($S_0 + 2\hbar\omega \rightarrow S'_1$)	3.6 GM	[116]
τ_{S_1}	Lifetime of S_1	4.2 ns	[129]
τ_{T_1}	Lifetime of T_1 (includes both phosphorescence and oxygen quenching)	3 μ s	—
Φ_{isc}	Intersystem crossing yield ($S_1 \rightarrow T_1$)	0.0018	[129]
I	Photon intensity	variable	—
k_{isc}	Intersystem crossing rate ($S_1 \rightarrow T_1$)	Φ_{isc} / τ_{S_1}	—
k_r	Thermalization rate ($S'_1 \rightarrow S_1$)	$1.11 \times 10^{12} \text{ s}^{-1}$	[129]
k_{rot}	Rotational diffusion rate	3.2 ns ⁻¹	—
k_{T_1}	Relaxation rate of T_1	$1/\tau_{T_1}$	—

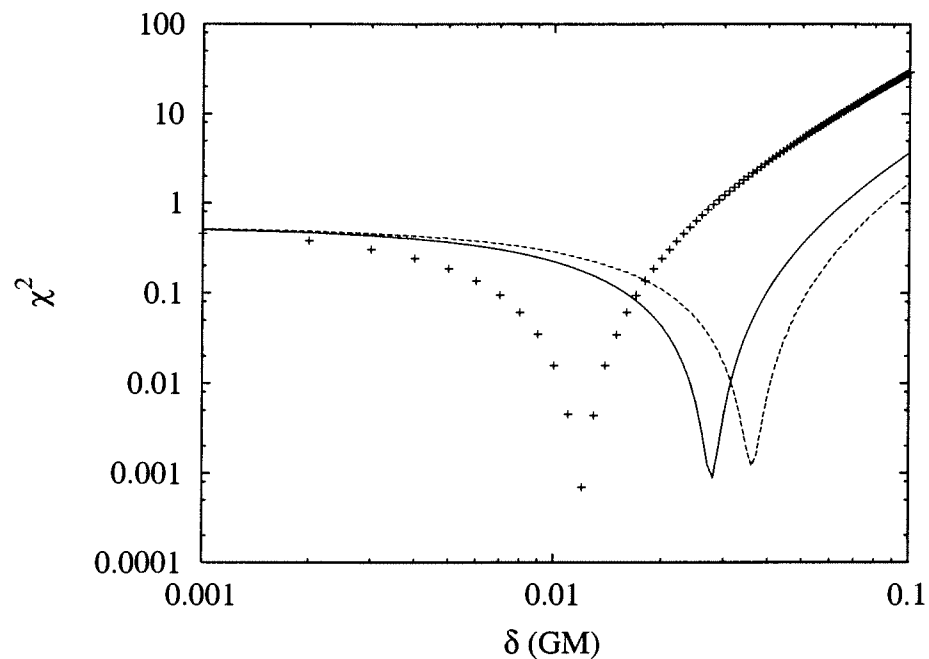


Figure 5.6: The best value of the two-photon absorption cross section δ is determined by locating a minimum in χ^2 of the fit of δ to the 1064-nm excited fluorescence of rose bengal (Fig. 5.4). The three χ^2 curves shown here were run with models with $\Phi_{\text{risc},T_2} = 0.0076$ (—), $\Phi_{\text{risc},T_2} = 0$ (- - -), and $\Phi_{\text{risc},T_2} = 0.12$ (+). The minima are at 0.028, 0.036, and 0.012 GM, respectively.

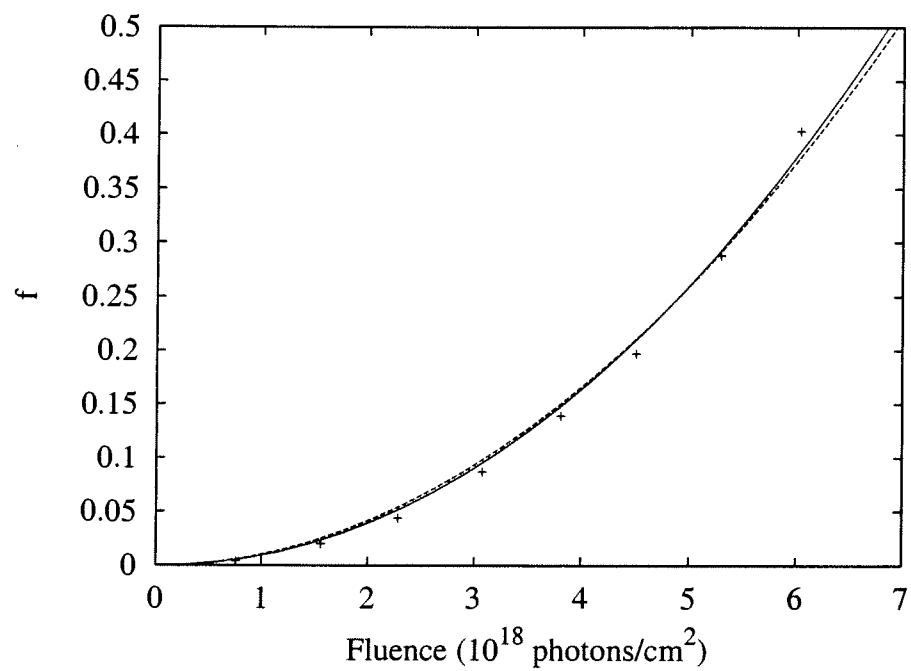


Figure 5.7: Best fit to 1064-nm-excited fluorescence of rose bengal. Model with $\Phi_{\text{risc},T_2} = 0.0076$ and $\delta = 0.028$ GM (—); model with $\Phi_{\text{risc},T_2} = 0$ and $\delta = 0.036$ GM (- - -); data (+).

pulse fluences are well above the saturation limit of the single photon triplet-triplet absorption process. Therefore, the amount of fluorescence resulting from reverse intersystem crossing will be limited only by the two-photon excitation process populating T_1 and not by the subsequent triplet-triplet excitation, producing a strictly quadratic response.

The population dynamics for the two-photon excitation model including the triplet-triplet absorption process are shown in Figs. 5.8, 5.9, and 5.10. Results are shown for a fluence of 6×10^{18} photons/cm². The time-dependent populations of S_1 , T_1 and T_2 are shown for the three cases described above, where $\Phi_{\text{risc},T_2} = 0.0076$ is the actual reverse intersystem crossing yield for this state. Fig. 5.8 shows the dynamics of S_1 . It can be seen that the peak S_1 population shifts to later times as the reverse intersystem crossing yield is increased. This results from the transfer of population from T_2 back to the singlet manifold following excitation of T_1 . The reverse intersystem crossing process results in the three cases having approximately the same T_1 population after the excitation pulse, as shown in Fig. 5.9. This final value is reached more quickly in the case of less reverse intersystem crossing. The dynamics of T_2 are shown in Fig. 5.10. The greatest T_2 population occurs in the case of no reverse intersystem crossing, as should be expected since population is trapped in the triplet manifold in this case. This series of figures clearly reveals the impact of triplet-triplet absorption and reverse intersystem crossing on the dynamics following two-photon excitation.

5.5 Conclusion

The two-photon absorption cross section for rose bengal excited by 1064-nm light is 0.028 GM, over three orders of magnitude less than the 38 GM cross section for fluorescein excited by 782-nm light. The improbability of this transition should

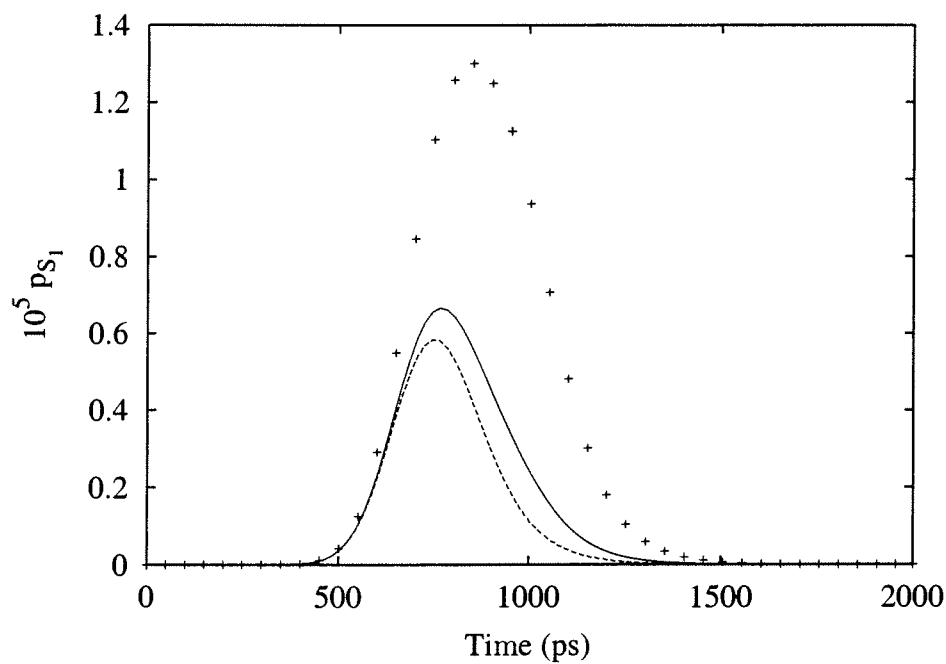


Figure 5.8: Population dynamics of S_1 during multiphoton excitation, calculated using the kinetic model described by Eq. 5.7. $F = 6 \times 10^{18}$ photons/cm². $\Phi_{\text{risc},T_2} = 0.0076$ and $\delta = 0.028$ GM (—); $\Phi_{\text{risc},T_2} = 0$ and $\delta = 0.036$ GM (- - -); $\Phi_{\text{risc},T_2} = 0.12$ and $\delta = 0.012$ GM (+).

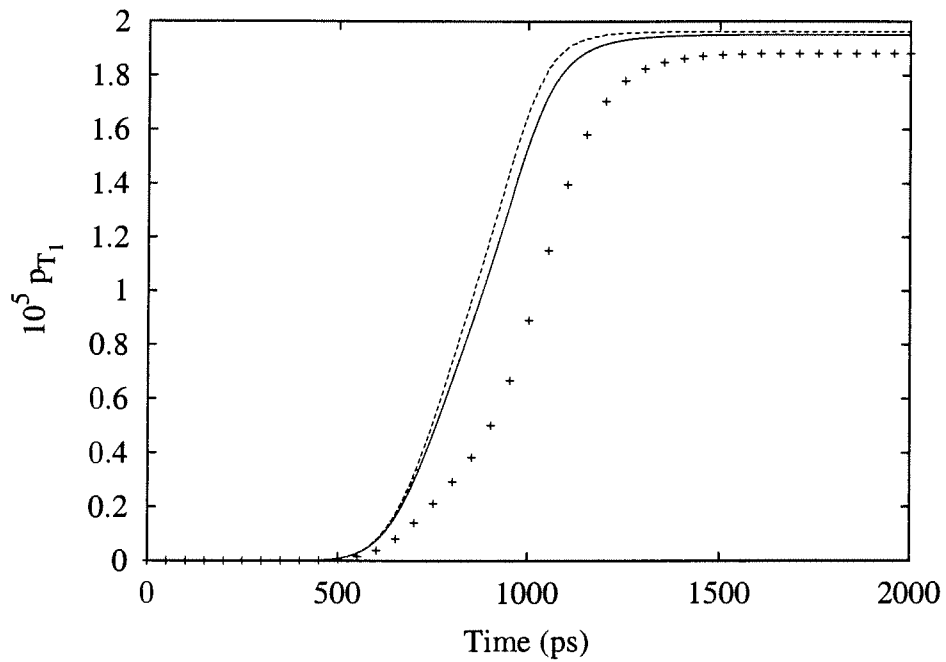


Figure 5.9: Population dynamics of T_1 during multiphoton excitation, calculated using the kinetic model described by Eq. 5.7. $F = 6 \times 10^{18}$ photons/cm². $\Phi_{\text{risc},T_2} = 0.0076$ and $\delta = 0.028$ GM (—); $\Phi_{\text{risc},T_2} = 0$ and $\delta = 0.036$ GM (- - -); $\Phi_{\text{risc},T_2} = 0.12$ and $\delta = 0.012$ GM (+).

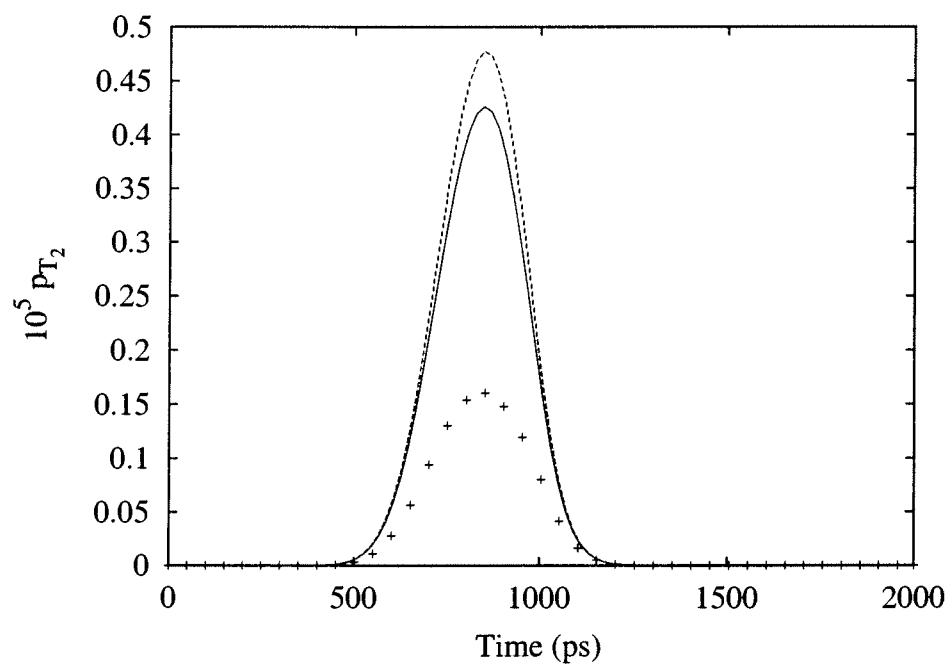


Figure 5.10: Population dynamics of T_2 during multiphoton excitation, calculated using the kinetic model described by Eq. 5.7. $F = 6 \times 10^{18}$ photons/cm². $\Phi_{\text{risc},T_2} = 0.0076$ and $\delta = 0.028$ GM (—); $\Phi_{\text{risc},T_2} = 0$ and $\delta = 0.036$ GM (- - -); $\Phi_{\text{risc},T_2} = 0.12$ and $\delta = 0.012$ GM (+).

not be misunderstood as eliminating the possibility of multiphoton excitation of rose bengal for biological applications. It remains to be determined if other wavelengths, such as those produced by a titanium:sapphire laser, might excite more probable transitions in rose bengal.

Two-photon fluorescence microscopy is a relatively new research tool that is becoming more widespread as the cost and technical knowledge required to use ultrashort pulsed lasers decreases. As this technique becomes more widely adopted the need for accurate two-photon absorption cross sections will become more critical. The case of rose bengal suggests that observation of a quadratic power law is not sufficient evidence to justify neglecting processes involving excited states. The example of rose bengal also shows that an inappropriate model of the system, not surprisingly, can lead to inaccurate results. The two examples of fits using incorrect reverse intersystem crossing yields show that the effect can cause significant deviations from that found using the correct yield. The presence of higher-lying states must be included in models of multiphoton excitation, especially for molecules with a large $S_1 \rightarrow T_1$ intersystem crossing yield.

Chapter 6

Summary and suggestions for future work

6.1 Summary

Our decision to study rose bengal was prompted by indications in the work of other groups that the higher-lying states of rose bengal had particularly interesting properties. Oxygen-independent photochemistry had been observed to occur from some higher-lying states of rose bengal. The factors producing this chemistry from some states but not others were not known. Other studies showed that rose bengal had one of the highest reverse intersystem crossing yields ever observed. Finally, rhodamines with a structure similar to rose bengal had large two-photon absorption cross sections, suggesting that perhaps two-photon excitation of rose bengal would be probable. One difference between rhodamines and rose bengal is the yield of triplet states. Rose bengal's large yield of triplet states suggested that the potential effects of excited state absorption during multiphoton excitation would be enhanced compared to the rhodamines.

Our selection of rose bengal for detailed study was based on practical considerations as well as the reasons given above. Frequency doubling of the Nd:YAG laser available for this work produced 532-nm light, allowing the excitation of a strong ground state absorption band of rose bengal in water. The existence of strong single photon absorption at this wavelength also indicated that two-photon excitation of rose bengal by 1064-nm light, the Nd:YAG fundamental, was energetically feasible. In addition, we assumed that there were triplet states closely associated with the singlet states populated by absorption of 532-nm and 355-nm light by the ground state. On the basis of this assumption we predicted that there would be strong triplet-triplet absorption near 1064 nm, corresponding to the energy difference between 532-nm and 355-nm photons. Triplet states of rose bengal had not been previously studied in the near-infrared. Such a triplet state was of particular interest because it would have an energy slightly below an ultraviolet-excited singlet state previously observed to produce oxygen-independent damage.

Our prediction of strong near-infrared triplet-triplet absorption was confirmed by our flash photolysis experiments described in Chapter 2. These experiments led to the identification of a previously unknown triplet state of rose bengal, denoted T_2 . This state can be excited efficiently since there is a $T_1 \rightarrow T_2$ absorption cross section of $(1.1 \pm 0.1) \times 10^{-16} \text{ cm}^2$ at 1064 nm. Other properties of this state were determined in our experiments and will be described below.

Oxygen-independent damage had been observed for T_3 , a state excited by 640-nm light, but not for the more energetic T_4 , a state excited by 532-nm light. The workers who had conducted these studies were unable to provide an explanation for this behavior. We proposed that a photophysical depletion of the triplet manifold due to reverse intersystem crossing from T_4 might prevent the numerous excitations of the higher-lying state necessary to produce a substantial

yield of photoproducts. We have conducted experimental and theoretical work to determine whether this proposed mechanism can explain the observations of oxygen-independent damage. Our proposed explanation of photoproduct yields being dependent on reverse intersystem crossing yields required that the yield of reverse intersystem crossing from T_4 be substantially different than that from T_3 . Several previous workers had suggested that reverse intersystem crossing yields would be essentially independent of the higher-lying state excited. According to their hypothesis, rapid internal conversion from higher-lying states to T_2 would effectively prevent reverse intersystem crossing from these states. The internal conversion from T_2 to T_1 was assumed to occur more slowly and thus allow reverse intersystem crossing from T_2 . Therefore they hypothesized that all higher-lying states would have a reverse intersystem crossing yield approximately equal to that of T_2 . The first step in confirming our reverse-intersystem-crossing proposal was to answer the question of whether the yield of reverse intersystem crossing was state-dependent, contrary to the hypothesis of other workers. Reverse intersystem crossing yields of 0.0076 for T_2 , < 0.06 for T_3 , and 0.12 for T_4 were found, clearly showing that the yield depends on the particular state initially excited. Our experiments using one-step and two-step laser-induced fluorescence to determine reverse intersystem crossing yields are described in Chapter 3.

The next question we sought to answer was whether these differences in yields of reverse intersystem crossing could produce significant differences in photoproduct yield. The validation of that hypothesis required investigation, as described in Chapter 4. Through the use of a kinetic model including both reverse intersystem crossing and photoproduct formation from a higher-lying triplet state it was found that reverse intersystem crossing can account for less than a 10% reduction in radical yield. At this time our proposed mechanism cannot explain most of the

photochemical differences between T_3 and T_4 . However, this modeling is based on the assumption that the photophysical parameters of rose bengal in the biological medium were the same as those in water. It is still possible that reverse intersystem crossing could explain the observed differences in biological effects since the radical yield could change more significantly in a biological environment or there might be a threshold for the biological response.

Oxygen-independent damage is believed to result from radicals produced by cleavage of one of rose bengal's carbon-iodine bonds. The energy required to cleave this bond is not known from theoretical calculations. Chapter 4 describes our experiments to determine whether T_2 , the least energetic triplet state identified in rose bengal, is sufficiently energetic to result in bond cleavage. Analysis of two-step laser-induced bleaching data indicates that it is most probable that no bond cleavage occurs from this state. An upper limit of 0.0008 was found for the yield of photoproducts from T_2 . On the basis of this experiment we believe that an energy greater than 2.9 eV is required to cleave the carbon-iodine bond in rose bengal in water.

We predicted that reverse intersystem crossing would have a substantial impact on two-photon absorption cross sections determined using a fluorescence technique described in Chapter 5. Triplet-triplet absorption allowed for the excitation of T_2 during 1064-nm excitation of rose bengal. Reverse intersystem crossing from this state led to an enhancement of fluorescence and thus interfered with the determination of the two-photon absorption cross section. This effect could be accounted for by using a model that included the yield of reverse intersystem crossing for T_2 . A cross section of 0.028 ± 0.001 GM was found for the two-photon excitation of the ground state. Strong two-photon transitions have cross sections greater than 10 GM, so the excitation of the rose bengal ground

state by 1064-nm light is relatively improbable. The effect of reverse intersystem crossing on the determination of the two-photon absorption cross section was demonstrated by performing the analysis with three different values for the yield of this process, 0, 0.12, and the actual value of 0.0076 determined in Chapter 3. In the absence of reverse intersystem crossing the best fit of the fluorescence data gave $\delta = 0.036 \pm 0.001$ GM, 28% larger than that found using the actual yield. With an overly large yield of 0.12 the best fit gave $\delta = 0.012 \pm 0.001$ GM, less than half of the actual two-photon absorption cross section. This confirmed our prediction that the neglect of reverse intersystem crossing can lead to an apparent enhancement of the two-photon absorption cross section in the analysis of fluorescence data.

6.2 Suggestions for future work

As the result of the work presented in this thesis, rose bengal now appears to be the photosensitizer with the most completely characterized higher-lying states. Photosensitizers that are more actively used in clinical photodynamic therapy should have their higher-lying states studied with equal thoroughness. When not already known, the triplet-triplet absorption spectra of these molecules in the far-red and near-infrared should be determined. The transmission of light through tissue is greatest in this spectral region and is therefore of particular interest. Unfortunately, most earlier studies of triplet-triplet absorption looked at shorter wavelengths, largely because of the availability of superior photodetectors in this region. Improvements in far-red and near-infrared detectors now allow more measurements to be made in this region.

Good photosensitizers have a large $S_1 \rightarrow T_1$ intersystem crossing yield, often resulting from the internal heavy atom effect. This also makes photosensitiz-

ers strong candidates for possessing significant reverse intersystem crossing from higher-lying triplet states. The list of molecules known to have large reverse intersystem crossing yields is fairly short, so identification of additional molecules with large yields would aid deeper understanding of the factors contributing to this process as well as its consequences. It is also prudent to verify the Redmond *et al.* results for Merocyanine 540 using an alternative method that does not use tetraphenylporphyrin as an actinometric reference.

The experimental studies of rose bengal described in this thesis benefited from the work of others to determine many of the photophysical parameters of rose bengal. In particular, our analysis was aided by knowledge of the rotational diffusion rate of rose bengal in water and the thermalization rate for the S_1 state. These parameters are not known for most other photosensitizers and therefore represent additional work that must be done before the properties of the higher-lying states can be determined.

Further studies of reverse intersystem crossing in rose bengal are also of interest. Although the variation of reverse intersystem crossing yield for the various triplet states discussed in this thesis is suggestive of a strong dependence on the relevant triplet-singlet energy gap, the fact that different combinations of triplet and singlet states are involved prevents a clear application of the energy gap law. However, changing the solvent can produce shifts in the energy gaps between triplet and singlet states, allowing the energy gap for a particular triplet-singlet pairing to be varied. This phenomena can be used to more carefully study the energy gap law in the context of reverse intersystem crossing.

As described in Chapter 4, there is evidence for oxygen-independent damage from the higher-lying states of several photosensitizers. A systematic study of this process in a variety of photosensitizers would increase our knowledge of the conditions required to produce oxygen-independent damage. This could po-

tentially allow for the design of a photosensitizer capable of efficiently producing oxygen-independent damage. These studies would be furthered by the use of standardized biological assays that would allow for quantitative comparison of the ability to produce oxygen-independent damage under various conditions.

Bibliography

- [1] M. Kasha, "Paths of molecular excitation," *Radiation Research, Supplement* **2**, 243–275 (1960).
- [2] C. Cohen-Tannoudji, B. Diu, and F. Laloë, *Quantum Mechanics* (Wiley-Interscience, New York, 1977).
- [3] P. W. Atkins, *Physical Chemistry* (Freeman, San Francisco, 1978).
- [4] G. Herzberg, *Atomic Spectra and Atomic Structure* (Dover, New York, 1944).
- [5] G. N. Lewis and M. Kasha, "Phosphorescence and the triplet state," *Journal of the American Chemical Society* **66**, 2100–2116 (1944).
- [6] A. Jabłoński, "Über den Mechanismus der Photolumineszenz von Farbstoffphosphoren," *Zeitschrift für Physik* **94**, 38–46 (1935).
- [7] G. Lewis, D. Lipkin, and T. T. Magel, "Reversible photochemical processes in rigid media. A study of the phosphorescent state," *Journal of the American Chemical Society* **63**, 3005–3018 (1941).
- [8] J. D. Jackson, *Classical Electrodynamics*, 2nd ed. (John Wiley & Sons, New York, 1975), pp. 541–547.
- [9] R. M. Hochstrasser, *Behavior of Electrons in Atoms* (Benjamin, New York, 1964).
- [10] R. Englman and J. Jortner, "The energy gap law for radiationless transitions in large molecules," *Molecular Physics* **18**, 145–164 (1970).
- [11] V. Chynwat and H. A. Frank, "The application of the energy gap law to the S_1 energies and dynamics of carotenoids," *Chemical Physics* **194**, 237–244 (1995).
- [12] A. J. McLean, D. J. McGarvey, and T. G. Truscott, "Effect of oxygen-enhanced intersystem crossing on the observed efficiency of formation of

- singlet oxygen," *Journal of the Chemical Society. Faraday Transactions* **86**, 3075–3080 (1990).
- [13] M. Gouterman and G.-E. Kahill, "Porphyrin free base phosphorescence," *Journal of Molecular Spectroscopy* **53**, 88–100 (1974).
- [14] H. Stiel, K. Teuchner, A. Paul, D. Leupold, and I. E. Kochevar, "Quantitative comparison of excited state properties and intensity-dependent photosensitization by rose bengal," *Journal of Photochemistry and Photobiology, B: Biology* **33**, 245–254 (1996).
- [15] G. R. Fleming, A. W. E. Knight, J. M. Morris, R. J. S. Morrison, and G. W. Robinson, "Picosecond fluorescence studies of xanthene dyes," *Journal of the American Chemical Society* **99**, 4306–4311 (1977).
- [16] M. A. J. Rodgers, "Picosecond fluorescence studies of rose bengal in aqueous micellar dispersions," *Chemical Physics Letters* **78**, 509–514 (1981).
- [17] O. Raab, "Ueber die Wirkung fluorescirender Stoffe auf Infusorien," *Zeitschrift für Biologie* **39**, 524–546 (1900).
- [18] H. von Tappeiner and A. Jesionek, "Therapeutische Versuche mit fluoreszierenden Stoffen," *Münchener medizinische Wochenschrift* **47**, 2042–2044 (1903).
- [19] F. H. J. Figge, G. S. Weiland, and L. O. J. Mangianello, "Cancer detection and therapy. Affinity of neoplastic, embryonic, and traumatized tissues for porphyrins and metalloporphyrins," *Proceedings of the Society for Experimental Biology and Medicine*. **68**, 640–641 (1948).
- [20] R. L. Lipson, E. J. Baldes, and A. M. Olsen, "The use of a derivative of hematoporphyrin in tumor detection," *Journal of the National Cancer Institute* **26**, 1–8 (1961).
- [21] T. J. Dougherty, "Activated dyes as antitumor agents," *Journal of the National Cancer Institute* **52**, 1333–1336 (1974).
- [22] M. D. Daniell and J. S. Hill, "A history of photodynamic therapy," *Australian and New Zealand Journal of Surgery* **61**, 340–348 (1991).
- [23] H. I. Pass, "Photodynamic therapy in oncology: mechanisms and clinical use," *Journal of the National Cancer Institute* **85**, 443–456 (1993).
- [24] T. J. Dougherty, C. J. Gomer, B. W. Henderson, G. Jori, D. Kessel, M. Korbelik, and Q. Peng, "Photodynamic therapy," *Journal of the National Cancer Institute* **90**, 889–905 (1998).

- [25] D. C. Neckers, "The Indian happiness wart in the development of photodynamic action," *Journal of Chemical Education* **64**, 649–656 (1987).
- [26] J. Henkel, "From shampoo to cereal: seeing to the safety of color additives," In *FDA Consumer*, (United States Food and Drug Administration, December 1993), also available from <http://www.fda.org>.
- [27] Y. Iwamoto, C. Tominaga, and Y. Yanagihara, "Photodynamic activities of food additive dyes on the yeast *Saccharomyces cerevisiae*," *Chemical and Pharmaceutical Bulletin* **37**, 1632–1634 (1989).
- [28] D. C. Neckers and O. M. Valdes-Aguilera, in *Advances in Photochemistry*, D. Volman, G. S. Hammond, and D. C. Neckers, eds., (John Wiley & Sons, New York, 1993), Vol. 18, Chap. Photochemistry of the Xanthene Dyes, pp. 315–395.
- [29] H. von Tappeiner and A. Jodlbauer, "Über die Wirkung der photodynamischen (fluoreszierenden) Stoffe auf Protozoen und Enzyme," *Deutsches Archiv für klinische Medizin* **80**, 427–487 (1904).
- [30] J. Lenard, A. Rabson, and R. Vanderoef, "Photodynamic inactivation of infectivity of human immunodeficiency virus and other enveloped viruses using hypericin and rose bengal: Inhibition of fusion and syncytia formation," *Proceedings of the National Academy of Science USA* **90**, 158–162 (1993).
- [31] T. A. Dahl, O. Valdes-Aguilera, W. R. Midden, and D. C. Neckers, "Partition of rose bengal anion from aqueous medium into a lipophilic environment in the cell envelope of *Salmonella typhimurium*: implications for cell-type targeting in photodynamic therapy," *Journal of Photochemistry and Photobiology, B: Biology* **4**, 171–184 (1989).
- [32] F. S. Cruz, L. A. V. Lopes, W. de Souza, S. N. J. Moreno, R. P. Mason, and R. Docampo, "The photodynamic action of rose bengal on *Trypanosoma cruzi*," *Acta Tropica* **41**, 99–108 (1984).
- [33] J. M. Larkin, W. R. Donaldson, T. H. Foster, and R. S. Knox, "Reverse intersystem crossing from a triplet state of rose bengal populated by sequential 532- + 1064-nm laser excitation," *Chemical Physics* **244**, 319–330 (1999).
- [34] J. M. Larkin, W. R. Donaldson, T. H. Foster, and R. S. Knox, "Near infrared spectroscopic studies of the triplet states of Rose Bengal," oral presentation, 1998, American Society for Photobiology Annual Meeting.

- [35] R. G. W. Norrish and G. Porter, "Chemical reactions produced by very high light intensities," *Nature* **164**, 658 (1949).
- [36] G. Porter, "Flash photolysis and spectroscopy: a new method for the study of free radical reactions," *Proceedings of the Royal Society of London A* **200**, 284–300 (1950).
- [37] R. V. Bensasson, E. J. Land, and T. G. Truscott, *Excited States and Free Radicals in Biology and Medicine: Contributions from Flash Photolysis and Pulse Radiolysis* (Oxford University Press, New York, 1993).
- [38] I. Carmichael and G. L. Hug, "Triplet-triplet absorption spectra of organic molecules in condensed phases," *Journal of Physical and Chemical Reference Data* **15**, 1–250 (1986).
- [39] I. Carmichael and G. L. Hug, "A note on the total depletion method of measuring extinction coefficients of triplet-triplet transitions," *Journal of Physical Chemistry* **89**, 4036–4039 (1985).
- [40] U. Lachish, A. Shafferman, and G. Stein, "Intensity dependence in laser flash photolysis experiments: hydrated electron formation from ferrocyanide, tyrosine, and tryptophan," *Journal of Chemical Physics* **64**, 4205–4211 (1976).
- [41] P. Murasecco-Suardi, E. Gassmann, A. M. Braun, and E. Oliveros, "Determination of the quantum yield of intersystem crossing of rose bengal," *Helvetica Chimica Acta* **70**, 1761–1773 (1987).
- [42] S. P. McGlynn, T. Azumi, and M. Kinoshita, *Molecular Spectroscopy of the Triplet State* (Prentice-Hall, Englewood Cliffs, NJ, 1969).
- [43] C. A. Parker, *Photoluminescence of Solutions: with applications to Photochemistry and Analytical Chemistry* (Elsevier, New York, 1968).
- [44] C. A. Parker and C. G. Hatchard, "Triplet-singlet emission in fluid solutions: phosphorescence of eosin," *Transactions of the Faraday Society* **57**, 1894–1904 (1961).
- [45] S. I. Vavilov, "The dependence of the intensity of fluorescence dyes on the wavelength of the exciting light," *Philosophical Magazine* **43**, 307–320 (1922).
- [46] M. Kasha, "Characterization of electronic transitions in complex molecules," *Discussions of the Faraday Society* **9**, 14–19 (1950).
- [47] M. Beer and H. C. Longuet-Higgins, "Anomalous light emission of azulene," *Journal of Chemical Physics* **23**, 1390–1391 (1955).

- [48] G. Viswanath and M. Kasha, "Confirmation of the anomalous fluorescence of azulene," *Journal of Chemical Physics* **24**, 574–577 (1956).
- [49] R. A. Keller, "Intersystem crossing from excited triplet states into the singlet manifold," In *Molecular Luminescence*, E. C. Lim, ed., pp. 453–468 (Benjamin, New York, 1969).
- [50] S. Kobayashi, K. Kikuchi, and H. Kokubun, "Fluorescence of the anthracenes following $T_n \leftarrow T_1$ excitation studied by a double excitation method," *Chemical Physics Letters* **42**, 494–497 (1976).
- [51] S. Kobayashi, K. Kikuchi, and H. Kokubun, "Nonradiative relaxation processes of the higher excited triplet states of anthracenes studied by a double excitation method," *Chemical Physics* **27**, 399–407 (1978).
- [52] H. Fukumura, K. Kikuchi, K. Koike, and H. Kokubun, "Temperature effect on inverse intersystem crossing of anthracenes," *Journal of Photochemistry and Photobiology, A: Chemistry* **42**, 283–291 (1988).
- [53] W. G. McGimpsey and J. C. Scaiano, "Photochemistry and photophysics from upper triplet levels of 9,10-bibromoanthracene," *Journal of the American Chemical Society* **111**, 335–340 (1989).
- [54] G. A. Ketsle, L. V. Levshin, and S. N. Letuta, "Photoprocesses in phosphor molecules under stepwise two-photon excitation," *Optics and Spectroscopy (USSR)* **68**, 202–204 (1990).
- [55] P.-T. Chou, M. L. Martinez, and S. L. Studer, "Studies of $T_2 \rightarrow S_1$ intersystem crossing for coumarins," *Chemical Physics Letters* **188**, 49–53 (1992).
- [56] K. Tokumura, N. Yagata, Y. Fujiwara, and M. Itoh, "Two-step laser-induced-fluorescence study of 2',3',4',5',6'-pentamethyl-3-hydroxyflavone in solution at room temperature: contribution of triplet states and confirmation of ground-state tautomer," *Journal of Physical Chemistry* **97**, 6656–6663 (1993).
- [57] K. Tokumura, M. Kurauchi, N. Yagata, and M. Itoh, "Reverse intersystem crossing from higher triplet to excited singlet in 2,2'-bipyridine-3,3'-diol phototautomer," *Journal of Photochemistry and Photobiology, A: Chemistry* **81**, 151–158 (1994).
- [58] K. Tokumura, M. Kurauchi, N. Yagata, and M. Itoh, "Phototautomerization of 3-hydroxyflavone in the lowest triplet state," *Chemical Physics Letters* **258**, 495–500 (1996).

- [59] S. Reindl and A. Penzkofer, "Higher excited-state triplet-singlet intersystem crossing of some organic dyes," *Chemical Physics* **211**, 431–439 (1996).
- [60] R. W. Redmond, I. E. Kochevar, M. Krieg, G. Smith, and W. G. McGimpsey, "Excited state relaxation in cyanine dyes: a remarkably efficient reverse intersystem crossing from upper triplet levels," *Journal of Physical Chemistry A* **101**, 2773–2777 (1997).
- [61] M. A. El-Sayed, "Spin-orbit coupling and the radiationless processes in nitrogen heterocyclics," *Journal of Chemical Physics* **38**, 2834–2838 (1963).
- [62] N. Durán and G. Cilento, "Long-range triplet-singlet energy transfer from enzyme generated triplet acetone to xanthene dyes," *Photochemistry and Photobiology* **32**, 113–116 (1980).
- [63] C. R. Lambert, I. E. Kochevar, and R. W. Redmond, "Differential reactivity of upper triplet states produces wavelength-dependent two-photon photosensitization using rose bengal," *Journal of Physical Chemistry B* **103**, 3737–3741 (1999).
- [64] *Topics in Fluorescence Spectroscopy*, J. R. Lakowicz, ed., (Plenum, New York, 1991), Vol. 1. Techniques.
- [65] C. R. Lambert, H. Stiel, D. Leupold, M. C. Lynch, and I. E. Kochevar, "Intensity-dependent enzyme photosensitization using 532 nm nanosecond laser pulses," *Photochemistry and Photobiology* **63**, 154–160 (1996).
- [66] P. C. C. Lee and M. A. J. Rodgers, "Laser flash photokinetic studies of rose-bengal sensitized photodynamic," *Photochemistry and Photobiology* **45**, 79–86 (1987).
- [67] R. R. Alfano and S. L. Shapiro, "Direct measurement of the vibrational decay of dye molecules in the excited state," *Optics Communications* **6**, 98–100 (1972).
- [68] I. Kitazima, N. Miyana, and H. Iwasawa, "Direct measurement of vibrational decay and fluorescence lifetime of erythrosine dye in S_1 -excited state," *Japanese Journal of Applied Physics* **17**, 243–244 (1978).
- [69] E. W. Small, L. J. Libertini, D. W. Brown, and J. R. Small, "Optical studies of molecular motions: using fluorescence anisotropy decays to determine the shapes of dye molecules, proteins, and nucleosomes," *Optical Engineering* **30**, 345–355 (1991).
- [70] G. Bader and P. Deuffhard, "A semi-implicit mid-point rule for stiff systems of ordinary differential equations," *Numerische Mathematik* **41**, 373–398 (1983).

- [71] W. H. Press, S. A. Teukolsky, W. T. Vetterling, and B. P. Flannery, *Numerical Recipes in C: the Art of Scientific Computing* (Cambridge University Press, Cambridge, 1992).
- [72] R. A. Van Calcor, M. J. G. Heuts, B. K. Van Uitert, H. A. J. Meijer, T. J. Hollander, and C. T. J. Alkemade, "Power broadening of the Na-D lines in a flame — II. The fluorescence line width as a function of the spectral irradiance of the pulsed dye laser," *Journal of Quantitative Spectroscopy and Radiative Transfer* **28**, 1–12 (1982).
- [73] G. Smith, W. G. McGimpsey, M. C. Lynch, I. E. Kochevar, and R. W. Redmond, "An efficient oxygen independent two-photon photosensitization mechanism," *Photochemistry and Photobiology* **59**, 135–139 (1994).
- [74] T. Shen, Z.-G. Zhao, Q. Yu, and H.-J. Xu, "Photosensitized reduction of benzil by heteroatom-containing anthracene dyes," *Journal of Photochemistry and Photobiology, A: Chemistry* **47**, 203–212 (1989).
- [75] V. M. Mullooly, A. L. Abramson, and M. J. Shikowitz, "Dihematoporphyrin ether-induced photosensitivity in laryngeal papilloma patients," *Lasers in Surgery and Medicine* **10**, 349–356 (1990).
- [76] R. H. Thomlinson and L. H. Gray, "The histological structure of some human lung cancers and the possible implications for radiotherapy," *British Journal of Cancer* **9**, 539–549 (1955).
- [77] H. Yamaura and T. Matsuzawa, "Tumor regrowth after irradiation: an experimental approach," *International Journal of Radiation Biology* **35**, 201–209 (1979).
- [78] J. M. Brown, "Evidence for acutely hypoxic cells in mouse tumours, and a possible mechanism of reoxygenation," *British Journal of Radiology* **52**, 650–656 (1979).
- [79] H. S. Reinhold, B. Blachiewicz, and A. Blok, "Oxygenation and reoxygenation in 'sandwich' tumours," In *Bibliotheca Anatomica*, D. H. Lewis, ed., **15**, 270–272 (Karger, Basel, Switzerland, 1977).
- [80] B. Chance and F. Jöbsis, "Chances in fluorescence in a frog sartorius muscle following a twitch," *Nature* **184**, 195–196 (1959).
- [81] B. Chance, P. Cohen, F. Jobsis, and B. Schoener, "Localized fluorometry of oxidation-reduction states of intracellular pyridine nucleotide in brain and kidney cortex of the anesthetized rat," *Science* **136**, 325 (1962).

- [82] T. H. Foster, R. S. Murant, R. G. Bryant, R. S. Knox, S. L. Gibson, and R. Hilf, "Oxygen consumption and diffusion effects in photodynamic therapy," *Radiation Research* **126**, 296–303 (1991).
- [83] T. H. Foster and L. Gao, "Dosimetry in photodynamic therapy: oxygen and the critical importance of capillary density," *Radiation Research* **130**, 379–383 (1992).
- [84] T. H. Foster, D. F. Hartley, M. G. Nichols, and R. Hilf, "Fluence rate effects in photodynamic therapy of multicell tumor spheroids," *Cancer Research* **53**, 1249–1254 (1993).
- [85] M. G. Nichols and T. H. Foster, "Oxygen diffusion and reaction kinetics in the photodynamic therapy of multicell tumor spheroids," *Physics in Medicine and Biology* **39**, 2161–2181 (1994).
- [86] P. W. McLearn and R. E. Hayden, "Prevention of cutaneous phototoxicity in photodynamic therapy," *American Journal of Otolaryngology* **10**, 92–98 (1989).
- [87] S. W. Young, K. W. Woodburn, M. Wright, T. D. Mody, Q. Fan, J. L. Sessler, W. C. Dow, and R. A. Miller, "Lutetium texaphyrin (PCI-0123): a near-infrared, water-soluble photosensitizer," *Photochemistry and Photobiology* **63**, 892–897 (1996).
- [88] G. Bottiroli, A. C. Croce, P. Balzarini, D. Locatelli, P. Baglioni, P. Lo Nostro, M. Monici, and R. Pratesi, "Enzyme-assisted cell photosensitization: a proposal for an efficient approach to tumor therapy and diagnosis. The rose bengal fluorogenic substrate," *Photochemistry and Photobiology* **66**, 374–383 (1997).
- [89] S. L. Gibson, K. R. VanDerMeid, R. S. Murant, R. F. Raubertas, and R. Hilf, "Effects of various photoradiations regimens on the antitumor efficacy of photodynamic therapy for R3230AC mammary carcinomas," *Cancer Research* **50**, 7236–7241 (1990).
- [90] R. H. Feins, R. Hilf, H. Ross, and S. L. Gibson, "Photodynamic therapy for human malignant mesothelioma in the nude mouse," *Journal of Surgical Research* **49**, 311–314 (1990).
- [91] D. Leupold and W. Freyer, "Proposal of modified mechanisms for photodynamic therapy," *Journal of Photochemistry and Photobiology, B: Biology* **12**, 311–314 (1992).

- [92] D. Leupold, W. Freyer, and H. Stiel, "Higher excited sensitizer states in photodynamic therapy. Reply to comment by T. Vidoczy," *Journal of Photochemistry and Photobiology, B: Biology* **17**, 84–86 (1993).
- [93] T. Vidoczy, "On the feasibility of modified mechanisms of photodynamic therapy proposed by Leupold and Freyer," *Journal of Photochemistry and Photobiology, B: Biology* **17**, 83–84 (1993).
- [94] G. I. Kobyshev, G. N. Lyalin, and A. N. Terenin, "Intermolecular energy transfer from the excited triplet level," *Optics and Spectroscopy* **21**, 74–75 (1966).
- [95] T. I. Karu, P. G. Kryukov, V. S. Letokhov, Y. A. Matveetz, and V. A. Semchishen, "High quantum yield of photochemical reactions of protoporphyrin-IX induced by powerful ultrashort laser pulses," *Applied Physics* **24**, 245–247 (1981).
- [96] A. Andreoni, R. Cubeddu, S. de Silvestri, P. Laporta, and O. Svelto, "Two-step laser activation of hematoporphyrin derivative," *Chemical Physics Letters* **88**, 37–39 (1982).
- [97] A. Andreoni, "Two-step photoactivation of hematoporphyrin by excimer-pump dye laser pulses," *Journal of Photochemistry and Photobiology, B: Biology* **1**, 181–193 (1987).
- [98] E. N. Fluhler, J. K. Hurley, and I. E. Kochevar, "Laser intensity and wavelength dependence of Rose-Bengal-photosensitized inhibition of red blood cell acetylcholinesterase," *Biochimica et Biophysica Acta* **990**, 269–275 (1989).
- [99] M. T. Allen, M. Lynch, A. Lagos, R. W. Redmond, and I. E. Kochevar, "A wavelength dependent mechanism for rose bengal-sensitized photoinhibition of red cell acetylcholinesterase," *Biochimica et Biophysica Acta* **1075**, 42–49 (1991).
- [100] T. A. Ciulla, J. R. van Camp, E. Rosenfeld, and I. E. Kochevar, "Photosensitization of single-strand breaks in pBR322 DNA by rose bengal," *Photochemistry and Photobiology* **49**, 293–298 (1989).
- [101] C. R. Lambert and I. E. Kochevar, "Does rose bengal triplet generate superoxide anion?," *Journal of the American Chemical Society* **118**, 3297–3298 (1996).
- [102] C. Lambert, T. Sarna, and T. G. Truscott, "Rose bengal radicals and their reactivity," *Journal of the Chemical Society. Faraday Transactions* **86**, 3879–3882 (1990).

- [103] M. J. Peak, J. G. Peak, C. S. Foote, and N. I. Krinsky, "Oxygen-independent direct deoxyribonucleic acid backbone breakage caused by rose bengal and visible light," *Journal of Photochemistry* **25**, 309–315 (1984).
- [104] K. F. Freed and Y. B. Band, in *Excited States*, E. C. Lim, ed., (Academic Press, New York, 1977), Vol. 3, Chap. Product energy distributions in the dissociation of polyatomic molecules, pp. 109–201.
- [105] D. F. McMillen and D. M. Golden, "Hydrocarbon bond dissociation energies," *Annual Review of Physical Chemistry* **33**, 493–532 (1982).
- [106] J. A. Kerr, "Bond dissociation energies by kinetic methods," *Chemical Reviews* **66**, 465–500 (1966).
- [107] S. W. Benson, "Bond energies," *Journal of Chemical Education* **42**, 502–518 (1965).
- [108] L. J. J. Laarhoven, P. Mulder, and D. D. M. Wayner, "Determination of bond dissociation enthalpies in solution by photoacoustic calorimetry," *Accounts of Chemical Research* **32**, 342–349 (1999).
- [109] J. C. Scaiano, L. J. Johnston, W. G. McGimpsey, and D. Weir, "Photochemistry of organic reaction intermediates: novel reaction paths induced by two-photon laser excitation," *Accounts of Chemical Research* **21**, 22–29 (1988).
- [110] I. Georgakoudi, M. G. Nichols, and T. H. Foster, "The mechanism of Photofrin[®] photobleaching and its consequences for photodynamic dosimetry," *Photochemistry and Photobiology* **65**, 135–144 (1997).
- [111] M. Göppert-Mayer, "Über Elementarakte mit zwei Quantensprüngen," *Annalen der Physik* **9**, 273–294 (1931).
- [112] J. P. Hermann and J. Ducuing, "Absolute measurement of two-photon cross sections," *Physical Review A* **5**, 2557–2568 (1972).
- [113] W. M. McClain, "Two-photon molecular spectroscopy," *Accounts of Chemical Research* **7**, 129–135 (1974).
- [114] P. T. C. So, H. Kim, and I. E. Kochevar, "Two-photon deep tissue ex vivo imaging of mouse dermal and subcutaneous structures," *Optics Express* **3**, 339–350 (1998).
- [115] D. J. Bradley, M. H. R. Hutchinson, H. Koetser, T. Morrow, G. H. C. New, and M. S. Petty, "Interactions of picosecond laser pulses with organic molecules: I. two-photon fluorescence quenching and singlet excited state

- excitation in Rhodamine dyes," Proceedings of the Royal Society of London A **328**, 97–121 (1972).
- [116] D. J. Bradley, M. H. R. Hutchinson, and H. Koetser, "Interactions of picosecond laser pulses with organic molecules: II. two-photon absorption cross-sections," Proceedings of the Royal Society of London A **329**, 105–119 (1972).
- [117] R. L. Swofford and W. M. McClain, "The effect of spatial and temporal laser beam characteristics on two-photon absorption," Chemical Physics Letters **34**, 455–460 (1975).
- [118] C. Xu and W. W. Webb, "Measurement of two-photon excitation cross sections of molecular fluorophores with data from 690 to 1050 nm," Journal of the Optical Society of America B **13**, 481–491 (1996).
- [119] W. G. Fisher, W. P. Partridge, Jr., C. Dees, and E. A. Wachter, "Simultaneous two-photon activation of type-I photodynamic therapy agents," Photochemistry and Photobiology **66**, 141–155 (1997).
- [120] C. Xu and W. W. Webb, in *Topics in Fluorescence Spectroscopy*, J. Lakowicz, ed., (Plenum, New York, 1997), Vol. 5: Nonlinear and Two-Photon-Induced Fluorescence, Chap. Multiphoton Excitation of Molecular Fluorophores and Nonlinear Laser Microscopy, pp. 471–540.
- [121] W. Kaiser and C. G. B. Garrett, "Two-photon excitation in $\text{CaF}_2:\text{Eu}^{2+}$," Physical Review Letters **7**, 273–295 (1961).
- [122] D. M. Friedrich and W. M. McClain, "Two-photon molecular electronic spectroscopy," Annual Reviews of Physical Chemistry **31**, 559–577 (1980).
- [123] L. Goodman and R. P. Rava, "Two-photon spectra of aromatic molecules," Accounts of Chemical Research **17**, 250–257 (1984).
- [124] M. D. Galanin, B. P. Kirsanov, and Z. A. Chizhikova, "Luminescence quenching of complex molecules in a strong laser field," Soviet Physics – JETP Letters **9**, 304–306 (1969).
- [125] J. P. Hermann and J. Ducuing, "Dispersion of the two-photon cross section in rhodamine dyes," Optical Communications **6**, 101–105 (1972).
- [126] A. Fischer, C. Cremer, and E. H. K. Stelzer, "Fluorescence of coumarins and xanthenes after two-photon absorption with a pulsed titanium-sapphire laser," Applied Optics **34**, 1989–2003 (1995).

- [127] W. Falkenstein, A. Penzkofer, and W. Kaiser, "Amplified spontaneous emission in rhodamine dyes: generation of picosecond light pulses and determination of excited state absorption and relaxation," *Optics Communications* **27**, 151–156 (1978).
- [128] M. A. Albota, C. Xu, and W. W. Webb, "Two-photon fluorescence excitation cross sections of biomolecular probes from 690 to 960 nm," *Applied Optics* **37**, 7352–7356 (1998).
- [129] A. Penzkofer and W. Falkenstein, "Theoretical investigation of amplified spontaneous emission with picosecond pulses in dye solutions," *Optical and Quantum Electronics* **10**, 399–423 (1978).
- [130] T. Gensch, K. J. Hellingwerf, S. E. Braslavsky, and K. Schaffner, "Photoequilibrium in the primary steps of the photoreceptors phytochrome A and photoactive yellow protein," *Journal of Physical Chemistry A* **102**, 5398–5405 (1998).
- [131] J. F. Nagle, S. M. Bhattacharjee, L. A. Parodi, and R. H. Lozier, "Effect of photoselection upon saturation and the dichroic ratio in flash experiments upon effectively immobilized systems," *Photochemistry and Photobiology* **38**, 331–339 (1983).
- [132] H. E. Lessing and A. von Jena, in *Laser Handbook*, M. L. Stitch, ed., (North-Holland, Amsterdam, 1979), Vol. 3, Chap. B6: Continuous picosecond spectroscopy of dyes, pp. 753–846.
- [133] S. Kawato and K. Kinoshita, "Time-dependent absorption anisotropy and rotational diffusion of proteins in membranes," *Biophysical Journal* **36**, 277–296 (1981).
- [134] A. Penzkofer, A. Beidoun, and M. Daiber, "Intersystem-crossing and excited state absorption in eosin Y solutions determined by picosecond double pulse transient absorption measurements," *Journal of Luminescence* **51**, 297–314 (1992).
- [135] G. R. Fleming, A. E. W. Knight, J. M. Morris, R. J. Robbins, and G. W. Robinson, "Picosecond fluorescence studies of rotational diffusion," In *Lasers in Chemistry: Proceedings of a conference held at the Royal Institution, London, 31 May - 2 June, 1977*, pp. 316–321 (Elsevier, New York, 1977).
- [136] K. G. Spears and L. E. Cramer, "Rotational diffusion in aprotic and protic solvents," *Chemical Physics* **30**, 1–8 (1978).

-
- [137] W. Reed, M. J. Politi, and J. H. Fendler, "Rotational diffusion of rose bengal in aqueous micelles: evidence for extensive exposure of the hydrocarbon chains," *Journal of the American Chemical Society* **103**, 4591–4593 (1981).
- [138] W. R. Ware, M. Pratinidhi, and R. K. Bauer, "Performance characteristics of a small side-window photomultiplier in laser single-photon fluorescence decay measurements," *Review of Scientific Instruments* **54**, 1148–1156 (1983).
- [139] A. Srivastava and S. Doraiswamy, "Rotational diffusion of rose bengal," *Journal of Chemical Physics* **103**, 6197–6205 (1995).
- [140] *CRC Handbook of Chemistry and Physics*, 77th ed., D. R. Lide, ed., (CRC Press, Boca Raton, FL, 1996).

Appendix A

Absorption and the effects of molecular rotation

A.1 Molecular orientation and Beer's law

The commonly used molecular absorption cross section σ is an ensemble average of individual molecular absorption cross sections. Specifically, it represents an average over the orientations of the molecules relative to the polarization axis of the incident light. It is the quantity measured in the typical solution-phase absorbance measurement and appears in the differential form of Beer's law,

$$\frac{dI}{dz} = -n\sigma I, \quad (\text{A.1})$$

where n is the molecular number density, I is the photon flux, and z is the distance traveled through the absorbing medium..

For a single molecule the rate of photon absorption is not given by σI but rather by $\sigma_0 I \cos^2 \theta$. The angle between the absorption dipole and the axis of light polarization is θ and σ_0 is the magnitude of the absorption cross section at $\theta = 0$.

Writing Beer's law in terms of these more fundamental parameters gives

$$\frac{dI}{dz} = -n\sigma_0 I \langle \cos^2 \theta \rangle , \quad (\text{A.2})$$

where $\langle \cos^2 \theta \rangle$ represents an average over the orientational distribution of the molecules. For an isotropic distribution

$$\langle \cos^2 \theta \rangle = \frac{1}{4\pi} \int_0^{2\pi} d\phi \int_0^\pi \sin \theta \cos^2 \theta d\theta = \frac{1}{3} , \quad (\text{A.3})$$

which gives

$$\frac{dI}{dz} = -\frac{1}{3} n\sigma_0 I . \quad (\text{A.4})$$

From Eq. (A.1) and (A.4) the relation

$$\sigma_0 = 3\sigma \quad (\text{A.5})$$

is obtained. This relation holds only for truly randomly oriented media. Deviations from this relation should be expected for more ordered media.

A.2 Effect of rotational diffusion on ground state depletion

A.2.1 Analytical solutions

The importance of molecular orientation effects becomes more evident when ground state depletion is considered. As a first approximation, consider the case of a single molecule excited by a pulse of light shorter than the relaxation time of the excited states. During the pulse of light the rate equation describing the probability of ground state occupation, p , is given by

$$\frac{dp}{dt} = -\sigma_0 I \cos^2 \theta p = -3\sigma I \cos^2 \theta p , \quad (\text{A.6})$$

where the effects of stimulated emission have been neglected and Eq. (A.5) has been applied. For the case of rotational motion rapid compared to the rate of absorption, the solution for a collection of molecules can be approximated by averaging the molecular orientation at each instant in time. From this we obtain

$$p(\tau) = \int_0^\tau e^{-3\sigma I t (\cos^2 \theta)} dt = e^{-\sigma F} \quad (\text{A.7})$$

where $p(\tau)$ is the probability of the ground state being occupied at the end of a pulse of length τ with photon fluence F . At the other extreme is the case of no rotational motion during the pulse. In this case the order of the time integration and rotational averaging are interchanged to give

$$\begin{aligned} p(\tau) &= \left\langle \int_0^\tau e^{-3\sigma I t \cos^2 \theta} dt \right\rangle \quad (\text{A.8}) \\ &= \frac{1}{4\pi} \int_0^{2\pi} d\phi \int_0^\pi e^{-3\sigma F \cos^2 \theta} \sin \theta d\theta \\ &= \frac{1}{2} \sqrt{\frac{\pi}{3\sigma F}} \operatorname{erf}(\sqrt{3\sigma F}) . \quad (\text{A.9}) \end{aligned}$$

The ground state depletion behavior is qualitatively different in these two cases, as shown in Fig. A.1. A medium in which molecules are undergoing rapid rotation will approach total ground state depletion much more swiftly than a random medium in which the molecules are stationary. The importance of considering rotational effects on ground state depletion has been previously demonstrated in work such as that of Gensch *et al.* [130] in which the fluence-dependence of laser-induced optoacoustic signals was studied, and Nagle *et al.* [131] in which the change in absorbance of bacteriorhodopsin in purple membrane as a function of fluence was studied. The related topic of rotational effects on transient absorption has been discussed by Lessing and von Jena [132].

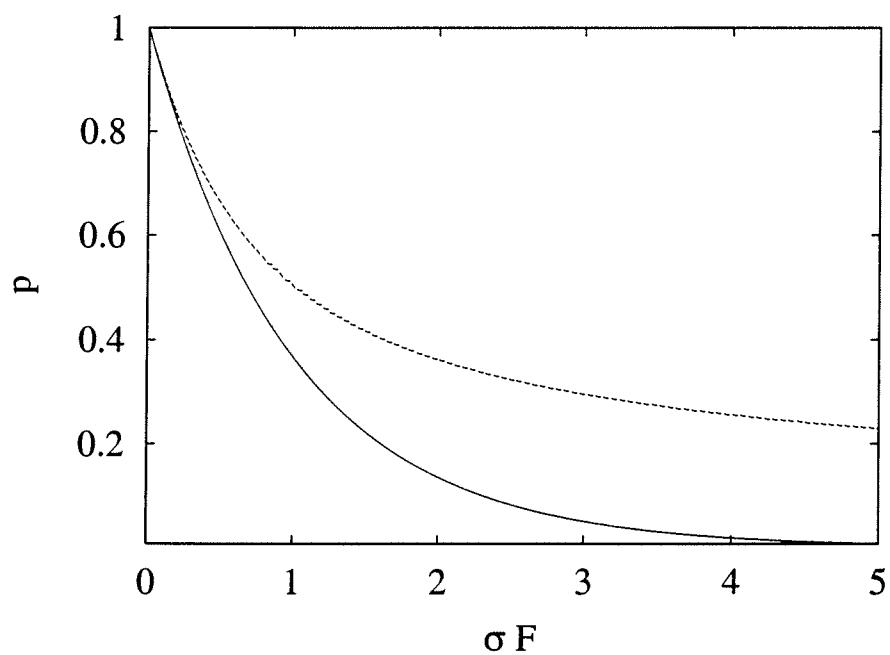


Figure A.1: Analytical solutions of ground state depletion including effects of rotational motion. Rapid molecular rotation (—), from Eq. (A.7); no molecular rotation (- - -), from Eq. (A.9). The ground state population density is given by p and σF is the product of the absorption cross section and photon fluence.

The discussion above applies to linear chromophores such as fluorescein-derivatives. A more complete derivation of similar expressions for both linear¹ and nonlinear chromophores is presented by Kawato and Kinoshita [133]. Nonlinear chromophores such as the metalloporphyrins have more than one absorption moment, which necessitates a more detailed treatment of photoselection effects.

A.2.2 Numerical solutions

If the pulse length of the excitation light is on the order of the rotational time of the molecule, a numerical solution is required. The effects of rotation can be incorporated into systems of rate equations such as those described earlier (see Chap. 3) by changing the $p_i(t)$ to $p_i(\theta, t)$, replacing σI terms by $3\sigma I \cos^2 \theta$, and adding a rotational diffusion term to each rate equation.

One implementation of the rotational diffusion term calculates the orientational averaged probability density for each state, $\langle p_i(t) \rangle$, where

$$\begin{aligned} \langle p_i(t) \rangle &= \frac{1}{4\pi} \int_0^{2\pi} d\phi \int_0^\pi p_i(\theta, t) \sin \theta d\theta \\ &= \int_0^{\frac{\pi}{2}} p_i(\theta, t) \sin \theta d\theta . \end{aligned} \quad (\text{A.10})$$

It is then assumed that $\langle p_i(t) \rangle$ contributes equally to each orientation-specific $p_i(\theta, t)$. For example, by adopting this approximation to the rotational motion Eq. (A.6) becomes

$$\frac{dp(\theta, t)}{dt} = -3\sigma I \cos^2 \theta p(\theta, t) - k_{rot}[p(\theta, t) - \langle p(t) \rangle] \quad (\text{A.11})$$

¹The reader is cautioned that Kawato and Kinoshita's expression for population of excited states of a linear chromophore (equation 15 in [133]) contains an error since it does not approach 0 in the limit of no excitation. This can be corrected by multiplying the second term in that equation by $\sqrt{\pi}/2$.

where k_{rot} is the rotational correlation decay rate. In practice the polar angle θ must be discretized in order to allow for computation such that

$$\theta_i = \frac{\pi}{2N} \left(i + \frac{1}{2} \right) \quad i = 0, 1, \dots, N - 1 \quad (\text{A.12})$$

where N is the number of angular divisions. This implementation of rotational diffusion was adopted by Penzkofer *et al.* [134] in their study of transient absorption by eosin Y.

Understanding this intermediate time scale is relevant for the experiments described in this work. The rotational motion of rose bengal has been the subject of many studies [69, 132, 135–139]. Measurements of the fluorescence polarization anisotropy are most commonly used to determine the rotational diffusion time [64]. The most relevant of these measurements to the present work are for rose bengal in water and methanol where the rotational diffusion times were found to be 310 and 180 ps, respectively, by Small *et al.* [69]. It should also be noted that Ware *et al.* [138] reported an average rotational diffusion time of 48 ps for water and 200 ps for methanol. There is no obvious reason for the significant discrepancy between the two groups' results for rose bengal in water. According to the Stokes-Einstein theory, the rotational diffusion time, τ_{rot} , depends on the properties of the solvent such that

$$\tau_{rot} = \frac{\eta V}{kT} \quad (\text{A.13})$$

where η is the solvent viscosity, V is the molecular volume, k is Boltzmann's constant, and T is the absolute temperature [64, 132]. At room temperature, the viscosities are 1.00 and 0.55 centipoise for water and methanol, respectively [140]. We have chosen to adopt the values of Small *et al.* since they most closely obey the theoretically expected behavior of rotational correlation times increasing linearly with viscosity. The rotational times for rose bengal in other solvents have been in agreement or exceeded that predicted by Stokes-Einstein theory [69, 135, 136].

This makes the Ware *et al.* result for water, approximately 6 times smaller than that predicted by theory, particularly suspect.

In order to examine the impact of rotational diffusion for the conditions studied in this work, we incorporated the algorithm for rotational diffusion described above into a rate equation model of rose bengal (neglecting excitation of higher-lying states for the moment). The results of numerical simulations illustrating the importance of rotational motion on the ground state depletion of rose bengal are shown in Fig. A.2. The dashed curve in this figure corresponds to the parameters under which our experiments were performed. It can be seen that this represents an intermediate case that differs significantly from the two cases in which analytical expressions can be obtained.

The time evolution of the discrete angular subpopulations during an excitation pulse can also be examined. The evolution of the ground state for the intermediate molecular rotation case is shown in Fig. A.3 and the stationary case in Fig. A.4. The three curves shown are the angular averaged population, the population most parallel to the light, and the population most perpendicular to the light. In this calculation there are a total of 8 angular divisions, so from Eq. (A.12) we obtain $\theta_0 = \pi/32$ and $\theta_{N-1} = 15\pi/32$.

The minimum number of angular divisions N required for an accurate calculation was investigated. The variation in ground state population as a function of fluence was calculated for N between 2 and 64. As can be seen in Fig. A.5, there is little difference between $N = 4$ and $N = 8$. No difference was noticed between the $N = 8$ and $N > 8$ calculations (not shown).

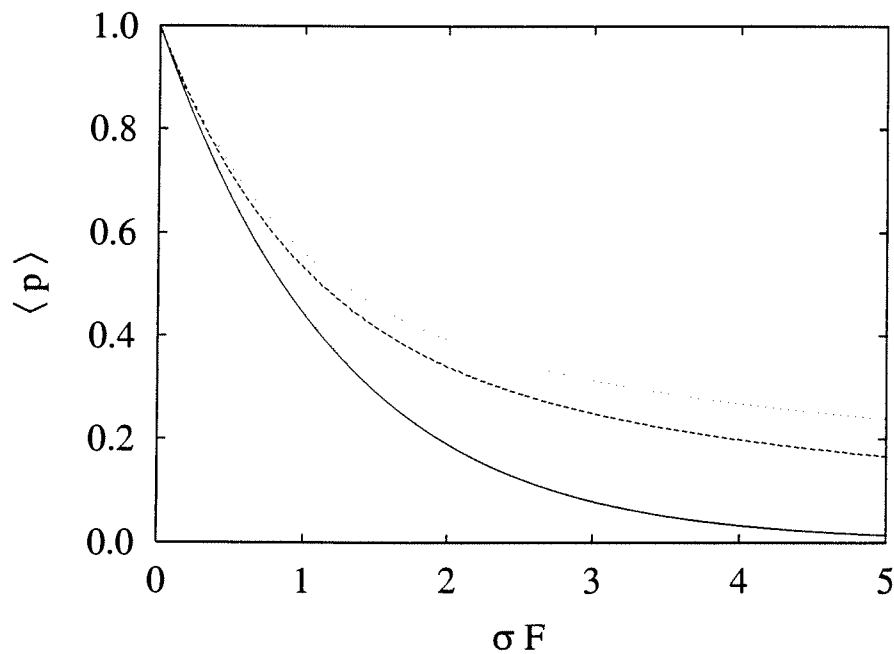


Figure A.2: Numerical solutions of ground state depletion including effects of rotational motion. Calculated for a model of rose bengal in which absorption only occurs from the ground state and the excitation pulse has a FWHM of 0.2 ns. Angular space was divided into $N = 8$ divisions. Rapid molecular rotation (—), $k_{rot} = 1000 \text{ ns}^{-1}$; intermediate molecular rotation (- -), $k_{rot} = 3.2 \text{ ns}^{-1}$; no molecular rotation ($\cdot \cdot \cdot$). The intermediate value of k_{rot} corresponds to that measured for rose bengal in water [69]. The ensemble average ground state population is given by $\langle p \rangle$ and σF is the product of the absorption cross section and photon fluence.

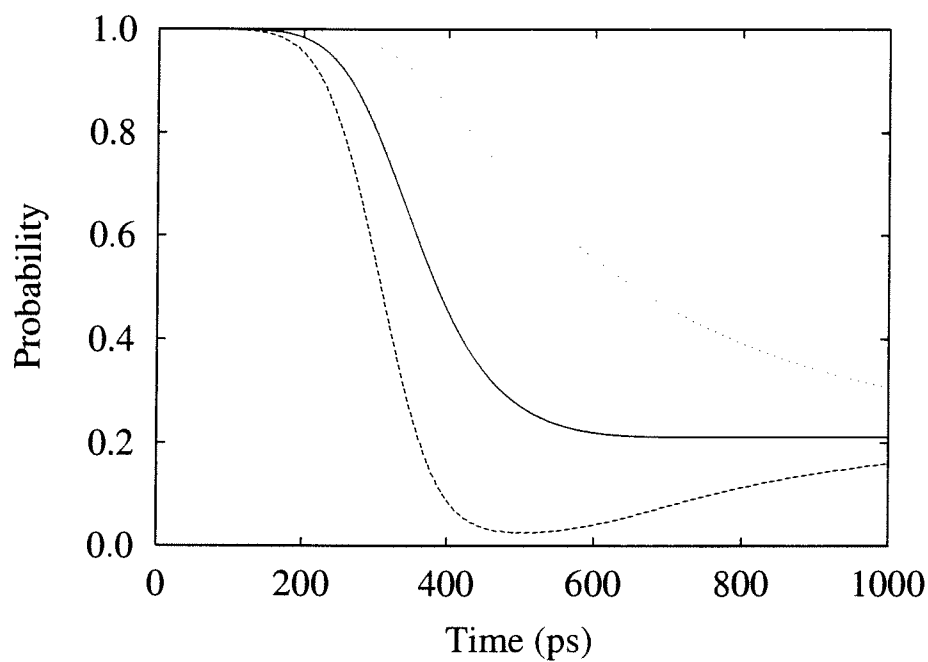


Figure A.3: Evolution of the ground state population when $k_{rot} = 3.2 \text{ ns}^{-1}$. Calculated for a model of rose bengal in which absorption only occurs from the ground state and the excitation pulse has a FWHM of 0.2 ns. Angular space was divided into $N = 8$ divisions. $\langle p(t) \rangle$ (—); $p(\theta_0, t)$ (- - -); $p(\theta_{N-1}, t)$ (\cdots).

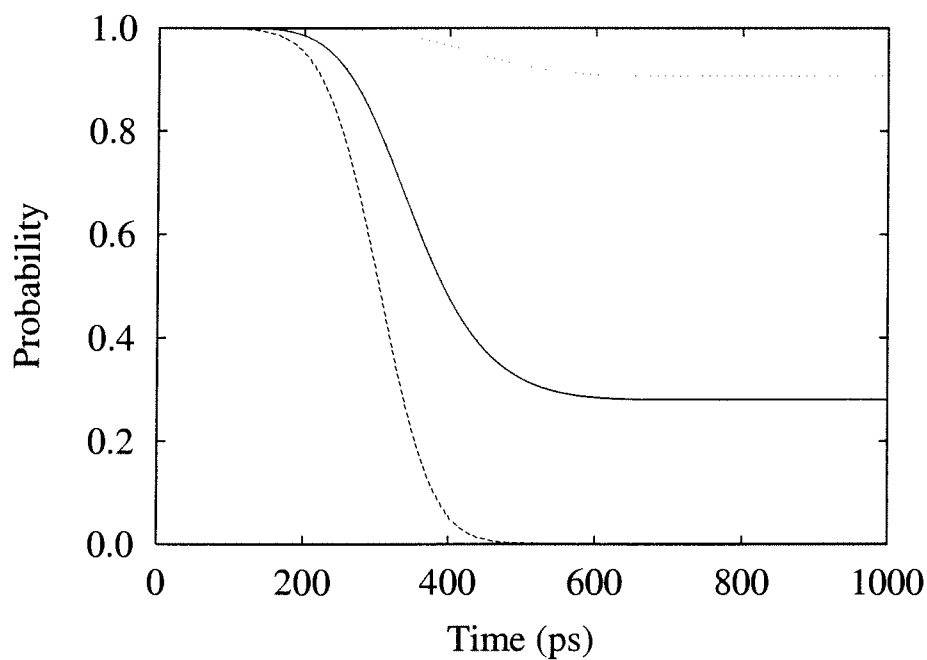


Figure A.4: Evolution of the ground state population when $k_{rot} = 0$. Calculated for a model of rose bengal in which absorption only occurs from the ground state and the excitation pulse has a FWHM of 0.2 ns. Angular space was divided into $N = 8$ divisions. $\langle p(t) \rangle$ (—); $p(\theta_0, t)$ (- - -); $p(\theta_{N-1}, t)$ (\cdots).

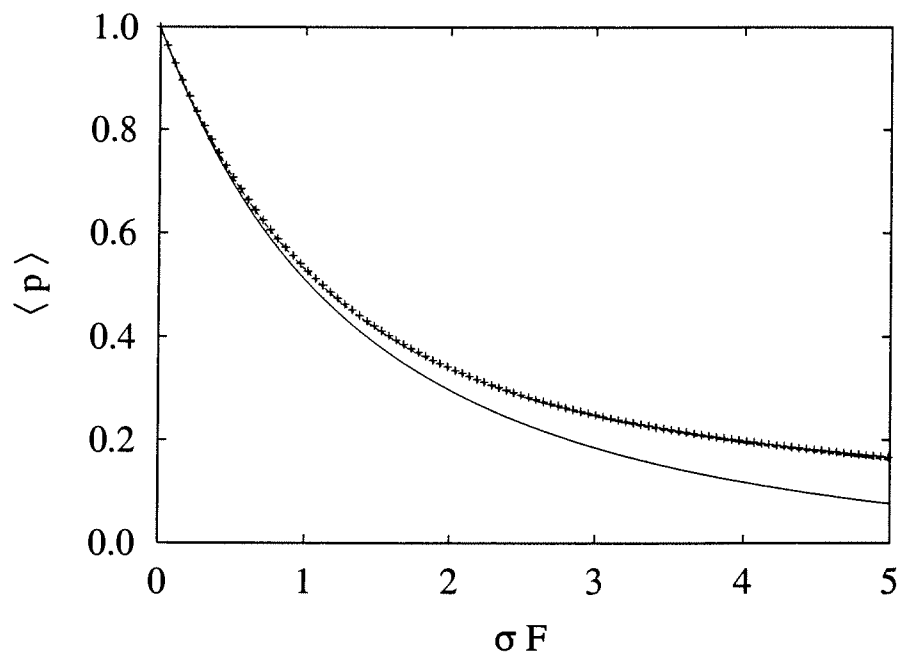


Figure A.5: Dependence of rotational diffusion model on number of angular divisions. Calculated for a model of rose bengal in which absorption only occurs from the ground state, the excitation pulse has a FWHM of 0.2 ns, and $k_{rot} = 3.2 \text{ ns}^{-1}$. $N = 2$ (—); $N = 4$ (- - -); $N = 8$ (+). The ensemble average ground state population is given by $\langle p \rangle$ and σF is the product of the absorption cross section and photon fluence.